TABLE OF CONTENTS

LIST OF FIGURES

LIST OF TABLES

CHAPTER 1

INTRODUCTION

1.1 OVERVIEW

In the recent years, icephobic surfaces have gained a lot of interest due to their potentials in protection of power transmission networks, transportation infrastructure, and aerial vehicles. A unified definition of icephobicity does not exist in the scientific literature, but generally a surface which can resist the ice accretion in one way or another is considered to be icephobic. Some icephobic surfaces can reduce the adhesion strength between the accumulated ice and the surface, while others may be able to prevent or hinder ice accumulation.

Generally, superhydrophobicity (i.e. very low adhesion force between liquid water and surface) is closely related to icephobicity. Water droplets are extremely mobile on such surfaces, leading to some unique characteristics that can be exploited for various applications. Due to this vast range of potential applications, superhydrophobic surfaces have become popular in the past few decades. Several methods have been developed for fabrication of superhydrophobic coatings. Among these methods, plasma surface treatment is a relatively new approach, with several advantages over more conventional methods, for surface modification of metallic and non-metallic substrates.

In this study, a two-step procedure is proposed for the development of superhydrophobic/icephobic coatings using atmospheric-pressure plasma. The first step is a plasma-based surface roughening procedure while the second step consists of plasma polymerization of an organosilicon precursor on the roughened structure. The effect of various plasma parameters on surface properties is studied and optimum plasma conditions for both steps are identified. Furthermore, in order to better understand the efficiency of these coatings in practical applications, the effects of various natural factors on surface characteristics is studied.

1.2 PROBLEM DEFINITION

Several countries around the world such as Canada, United States of America, Sweden, Norway, Russia and China contend with ice-related problems on a yearly basis. Ice accumulation during different atmospheric events, if not addressed swiftly and with precision, can lead to power shortages, driving and aviation accidents as well as significant life hazards.

In the winter of 1998, a massive ice storm hit a large part of North-eastern North America including southern Quebec, South-eastern Ontario, and North-eastern New York, causing 28 related fatalities and destroying almost 1000 transmission towers, 35000 utility poles and enough wires and cables to stretch around the world three times [1,2]. This catastrophe left 4.7 million people in Canada and 500000 people in the United States without electrical power for up to a month [2]. The damages were estimated to be more than 3 billion dollars [1], from which 1 billion dollar was spent on repairing the damage to the Canadian power companies, Hydro Quebec and Ontario Hydro (now known as Hydro One) [3].

By definition, any form of ice accumulation originated from the atmosphere is referred to as atmospheric icing [4,5]. However, depending on some climatic factors such as

wind speed, temperature or droplet dimensions, various forms of solid water with specific physical properties may form on the exposed structures. Table 1-1 and Figure 1-1 show some of these solid water phases along with their physical properties, their appearance, and their formation criteria [6]. It should be noted that different forms of ice affect the exposed structures to different extents. For instance, in contrast with glaze ice which can be very dense and adhesive to the surface, dry snow may be easily blown off without imposing any significant structural loads.

Table 1-1. Various water-based solid-phase materials that can form from liquid or gaseous water [6].

Frost	Sparse dendritic crystal structures; nucleates from the vapor phase via desublimation or condensation followed by freezing.
Glaze	Clear, dense, and hard ice; forms from freezing rain of large droplets with diameters ranging from 70 μm to even a few millimeters.
Rime	White, brittle, and feather-like ice that forms because of freezing of super-cooled droplets with diameters in the range of 5–70 μm originating from clouds or fog.
Snow	A mixture of ice and water. Snow is 'dry' when the air temperature is below -1 or -2 °C, but at temperatures closer to freezing point a thin layer of water covers ice, creating wet ice with properties between ice and water.
Ice	A brittle frozen state of water which can appear transparent or a more or less opaque bluish-white color depending on the presence of impurities such as particles of soil or bubbles of air.

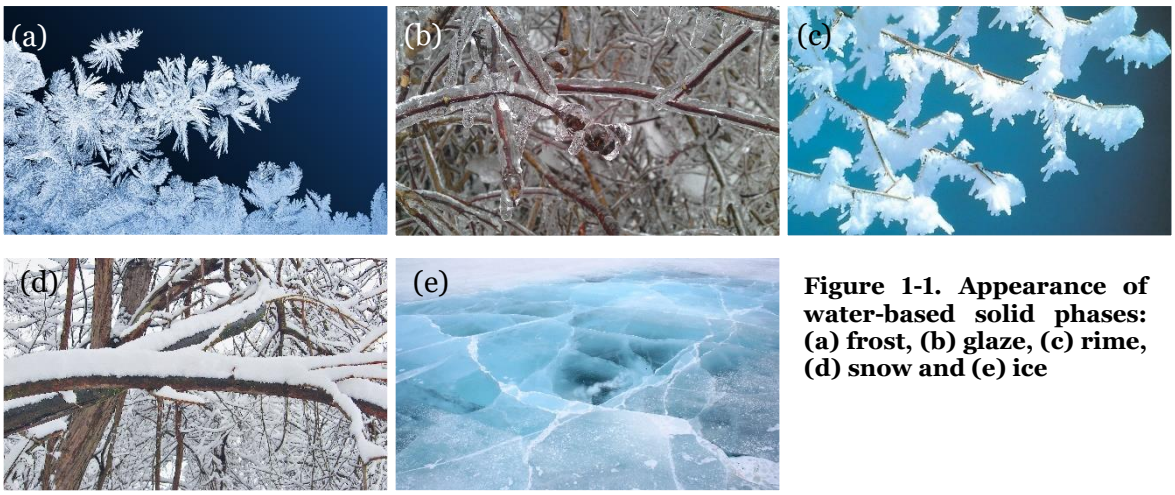

Figure 1-1. Appearance of water-based solid phases: (a) frost, (b) glaze, (c) rime, (d) snow and (e) ice

Glaze ice is the most problematic form of atmospheric icing due to its density, hardness, and adhesion to the surface. The conditions used for ice accumulation in this study are therefore chosen in a way that favor glaze formation (see Table 3-6). In natural conditions, glaze ice is usually formed after an ice storm or a freezing rain. An ice storm occurs when a thin layer of moist and warm air is trapped between two layers of sub-zero cold air, one near the ground and the other one in the upper atmosphere. The snow which is originated in the upper layer will melt while passing through the warm layer and then super-cools before hitting the ground. Super-cooled drops will freeze upon impact, forming a thick hard layer of ice on exposed structures (Figure 1-2) [2,3].

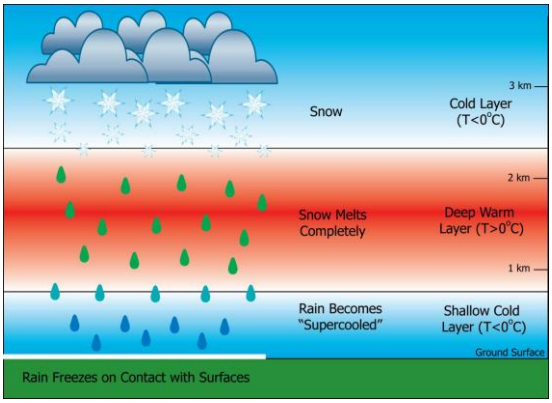

Figure 1-2. Schematics of how a freezing rain occurs [2].

To prevent failure, power companies try to build overhead lines and transmission towers that are capable of withstanding large icing events. This requires strengthened towers and costly lines, which will increase the construction and maintenance cost [5,7]. To avoid such excessive costs while being able to prevent the failure of power transmission network, a solution should be found to either remove the ice from the surface (active icing protection) or prevent its accretion from the beginning (passive icing protection). In this study, a passive icing protection method based on plasma treatment of Al-6061 surface is proposed and the efficiency of such method is studied.

1.3 OBJECTIVES

The general objective of this research is to develop a superhydrophobic/icephobic coating through an atmospheric-pressure plasma treatment procedure for protection of high-voltage overhead lines against atmospheric icing. The specific objectives are as follows:

- Generation of a roughened structure through air plasma treatment:
    - Identifying the transformation mechanism
    - Studying the role of plasma gas on the transformation
- Deposition of hydrophobic materials on the roughened structure:
    - Studying the effects of various plasma parameters (precursor flow rate, ionization gas, plasma power, number of deposition passes) on surface properties (morphology, chemical composition, wetting, ice adhesion strength)
- Evaluation of the coating performance in natural environments under the effects of different natural factors, such as icing/deicing cycles, ultraviolet radiation, and water immersion

1.4 ORIGINALITY STATEMENT

Hexamethyldisiloxane (HMDSO) is one of the most common organosilicon precursors in atmospheric pressure plasma treatment. However, only a handful of studies have reported the development of a hydrophobic coatings by plasma polymerization of HMDSO. Even fewer studies have been dedicated to the icephobic properties of plasma-polymerized organosilicon-based coatings. Since atmospheric pressure plasma polymerization is relatively cheap, safe, quick, and environmentally friendly, the procedure introduced here can be a suitable candidate for industrial production of icephobic surfaces on aluminum. To the best of our knowledge, such method currently does not exist.

Furthermore, the pre-treatment process introduced and characterized in this research (Chapter 4) has never been reported before, and its potential applications can go well beyond the icephobic applications discussed here. This process can create a micro porous alumina-based surface structure which is highly hydrophilic, and may be used for several applications, e.g. as a priming step prior to water-based paint application on aluminum.

1.5 THESIS OUTLINE

To provide the reader with a general understanding of the thesis structure and what to expect, a brief overview of each chapter will be presented in this section.

After a brief introduction to the problem at hand along with our proposed solution, chapter two presents a detailed literature review on some of the key concepts used in this research work. At first, the concepts of wetting, icing, superhydrophobicity, icephobicity and their correlation with each other will be reviewed. Then, the physics of plasma along with its commercial and non-commercial applications will be discussed. The applications of various plasma treatment methods in development of hydrophobic and superhydrophobic surfaces

will be discussed next. Finally, the interaction of electrical arcs with the surface and some surface modification methods through arc treatment will be reported.

In chapter three, the experimental methodology used in this study will be described. Every instrument used for surface treatment or analysis will be reviewed in detail and the specifics of each experiment will be presented.

In chapter four, the interaction between the aluminum surface and air plasma will be studied. The micro-porous surface structure resulting from air plasma treatment will be characterized and a phase transformation mechanism will be proposed.

In chapter five, plasma deposition procedure will be discussed and superhydrophobic/icephobic coatings are developed and studied. The effects of some of the plasma parameters on general surface properties will be discussed and a modification to the plasma jet will be proposed. The effects of this modification on surface properties and plasma characteristics will also be reviewed. Subsequently, initial plasma conditions are identified and coatings based on these conditions will be studied regarding their chemical composition, surface topography, wetting behavior, and icephobic properties.

In chapter six, the effects of multiple icing/deicing cycles along with ultraviolet exposure and water immersion on surface characteristics will be studied.

In chapter seven, conclusions of this research work will be presented and a number of recommendations with respect to future work be discussed.

CHAPTER 2

LITERATURE REVIEW

2.1 INTRODUCTION

In this chapter, a review of the relevant literature is presented to better understand the principals of the project and explain the basic concepts related to this work. First, fundamentals of plasma science will be introduced and some of the existing technologies for plasma surface treatment will be discussed. Then, the concepts of hydrophobicity, icephobicity and their inter-correlation will be presented. Finally, the applications of plasma technology in development of superhydrophobic surfaces will be reviewed followed by a discussion on a specific case of plasma-surface interaction.

2.2 WETTING AND ICING

2.2.1 FUNDAMENTALS OF WETTING

Since the prehistoric times, natural superhydrophobic surfaces have been known to mankind. In ancient Egypt, lotus leaf was considered to be a symbol of purity and cleanliness, and thus sacred, due to its superhydrophobic and self-cleaning behavior [8,9]. However, it was not until the early-19th century that the scientific fundamentals behind the superhydrophobicity phenomena were established. In 1805, Thomas Young defined the concept of contact angle (Figure 2-1), and introduced a mathematical relationship between

the contact angle and the surface energies of various interfaces (Equation 2-1) [10]. Even today, his definition of contact angle and its derivatives are used to quantify the wetting behavior of a given surface.

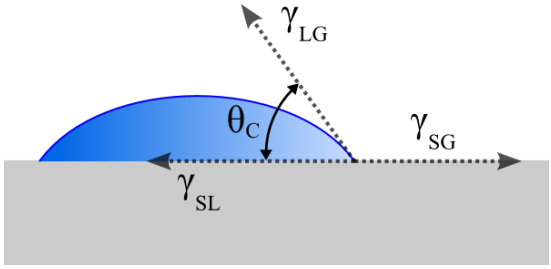

Figure 2-1. Contact angle as defined by Young.

$$\cos\theta_c = \frac{\gamma_{SG} - \gamma_{SL}}{\gamma_{LG}} \tag{2-1}$$

In Young's equation, θ_c is the equilibrium Young contact angle and γ is the surface energy (expressed in energy over area units) for which the subscript denotes the relative interface. Young equation defines the concept of contact angle on an ideally flat and uniform surface. However, to formulate this concept on practical surfaces, the effect of surface topography on wetting behavior should be considered. In this context, in 1936, Robert Wenzel developed a mathematical model (Equation 2-2) for the behavior of a single water droplet on a roughened surface on which the water can penetrate the surface features (Figure 2-2a). This model is now known as the Wenzel wetting regime [11].

$$\cos\theta_w = r_s \cos\theta_c \tag{2-2}$$

In Wenzel equation, r_s is the roughness ratio, and is defined as the ratio of true area of the solid surface to the apparent area, while θ_w and θ_c refer to the apparent Wenzel contact angle and the equilibrium Young contact angle, respectively. Eight years later, Cassie and Baxter developed another model, assuming that the surface features are small enough that the

water penetration is prevented (Figure 2-2b). Their model is known as Cassie-Baxter wetting regime and the equation governing the contact angle in this case is known as the Cassie-Baxter equation (Equation 2-3) [12].

$$\cos\theta_{CB} = f_s(\cos\theta_c + 1) - 1 \qquad (2\text{-}3)$$

In Cassie-Baxter equation, f_s is the fraction of solid/liquid interface where the water droplet is in contact with surface, while θ_{CB} and θ_c refer to the apparent Cassie-Baxter contact angle and the equilibrium Young contact angle, respectively. It should be noted that the Cassie-Baxter regime is a quasi-stable state and tends to transform into Wenzel regime over time. However, the mechanism responsible for the penetration of liquid into the surface texture and the criteria involved in the transition between the two regimes are not yet fully understood [13,14].

Complete Wenzel or Cassie-Baxter regime is rare in occurrence, and usually a mixed state is observed where water partially penetrates the roughness features on the surface [15].

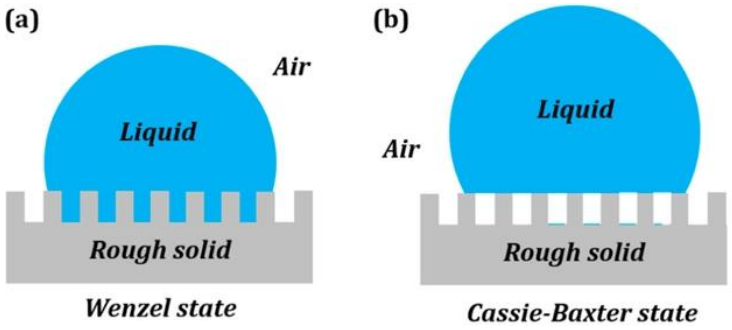

Figure 2-2. (a) Wenzel wetting regime and (b) Cassie-Baxter wetting regime.

As mentioned before, the above equations can generally be utilized in various applications. However, some studies have cast doubts on the generality of Wenzel and Cassie-Baxter equations and our current understanding of the criteria required for validity of each regime. It is proven that these models are only true when the drop size is infinitely

bigger than the roughness dimensions. Very small drops will become axisymmetric, even if the surface shows no sign of symmetry whatsoever [16]. Furthermore, Marmur et al. added an extra criterion for the validity of the Cassie-Baxter regime in relation to Gibbs free energy. They indicated that even if the dimension requirements are met for Cassie-Baxter regime without this extra criterion, Wenzel regime will still be dominant [17]. Brandon et al. demonstrated that two dimensional models, like Wenzel and Cassie-Baxter, are not truly accurate. They proposed a simulated method, which is claimed to be more accurate than the current models [18]. However, most studies on hydrophobic surfaces assume that these models are accurate enough to explain surface wettability behaviour.

Young, Wenzel and Cassie-Baxter models all consider the contact angle of a water droplet resting on the surface, or static contact angle. Besides static contact angle considerations, dynamic contact angles and contact angle hysteresis (CAH) should be considered to fully characterize the wetting behavior on a surface. Dynamic contact angles are defined as the contact angles related to moving liquid fronts (interfaces). For instance, when a droplet is moving on a surface, the contact angle in the movement direction is referred to as the advancing contact angle and the contact angle on the opposite side is referred to as the receding contact angle (Figure 2-3). Contact angle hysteresis is defined as the difference between advancing and receding angles [19].

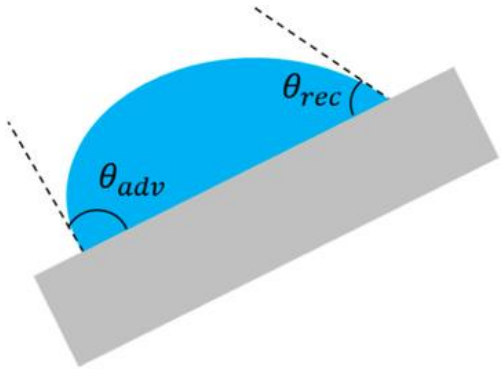

Figure 2-3. Dynamic contact angles on the interfaces of a moving droplet.

Some studies suggest that the concept of static contact angle should be reconsidered [20–24]. It is argued that every so-called static contact angle is in fact an advancing contact angle, and it should be treated as such. Others have claimed that although measurement of static contact angle is not easy, by giving the droplet enough time to reach the state of global minimum energy, in some cases it is possible to observe the 'equilibrium' droplet [25]. Either way, most studies in the literature refer to the contact angle measured for a drop at rest on a surface as static or stationary contact angle.

Contact angle hysteresis is an important factor in roll-off behavior. Lower contact angle hysteresis usually means lower adhesion force between the droplet and the surface and easier sliding of the droplet on the surface [26]. Easy sliding of a liquid droplet on the surface has been proven to be an essential factor in many applications, notably self-cleaning surfaces and anti-icing applications [27]. In the roll-off phenomena, droplets will roll off the surface easily, absorbing dirt and external particles [28]. It has been even suggested that the contact angle hysteresis is a significant tool to fully realize the surface topography and that instead of maximum contact angle achievable, CAH should be taken into account [29].

2.2.2 SUPERHYDROPHOBIC SURFACES

By definition a superhydrophobic surface is a surface for which the equilibrium water contact angle (WCA) is higher than 150° [30–33]. Some studies add the criteria of low contact angle hysteresis to the definition [34,35]. The concept of superhydrophobicity initially emerged from the investigation of natural surfaces with high contact angle and low contact angle hysteresis, notably the lotus leaf (Nelumbo) surface (Figure 2-4) [8,27,36].

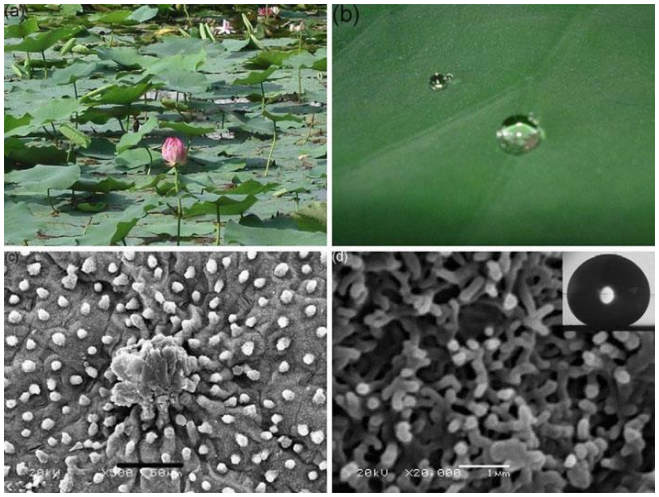

Figure 2-4. (a) Lotus leaves in their natural habitat, (b) a water droplet on a lotus leaf and (c,d) SEM images of lotus leaves with different magnifications [37].

The superhydrophobic characteristics of the micro-nanostructured and wax coated surface of the lotus leaf was first studied by Dettre and Johnson in 1963 [38]. Since then, several other examples of natural superhydrophobic surfaces have been discovered. Figure 2-5 shows some examples of these surfaces and their surface nanostructure responsible for superhydrophobic characteristics.

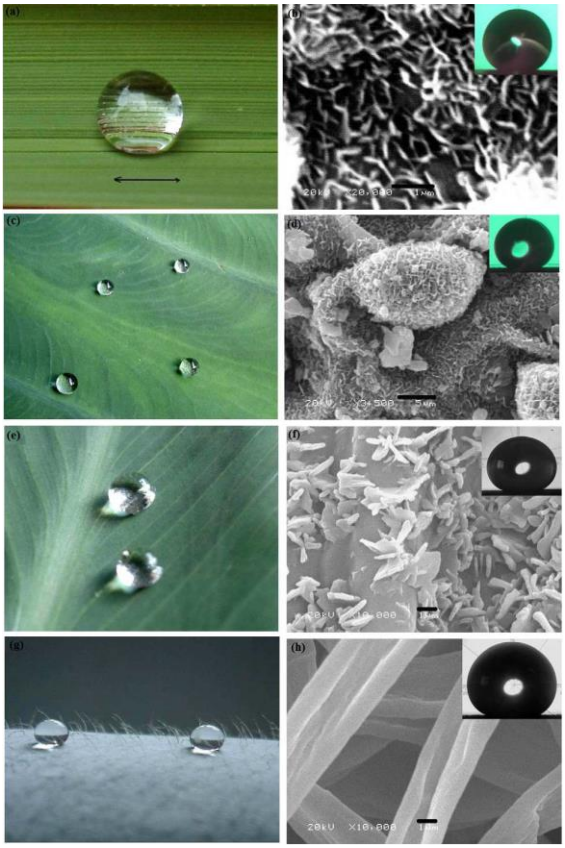

Figure 2-5. Examples of natural superhydrophobic surfaces. On the left side, photos of a water droplet on a rice leaf (a), taro leaf (c), india canna leaf (e) and Chinese watermelon surface (g). On the right side, SEM images of the same leaves: rice leaf (b), taro leaf (d), india canna (f) and Chinese watermelon (h) [37].

It has been shown that the wax nano-crystals present on the leaves of Colocasia Eculenta (taro leaf) are capable of trapping air between a water droplet and the leaf surface [39]. Euphorbia Myrsinites, another plant native to Southeastern Europe and Asia Minor, has superhydrophobic leaves due to its hierarchically nano-structured leaf surface. Rice leaf, Chinese watermelon and India canna leaf are also known to be superhydrophobic [40]. Barthlott et al. studied 350 leaves through SEM imaging and showed that the hierarchical roughness on a leaf surface plays an important role in its self-cleaning effect [8]. For more information on natural superhydrophobic surfaces, see [8,27,37,40].

Water droplets roll freely on a superhydrophobic surface, carrying away any contamination, which is why superhydrophobic surfaces are usually considered to be self-

cleaning [27]. During the past few decades, many studies have been done trying to mimic some of the structures observed on natural superhydrophobic leaves to develop artificial superhydrophobic surfaces, which can be useful in numerous applications. These applications range from textile industry to power network design and maintenance [34]. Many studies have been done on water-repellent self-cleaning fabrics [41–43]. Since icephobicity (i.e. low adhesion force between ice and the substrate) shows a correlation with superhydrophobicity [44], superhydrophobic coatings can be considered as a suitable candidate to reduce the ice accumulation on various structures, notably power network equipment [36,45–49]. Construction industry can benefit from the development of superhydrophobic surfaces for manufacturing self-cleaning windshields and windows [17,36,50,51]. In marine industry, superhydrophobic coatings can be used to develop anti-fouling surfaces [52]. Finally, due to their potential in minimizing the liquid/surface contact area, hydrophobic and superhydrophobic surfaces can be used in anticorrosion application [40,53–55].

Many approaches and techniques can be utilized to impose superhydrophobic characteristics on various metallic and polymeric substrates. Sol-gel reactions [56–58], electrochemical deposition [59–61], layer-by-layer deposition [62–65] and spin coating [66] have been used to develop superhydrophobic surfaces. One of the most promising approaches for the development of superhydrophobic surfaces is plasma related techniques. Plasma surface treatment approaches are gaining popularity in many applications and therefore, many studies have been done on the applications of various plasma-based techniques in development of superhydrophobic surfaces.

2.2.3 ICEPHOBICITY AND ITS CORRELATION WITH SUPERHYDROPHOBICITY

2.2.3.1 Concept of icephobicity

As mentioned before, the formation, adhesion and accumulation of ice, snow, frost, glaze, rime and their mixtures can be hugely problematic in various industries. Several studies have investigated the development of functional coatings designed to address some of these icing-related issues. The term *'icephobic coating'* is broadly used to refer to such coatings, but no conclusive definition for icephobicity exists in the literature. Some studies define icephobicity as low adhesion strength between ice and a solid surface [67–71]. In this case, ice adhesion strength can refer to shear stress [72,73] or normal stress [74–76]. Some other studies define icephobicity as the ability to prevent, delay or reduce ice accumulation [76,77].

In a review focused on icephobicity (or pagophobicity as it is referred to in the manuscript), Sojoudi et al. present a broad definition based on the literature:

> [...] These different definitions of pagophobicity (icephobicity) correspond to different, although related, properties of anti-icing surfaces. Thus, anti-icing surfaces must display a comprehensive set of characteristics. Water in its solid form should be prevented or delayed in forming on such surfaces, or if formed, the rate of accumulation on the surface should be slowed down. Additionally, the adhesion of ice to the underlying substrate should be reduced, such that it can be easily removed. For engineering applications, these attributes are required for ice in its myriad forms. [6]

Conventionally, superhydrophobic surfaces are suitable candidates for icephobic applications. This can be due to several properties that will be discussed in detail later. However, recent developments have led to a radically different class of ice-repellant surfaces which promotes droplet mobility on the surface. These surfaces, which are inspired by

Nepenthes pitcher plants, are created by infiltrating a micro/nano porous substrate with a non-freezing lubricating liquid to produce a thin, ultra-smooth lubricating layer that minimizes contact angle hysteresis and enhances droplet mobility [78–80]. Such surfaces, which are referred to as SLIPS (slippery liquid-infused porous surfaces), are shown to perform very well in humid conditions and after multiples freeze/thaw cycles. However, some studied have suggested that the mechanical integrity of the lubricating layer can be compromised under external forces, such as gravity [70]. Lubricating liquid can be gradually depleted due to capillary attraction or during deicing, leaving a micro/nano structured substrate which may lead to an increased ice accumulation compared to the untreated surface.

2.2.3.2 Icephobic properties of superhydrophobic surfaces

Conventionally, the development of icephobic surfaces is closely related to superhydrophobicity. Generally, wetting characteristics is studied to better evaluate the icing properties of a surface. Several studies suggest that superhydrophobic surfaces can exhibit icephobic behavior [5,36,45,46,48,49,81,82]. The concept of superhydrophobicity and water contact angle was introduced before. In this section the icephobic behavior of superhydrophobic surfaces along with the correlation between superhydrophobicity and icephobicity will be further discussed.

As mentioned before, the concept of superhydrophobicity was inspired by the investigation of several natural surfaces. It was also observed that the water-repellency behavior of some natural superhydrophobic surfaces decreases drastically with temperature. For instance, hydrophobic properties of Lotus leaf deteriorates as the temperature decreases, while the wings of Morpho Nestira, a butterfly species native to south and Central America (Figure 2-6), retain its superhydrophobic properties even in lower temperatures [83].

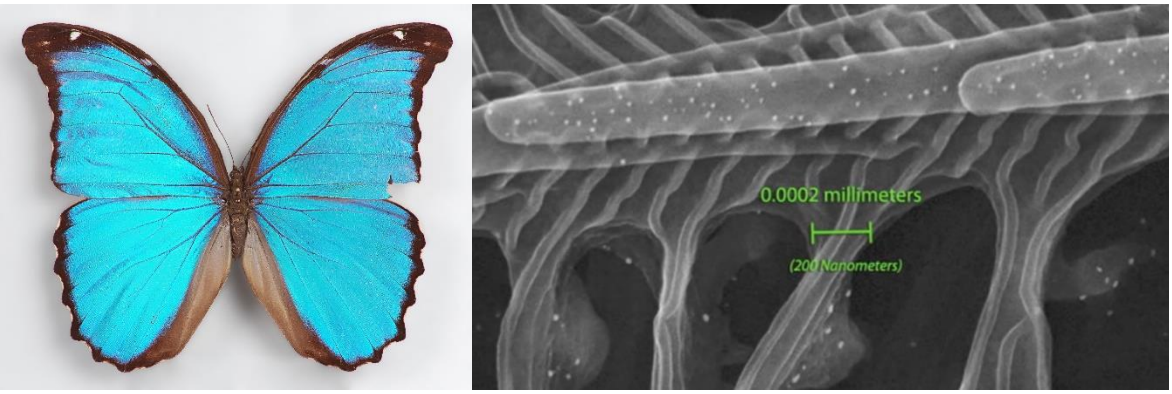

Figure 2-6. Morpho Nestira (left) and a typical multi-level surface roughness observed on its wings (right).

While hydrophobic coatings are shown to be able to reduce the ice adhesion strength to some extent, it has been unclear how this reduction correlates with various measurements of a superhydrophobic surface. This uncertainty was changed when a strong linear correlation was reported between ice adhesion strength and a water wetting related parameter [69,84]:

$$[1 + \cos\theta_{rec}] \tag{2-4}$$

This factor scales with the practical work of adhesion, which is the energy required to remove a water droplet from surface [85]. Meuler et al. studied the ice adhesion strength data from three separate studies (Meuler et al. [69], Dotan et al. [86] and Kulinich and Farzaneh [67]) performed on different sets of surfaces and found a strong linear relationship between ice adhesion strength and $[1 + \cos\theta_{rec}]$ regardless of the ice deposition process and measurement method used (Figure 2-7) [87].

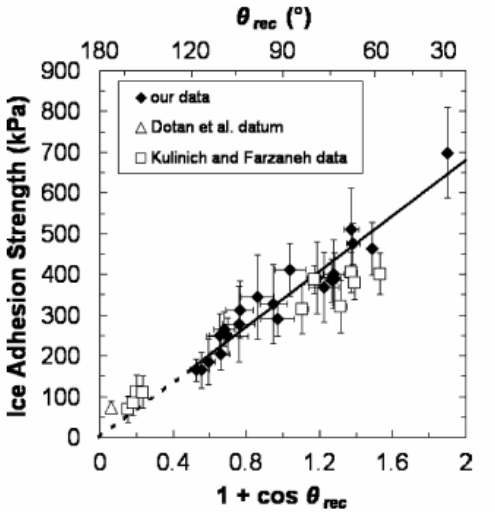

Figure 2-7. Compilation of average strengths of ice adhesion measured for: (♦) 22 nominally smooth test substrates at -10 °C [69], (△) one textured test substrate at -8 °C [86] and (□) 10 textured test substrates at -10 °C [67]. Figure reproduced from [69].

Recent studies show a correlation between superhydrophobicity and icephobicity [46,66,76,88–91]. It has been shown that a low contact angle hysteresis is a defining criterion in icephobicity [67,92,93]. Surfaces with low contact angle hysteresis showed lower ice adhesion strength along with longer delays in freezing times. This suggests that icephobicity is more likely to be achieved in Cassie-Baxter wetting regime. In fact, Meuler et al. have suggested that effective icephobic surfaces must resist transition to fully wetted Wenzel regime that may be brought about by the kinetic energy of impinging water droplets or by the condensation moisture from the ambient atmosphere within the micro and/or nano textures of the substrates [87]. In Cassie ice, the contact area between ice and substrate is significantly reduced, resulting in a reduction of ice adhesion strength, whereas in Wenzel ice, the real contact area is increased due to surface morphology, leading to an increase in total ice adhesion [6].

Recently, a few studies investigated this correlation and suggested that a superhydrophobic surface can reduce or prevent the ice accretion by one or more of the following mechanisms:

(1) The heat transfer between the droplet and the surface is hindered by the insulation effect of the nano-structured roughness on the surface (Figure 2-8). In other words, the micro/nano structure on a superhydrophobic surface acts as an insulating layer on the interface to reduce the heat flux between the liquid and the substrate [46,66,89].

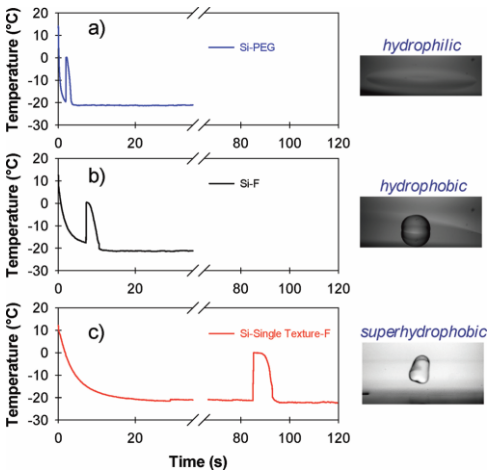

Figure 2-8. Transient temperatures of 4 µL water droplet freezing on a (a) hydrophilic, (b) hydrophobic, and (c) superhydrophobic surface [46]. The spikes in the temperature curves denote the latent heat of fusion and is used as a representative of freezing instant.

(2) In a superhydrophobic surface, contact area between the surface and the water droplet is significantly smaller and therefore, less potential nucleation points are present on the surface. In other words, lower contact area results in higher activation energy for nucleation and growth of the ice crystals. It has been shown that for a superhydrophobic surface, the contributions of solid/liquid interface to the solidification process are negligible [46], i.e. homogeneous nucleation, which is known to have significantly higher activation energy, is dominant. Moreover, smaller contact area can lead to lower heat transfer area between the droplet and the surface, which subsequently delays the freezing point [76].

(3) Unlike hydrophilic surfaces, water droplets are extremely mobile on a superhydrophobic surface and will rebound upon impact (Figure 2-9). The time for which the water droplet is in contact with the surface before rebounding on a superhydrophobic surface is called the droplet rebound time or shedding time. Mishchenko et al. used high

speed video camera to study the impact mechanism and rebound time on several morphologies [94]. They showed that the droplet rebound time can be as short as 20 ms in some cases. If the drop rebound time is smaller than the time needed for ice nucleation, then it can be expected that the ice formation is reduced or prevented [88,91,94,95].

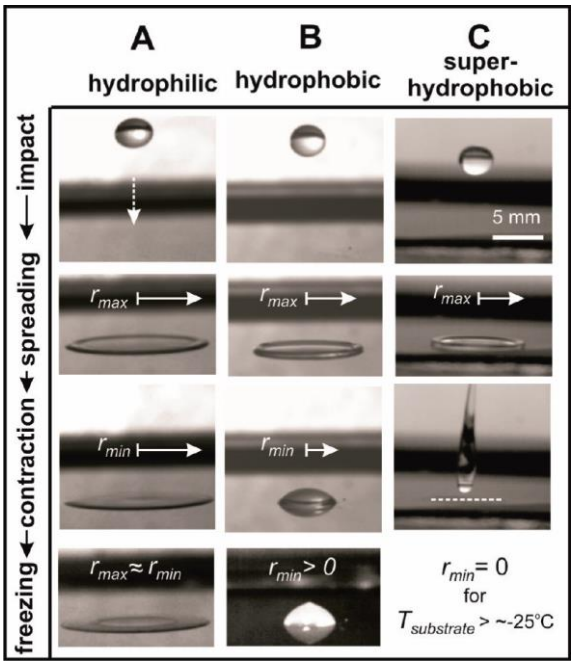

Figure 2-9. Sequential images of the dynamic behavior of 15 µL droplets impacting cooled ($T_{substrate} < 0$ °C) horizontal surfaces from a 10 cm height. Images from top to bottom depict droplet impact, maximum spreading (r_{max}), maximum retraction (r_{min}), and freezing [94].

Although the correlation between superhydrophobicity and icephobicity is often expressed in the literature, several case-dependent factors exist that can increase the ice adhesion strength and thus weaken the icephobic characteristics on a superhydrophobic surface. Unfortunately, most of the studies done in this regard only report the superhydrophobicity and/or icephobicity of the surface, and only a few studies have been done on the stability of such surfaces under various conditions such as UV exposure or icing/deicing cycles. For practical applications, the surface should sustain different natural environments, from severe sub-zero weather conditions and freezing rains in winter to extreme UV exposure and hot weather in summer. It is well known that most of the current

coatings will degrade after exposure to several icing/deicing cycles [46,68,78,96]. Ice build-up and subsequent shedding can destroy the micro/nano-structured roughness on the surface as well as altering the chemical composition of the coating. Therefore, assuming the wide application of such surfaces in outdoor environments, the icephobic characteristics will diminish over time. Another issue which must be addressed is the effect of humidity on the performance of icephobic coatings. Water condensation in humid conditions can degrade the hydrophobic behavior of a surface by covering the roughness features with water and increase the liquid-solid contact area. Similarly, it was shown that in icephobic applications, frost formation in a supersaturated environment prior to freezing is of significant importance (Figure 2-10) [68,71,78,97]. Before the water solidification, frost can cover the micro/nano structure on the surface, thus reducing the hydrophobicity of a surface and increasing the ice adhesion strength. In this case, ice adhesion strength was shown to increase linearly with surface area, suggesting that frost can cover the whole structure, including post tops, side walls and valleys [71].

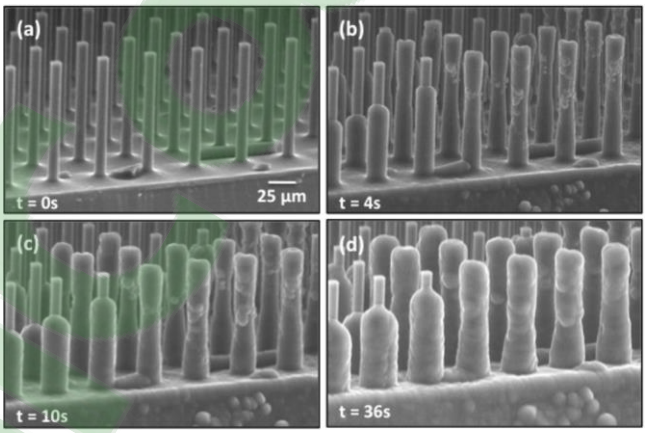

Figure 2-10. ESEM images of frost formation on a superhydrophobic surface. The surface is maintained at a temperature –13 °C [71].

An alternative strategy has been suggested to simultaneously utilize superhydrophobic surfaces along with deicing methods to mitigate the effect of humidity on the icephobic properties of superhydrophobic surfaces. Antonin et al. have shown this

combined strategy can reduce the energy required to avoid ice accumulation on airplane wings by up to 80% [91].

At this point, it should be noted that some materials have proven to prevent ice accumulation by reducing the freezing point and/or maintaining a liquid film between the ice and the substrate and thus facilitating the ice shedding process. Although these materials are not considered to be "icephobic" in the conventional sense, they can be used in various instances where ice accumulation occurs over a relatively short period. During the past few decades, several groups of materials have been used as ice prevention measures [98,99]. Monohydric alcohols, such as methyl alcohol have been used regularly to prevent icing events in aircraft parts. However, they are corrosive and highly volatile liquids, and therefore should be reapplied frequently [99]. Polyhydric alcohols, such as glycols, are more suitable because while still corrosive, they exhibit higher stability in higher temperatures [99]. Some soluble salts, such as nitrous acid salts can also be used to reduce the freezing point of water on an exposed surface.

2.3 PLASMA

Plasma is generally defined as the fourth state of matter, the other three being gas, liquid and solid. From a purely physical point of view, plasma is a mixture of ions (positive and negative), free electrons, and neutral species. It can be created by applying a considerable amount of thermal or electromagnetic energy to a gas, thus ionizing the gas atoms and molecules. Naturally occurring plasmas account for more than 95% of the observable universe (excluding dark matter and dark energy), making plasma the most common state of matter in the universe. Terrestrial plasmas, i.e. plasmas that occur naturally on earth, such as lightnings or polar winds, are more scarce. To generate a synthetic plasma on earth, enough energy must be applied to a gas to sufficiently ionize the gas atoms and/or molecules. This energy is usually provided by an electric source, which can

be direct current (DC), low frequency (LF), radio frequency (RF), or microwave frequency (MW) [100,101].

Over the last decade, research in plasma science and technology has led to a wide range of potential applications. Thousands and thousands of research papers are published each year on both fundamental and technological aspects of plasma science. In medicine for instance, plasma treatment can be used for wound management, tumor treatment, tissue engineering, and equipment sterilization [102–105]. Some studies have also used plasma treatment as an environmentally friendly alternative to chlorine washing for decontamination of food products [106–108]. Through surface functionalization (i.e. grafting of new functional groups on the treated surface), plasma technology is further being used to improve polymer surface properties by exposing them to reactive gases plasmas (like O_2, N_2, NH_3 and H_2O) [109]. Plasma treatment is used in electronics industry in a wide range of applications, from adhesion promotion and cleaning to the deposition and etching of thin films [110]. Plasma reactions have also been used for plastic and nuclear waste disposal [111], nitriding or carburizing of steels [112] and sintering acceleration [113,114].

In all the examples listed above, the process dynamics can judiciously be controlled through fine-tuning of the plasma properties. This includes the number density and temperature of all plasma-generated species. When all particles (ions, electrons, and neutrals) contained in the plasma interact significantly with each other by collisions, a unique temperature T can be used to describe the plasma. In those systems generally characterized by high number densities of charged particles and high temperatures, the plasma properties are driven by thermodynamic equilibrium equations and the plasmas are usually referred to as *thermal plasmas*. On the other hand, when the interaction between all species becomes less important, thermodynamic equations can no longer be applied. Plasma properties must now be obtained by solving the particle and energy balance equations of each species. Since electrons are significantly lighter than atoms and ions, the electron

temperature in such systems is generally much higher than the ion and neutral temperatures. Such plasmas are referred to as *non-thermal plasmas* or *cold plasmas*.

In the next two sections, non-thermal plasmas are categorized based on the gas pressure in which they are generated. The advantages and disadvantages related to each of these categories along with the different technologies for their production are discussed. Furthermore, the specific applications of non-thermal plasmas at low and atmospheric pressure are presented.

2.3.1 LOW-PRESSURE PLASMAS

Low-pressure plasmas are typically generated under controlled environment in a vacuum chamber using DC, kHz, RF or MW electric fields. Depending on the experimental conditions, these plasmas can lead to a uniform treatment of various shapes and geometries, 2D or 3D. Furthermore, since low pressure plasmas are typically characterized by neutral gas temperature close to 300 °K, they can be used for the treatment of heat-sensitive substrates such as polymers and biomaterials. For instance, several studies have been done on the treatment of cancerous cells using low-pressure plasmas [102]. It has been shown that the significant presence of nitrogen and oxygen reactive species can improve the cellular response in tumor cells. It has also been reported that low-pressure oxygen plasma treatment can be used for sterilization of medical equipment [115]. Another study has used various combinations of N_2 and O_2 low-pressure plasmas to modify the surface topography of PET samples [116].

However, the requirements for a vacuum chamber significantly increases the process costs associated with low-pressure plasmas. In particular, the size of the vacuum chamber must increase with the size of the sample such that the treatment of very large objects requires very large (and thus very expensive) vacuum pumps. In addition, the long pumping times required to obtain either a good base pressure or the required operating pressure

prevents any continuous, in-line materials manufacturing. Consequently, the main applications of low-pressure plasmas are limited to markets relying on the treatment of small-volume of high-added value products. This includes, for example, batch-like deposition and etching of thin films in the semiconductor industry.

2.3.2 ATMOSPHERIC-PRESSURE PLASMAS

An atmospheric-pressure plasma is a plasma in which the gas pressure approximately matches the pressure of the surrounding environment. Such plasmas have a significant technical advantage over those operating at low pressure, since no reactor vessel is required for plasma ignition and maintenance. Therefore, they can be directly used in production lines without the need for cost-intensive vacuum chambers and vacuum pumps. However, due to the open-air configurations, plasma treatment of oxidation-sensitive materials becomes limited.

Over the years, several technologies and configurations have been developed to generate and maintain a cold plasma under atmospheric-pressure conditions. Each one of these configurations have their own specific physical and chemical characteristics, making them preferable in some applications rather than others.

One of the most common technologies currently being used is dielectric barrier discharges, usually referred to as DBDs. It was first reported in the mid-19th century as an electric discharge between two electrodes in which one or both electrodes are covered with a dielectric material (Figure 2-11). DBDs are typically very cold with neutral gas temperatures close to 300 K [117], therefore, such plasmas can be used on heat-sensitive substrates. For example, DBD treatments have been investigated for decontamination of fresh vegetables as a more environmentally friendly alternative to chlorine washing [107,108]. Some authors have also used DBDs for the functionalization of wood samples [118,119]. Furthermore, it has been suggested that using a nitrogen based DBD on chronic

or infectious wounds on human skin can increase the micro circulation and control the infection [105].

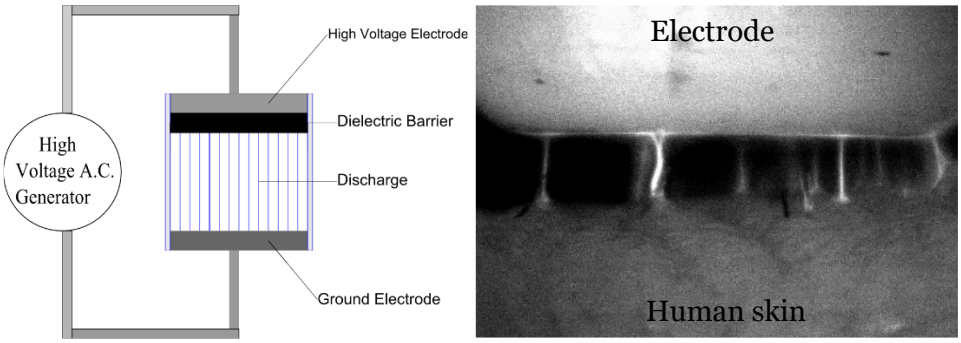

Figure 2-11. Schematics of a DBD reactor from Wikipedia (left) and a dielectric barrier discharge between an electrode and human skin (right) [105].

Another common technology is atmospheric-pressure plasma jets, or APPJs. In a typical plasma jet, working gas (sometimes referred to as the ionization gas) is injected into the jet where ionization occurs. Plasma will then pass through a jet head and then expands into the ambient air where plasma-substrate interaction occurs (Figure 2-12).

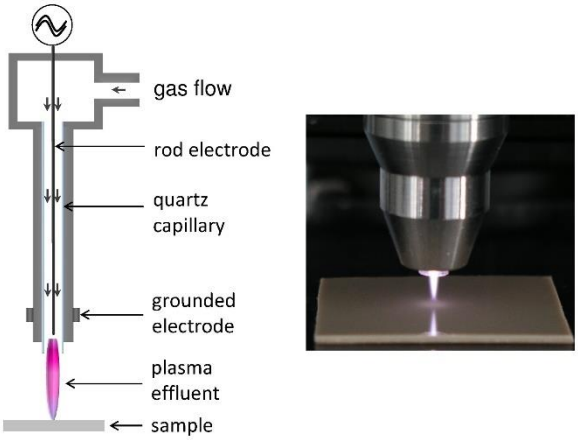

Figure 2-12. Schematics of an APPJ (left) and APPJ treatment on a flat sample (right) [120].

Depending on the process parameters, the neutral gas temperature in APPJs can be tuned from 300 K up to a few thousands K. Like DBDs, “cold” APPJs can be used to decontaminate food products. One specific study by Hertwig et al. used an APPJ to decontaminate black pepper, and showed that the amount of *Salmonella enterica* and

Bacillus subtilis bacteria is reduced significantly after plasma treatment [106]. On the other hand, APPJ can also be used to generate "hot" plasmas which can in turn include thermally-activated processes. For example, Chien et al. developed an APPJ system for removal of structure-directing agents (SDAs) from as-synthesized zeolite, and showed that the effect of APPJ treatment over a period of 60 seconds is comparable to that of thermal calcination over a period of 5 hours [114]. They suggest that the removal process is accelerated by disintegration of SDAs in the zeolite structure due to the high-energy collisions between plasma-generated species and SDA molecules. APPJs have also been used to accelerate the sintering process in some powders. For example, it has been shown that APPJ treatment can accelerate TiO_2 sintering and reduce the time needed from 15 minutes for conventional calcination at 510 °C to 60 seconds [113].

When sustained in the presence of a precursor, non-thermal plasmas (DBDs or APPJs) can also be used for the deposition of functional coatings on surfaces. In plasma deposition, high-energy particles collide with a larger *monomer* compound, breaking its chemical bonds and disintegrating the molecules. These broken chemical functions, which may not be stable in typical process conditions, can then be deposited on the surface [101]. For example, El-Shafei et al. have used a non-thermal glow discharge at atmospheric-pressure to break the bonds in the long chains of a fluorocarbon polymer, depositing fluorocarbon functions on a cotton surface and creating a hydrophobic and oleophobic fabric [121]. Various parameters can affect the coating characteristics, and therefore adjusting the process parameters can vastly change the result. For example, it has been shown that by changing the working gas, the wettability of the surface can be tuned from superhydrophilic to superhydrophobic [122]. Due to their high controllability, relatively low cost, low pollution levels, and short treatment time, non-thermal plasmas at atmospheric pressure are becoming a relatively popular surface treatment method for the deposition of thin films

relevant for several applications, including in the auto industry [123], marine industry [124], wood industry [119], and photovoltaic industry [125].

2.4 PLASMA-SURFACE INTERACTIONS FOR SUPERHYDROPHOBIC APPLICATIONS

As mentioned before, reactive particles in a plasma can be utilized in several ways to modify the surface properties of various materials. In superhydrophobic applications, two major surface characteristics are of outmost importance: (1) surface chemical composition and (2) surface topography. In this regard, plasma surface treatment methods have gained a lot of interest due to their capability of imparting the two characteristics simultaneously. In this section, plasma surface treatment methods are divided into four categories. Etching is primarily used for surface roughening, but it can also alter the chemical composition of the surface. On the other hand, sputtering and polymerization are mainly used for deposition of thin films of hydrophobic materials, but by carefully adjusting the plasma parameters these films can be roughened to some degree. In the final part of this section, the physical interactions between an electrical arc and the surface will be discussed. To the best of our knowledge, arc treatment is not a common method for development of superhydrophobic surfaces. However, since this process has been extensively used in this study, a brief review of the literature will be presented.

2.4.1 PLASMA ETCHING

Plasma etching is the process of selective physical or chemical removal of materials from a surface by reactive plasma radicals. Certain plasma particles react with certain atoms [126] or certain phases [31] on the surface and reaction products are ejected from the surface as gaseous or atomic compounds. For example, oxygen plasma is mainly used in etching of organic materials, where oxygen reacts with carbon and hydrogen and produces gaseous carbon dioxide, carbon monoxide and water [126].

In etching processes, a photo-resistant mask can be used to protect parts of the surface from exposure to the etching medium [126]. Since this process is mostly governed by particle collisions, plasma etching is typically done in low-pressure plasmas. In conventional or wet etching methods, various chemical reactions are utilized to selectively remove the materials exposed to the solvent. However, wet etching has several disadvantages compared to plasma etching. Unlike plasma etching, wet etching can be problematic for roughening of thin films. Besides, solvents or the product solutions may be environmentally hazardous, and should be safely disposed according to numerous standards and regulations which will in turn increases the operation costs [101,126]. Plasma etching on the other hand, is a dry and precise technique without the serious limitations of conventional etching methods [126].

Plasma etching is based on selective erosion. Usually one phase or compound reacts more readily with plasma gas and therefore, etching rate is different at various locations on the surface. If the coating is completely uniform, i.e. the erosion rate is similar for all locations, a photo-resistant mask may be used to cover some and expose other locations. It has been shown that the same effect can be achieved by deposition of photo-resistant micro or nano-structures prior to etching. For instance, polystyrene (PS) micro-beads have been deposited on a glass substrate through various chemical techniques prior to plasma etching with oxygen plasma [127,128]. Oxygen erodes the glass phase more readily, leading to a roughened structure with valleys in between the beads. PS beads may be washed away later with a solvent, fully exposing the micro roughness structure on the glass.

The most common application of plasma etching in development of superhydrophobic surfaces is to generate a micro/nano scale roughness on the surface. This roughened structure may be used as a substrate for further deposition steps [129,130]. For this purpose, oxygen plasma is of significant importance since it can be used to efficiently remove organic functions from the surface. Several studies have reported successful etching

of surface structures on various organic compounds such as polycarbonate, poly(ethylene tetraphalate), polypolyurethane, poly(propylene) and cellulose paper using oxygen plasma etching (Figure 2-13). It has been shown that by adjusting various plasma parameters, such as treatment time, gas pressure, gas composition and plasma power, surface topography can be essentially adjusted to a significant degree [51,131,132].

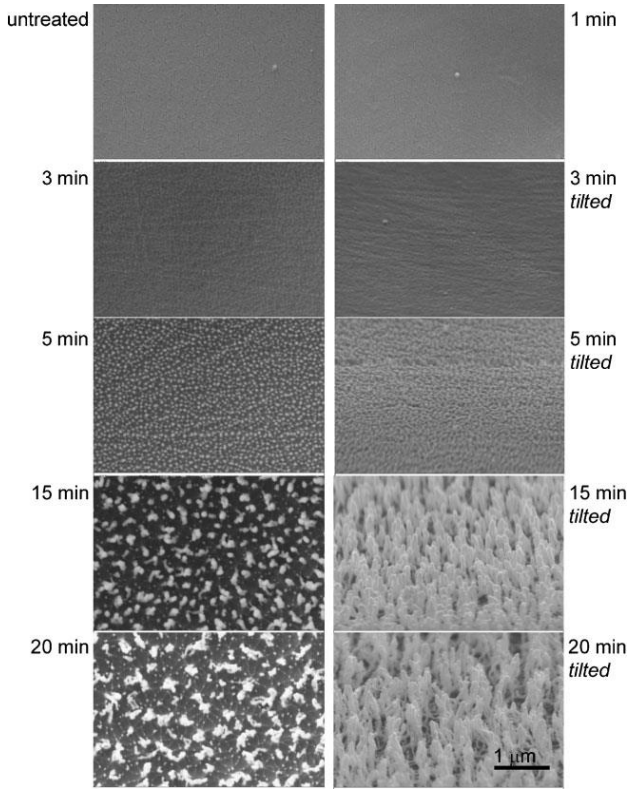

Figure 2-13. Scanning electron microscopy (SEM) pictures (top and tilted views) of untreated and plasma textured PC at different processing time, at 100W RF power [129].

Plasma etching can also be used as an stand-alone treatment procedure to develop roughness on low-surface-energy materials, thus improving their hydrophobic behavior. In this case, PTFE as a substrate is of great interest, since it is a common hydrophobic material which can be easily eroded by oxygen plasma [133–135]. It has been shown that oxygen uptake on the PTFE surface during the treatment process with sufficiently high plasma power is almost nonexistent even after 3 hours treatment time, and thus the amount of polar oxide hydrophilic groups deposited by oxygen plasma etching is negligible [114,133,135,136].

On the other hand, nitrogen or argon plasmas have proved to be ineffective at best in etching of PTFE [135,137].

In some cases of plasma etching, fluorine-based gases can be used for simultaneous roughening and functionalization of the surface structure. Fluorine based groups deposited on the surface during plasma treatment can further decrease the surface energy, thus improving surface hydrophobic behavior. Technically, such process is different from polymerization in the sense that it involves covalently binding plasma species to the surface, rather than physical deposition of hydrophobic materials [138]. For instance, one of the most common gasses for simultaneous etching and functionalization is tetrafluoromethane (CF_4), which is considered to be an etching gas since it does not readily polymerize on the surface [51,128,130]. However, a significant amount of fluorocarbonic groups are typically observed on samples etched with CF_4 (Figure 2-14) which can contribute to the surface hydrophobic behavior [133,139,140].

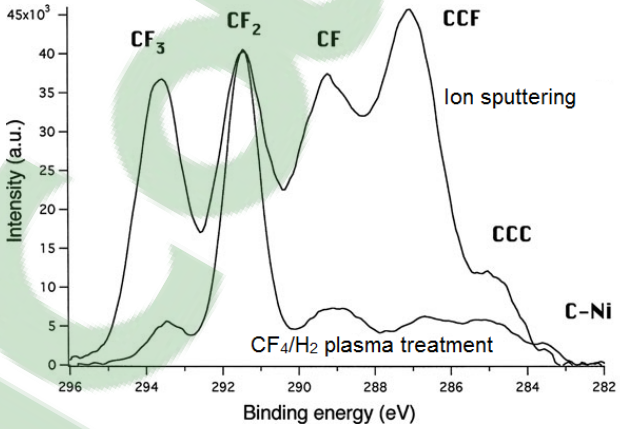

Figure 2-14. A comparison of the two as-deposited XPS results for functionalization and sputtering of PTFE like thin films. The XPS spectra are normalized to the CF_2 peak [141].

Due to its simultaneous roughening and functionalizing effect, it has been shown that CF_4 plasma treatment is more efficient in development of superhydrophobic surfaces compared to other common plasma gases, such as SF_6, Ar, N_2 and O_2 [122,133,134]. Its advantage is not always due to the higher roughness, but also to the lower surface energy

resulting from surface functionalization. In fact, it has been shown that oxygen plasma treatment will lead to a slightly higher roughness on PTFE samples compared to CF_4 with the same treatment time, but higher contact angles can be achieved with CF_4 plasma treatment [133].

2.4.2 PLASMA SPUTTERING

Sputter deposition is a PVD (physical vapor deposition) thin film deposition method which involves the ejection of material from a 'target' onto a 'substrate'. In plasma sputtering, ejection is mostly driven by high energy collisions between plasma species and target molecules, therefore plasma sputtering is typically carried out in low-pressure plasmas.

To initiate plasma sputtering, the coating material (target) and substrate are placed as cathode and anode in a plasma reactor, respectively. A feed gas (e.g. argon) is injected between the electrodes and a voltage in the range of 100 V to several kV is applied. Positively charged ions from the plasma strike the negatively charged target with high energy, thus disintegrating atoms or molecules from the cathode surface. Ejected atoms are then transported in the gas phase and eventually settle on the surface of the substrate, forming a thin film based on the target material [112]. Compared to conventional coating techniques, sputtering is a simple, environmentally friendly and time saving process which results in relatively adhesive films [141]. It is also not limited by the melting point of the coating materials [112] and is capable of forming multicomponent thin films (e.g. alloys) on various substrate [126].

Polytetrafluoroethylene (PTFE) is one of the most common materials in sputtering technology for development of hydrophobic and superhydrophobic coatings. In this case, plasma sputtering is of significant interest because PTFE does not exhibit some essential properties required for other deposition methods. It does not dissolve readily in any solvent

and its vaporization temperature is more than 400 °C [30]. Therefore, sputtering is one of the few methods available for the development of PTFE based thin films.

Argon is one of the most common gasses used in plasma sputtering [142–145]. Occasionally other inert gases like neon and helium may be utilized, but it has been shown that the deposition rate increases with the atomic mass of plasma gas, and therefore deposition rate is generally higher with argon [144]. Inert gasses are preferable for plasma sputtering, since they can minimize the amount of undesirable deposition on the substrate. For instance, using nitrogen as the feed gas in plasma sputtering leads to a significant deposition of nitrogen species on the surface, such as C-N-F or C-N [143].

In plasma sputtering, similar to the case of plasma etching and plasma polymerization, the properties of the deposited film can be adjusted by modifying the plasma parameters. For instance, it has been shown that by increasing the gas pressures in plasma sputtering of PTFE, roughness of the deposited film and the deposition rate of CF_3 and CF functions are increased [145–147]. This correlation can be exploited to develop coatings with different levels of roughness, which are specifically suitable for hydrophobic applications [57].

2.4.3 PLASMA POLYMERIZATION

Plasma polymerization refers to the deposition of polymeric films through dissociation of a monomer in a plasma and subsequent deposition and polymerization of the species on the substrate surface [101]. This process is capable of forming ultra-thin films with suitable mechanical properties [148,149], can be used for monomers that do not polymerize under normal conditions [150,151] and is environmentally friendly [42,148]. Depending on the gas pressure, plasma polymerization can be divided into two categories: (1) low-pressure plasma polymerization and (2) atmospheric-pressure plasma polymerization. The former tends to generate more homogeneous films with less impurities.

It is also considered to be environmentally friendly due to significantly less amount of process gases involved [152]. On the other hand, atmospheric-pressure plasma polymerization can be advantageous due to its lower energy consumption, shorter processing times, lack of need for vacuum equipment and considerably higher growth rates [153–155].

Several materials can be used in plasma polymerization, but in superhydrophobic applications it is essential to consider materials with low surface energy. Two major groups of such materials exist in the literature, fluorocarbons and organosilicons, which will be discussed here.

2.4.3.1 Fluorocarbons

Fluorocarbons are well known for their low surface energy attributed mostly to CF_2 and CF_3 groups. Hare et al. showed that the surface energy of hydrofluorocarbon groups decreases in the following manner [156]:

$$CH_2 > CH_3 > CF_2 > CF_3$$

It has also been shown that higher fluorine content in a coating correlates to a higher contact angle and improved wetting behavior [157]. Thus, fluorocarbons are among the most common choices for development of superhydrophobic surfaces [158]. However, their usage is severely limited due to some environmental concerns [159,160], since many fluorinated compounds and their production by-products are known to be carcinogens.

Polytetrafluoroethylene (PTFE), well known through its commercial name, Teflon, is a hydrophobic and low-friction surface widely used in the manufacturing of household items. Due to its solid state in room temperature, PTFE is not generally considered as an appropriate option for plasma polymerization. However, thin films with chemical compositions close to that of PTFE (Figure 2-14) have been developed through application

of high evaporation temperatures [161] or using tetrafluoroethylene (TFE) as a precursor [32].

In plasma polymerization, plasma parameters can be adjusted to achieve various functionalities in the coating. One of the most important factors in plasma polymerization is the plasma generation power. As the generation power increases, a higher degree of molecular fragmentation can be expected, which can increase or decrease the presence of some radicals in the plasma. In the case of fluorocarbons, it has been shown that the amount of CF_x species decreases as the power increases [130,162,163], which is consistent with the higher fragmentation observed with higher plasma powers.

2.4.3.2 Organosilicons

As mentioned before, the use of fluorocarbons in development of superhydrophobic surfaces through plasma polymerization is limited due to some environmental issues [160]. Therefore, other groups of potential monomers, specifically organosilicons, have been considered for superhydrophobic applications. Although the surface energy of CH_3 and CH_2 groups, to which the hydrophobicity of organosilicons is attributed, is not as low as that of fluorine-based groups [164], organosilicon based polymers are considered as an environmentally friendly alternative to fluorine based polymers for hydrophobicity applications [150,165,166].

In plasma polymerization of organosilicons, the presence of oxygen is of great importance [26,129,167]. Oxygen in the feed gas may result in an abundance of polar and hydrophilic SiO_x groups in the deposited coating, which will adversely affect the hydrophobic behavior of the surface. It has also been suggested that oxygen atoms in the plasma can react with the deposited carbon and decrease the number of organic groups on the surface [26].

Similar to the case of fluorocarbons, plasma power has a significant effect on the surface properties of polymerized silicon-based coatings. Increasing the plasma generation

power increases the fragmentation degree of precursor molecules, which can drastically change the chemical composition of the plasma and several surface properties. Specifically, in the case of hexamethyldisiloxane (HMDSO), it has been shown that since the energy required to break Si-C bond (318 kJ/mol) is less than the energy required to break Si-O bond (452 kJ/mol), higher plasma energies will lead to more polar oxide functions on the surface, which will in turn decreases the surface hydrophobicity [48,168].

On the other hand, the effect of plasma power on surface properties in plasma polymerization of organosilicons can depend on the availability of monomer molecules in the plasma. It has been suggested that increasing the presence of monomer in the plasma will generally lead to higher contact angles [169]. This is due to an increase in the number organic groups in the plasma with increasing the monomer percentage. However, if the generation power is not sufficient to disintegrate enough precursor molecules, increasing the monomer percentage will have no effect on surface properties. It was argued that a critical monomer percentage exists, below which the influence of concentration is dominant on the surface morphology and chemical composition [168]. If the concentration is increased above this amount, plasma power will become the controlling parameter.

2.4.3.3 Other Precursors

Although studies on plasma polymerization for superhydrophobic surfaces are mainly focused on the fluorocarbons or organosilicons, some works have considered the use of other precursors to generate water-repellent surfaces. These precursors can be used with more conventional precursors as improving agents, or they can be used as the sole precursor. HMDSO is an ideal precursor for superhydrophobicity applications for several reasons. However, compared to more conventional fluorocarbons, higher surface energy of HMDSO results in weaker wetting properties. Several studies have been done to address such issues.

For instance, it's been shown that toluene may be used in combination with HMDSO to improve the surface hydrophobicity of organosilicon based coatings [170,171].

Hydrocarbon groups, and especially methyl groups, are responsible for the hydrophobic behaviour of some coatings. Hence, one might expect that hydrocarbon gases themselves can be used in plasma polymerization processes to develop hydrophobic and superhydrophobic surfaces. Indeed, several hydrocarbon gases, like methane [172–174], acetylene [175,176] and propane [176] have been used to develop hydrophobic thin films. Some studies have investigated the addition of fluorocarbons to the hydrocarbon gas [172,176], and as it can be expected fluorine-based groups deposited on the surface can further enhance the hydrophobic behaviour.

2.5 ARC-SURFACE INTERACTIONS

2.5.1 PLASMA-TRANSFERRED ARCS

As mentioned before, plasma is electrically neutral in bulk due to the equal number of positive and negative charges, but for all intents and purposes its electrical conductivity can be considered infinite. This unique characteristic can give rise to the so-called plasma-transferred arcs, or PTAs, where an electric arc is formed between an electrode and the sample being exposed to the plasma. The formation of this arc is facilitated by the high conductivity of the plasma column, and therefore the nature of the working gas has a significant effect on the intensity of the electric arcs.

PTAs are extensively used in welding or alloy deposition [177–180]. In such processes, typically the arc energy is used to melt the surface of the working piece with high precision and controllability. Furthermore, a metallic powder may be injected into the plasma for fabrication of alloys and multi-phase compounds on the surface. Compared to some of the common techniques for welding, such as thermal spraying or laser cladding, PTAs exhibits significantly faster deposition rates with fewer limitations on the material

choice. Since the plasma-arc possesses an extremely high temperature (over 50,000 °K) and a relatively high density of energy (10^5 - 10^6 W/cm^{-2}), a high heating rate and a thin treated layer can be obtained, which may be compared with laser surface treatment. However, unlike laser treatment, PTAs are independent of surface optical reflectivity and are more energy efficient [180].

PTA deposition has been used for development of metal matrix composite (MMC) coatings. Since the 80s, molybdenum, carbide, boride, nickel, and cobalt based powders have been studied extensively in PTA deposition on steel surfaces due to their hardness and wear resistance [178–182]. Similar MMCs have been fabricated with aluminum matrix and boron, graphite, nickel, copper, SiC or Al_2O_3 as the reinforcing phases. It has been shown that these composites can improve the wear resistance and hardness of aluminum, mostly due to the formation of intermetallic phases, such as Al_3Ni, Al_3Ni_2 or Cu_2Al [183].

In the past few decades, PTA deposition process has been studied extensively, but the effects of electric arcs on the surface in the absence of metallic powders is mostly unknown. Moshkovith et al. used an arc treatment procedure for preparation of micro-valleys on the surface of steel substrates (Figure 2-15) [184]. These valleys were then filled with solid lubricants (MoS_2/WS_2) to improve the wear resistance of steel surface.

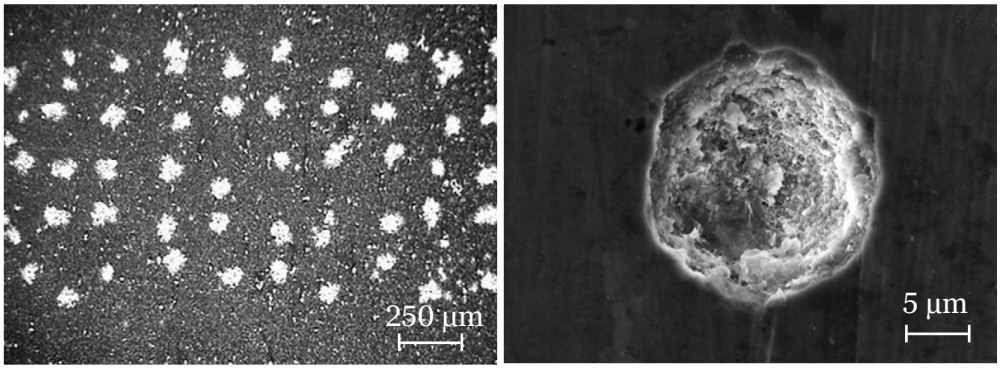

Figure 2-15. The erosion spots on the surface of steel sample (left) and a single dimple on the surface of steel (right) [184].

As mentioned before, the energy density and temperature in PTAs can be compared to that of a laser beam. Since laser ablation is a well characterized process, particularly in terms of modeling, some similarities may be drawn between arc/surface interactions and laser/surface interactions.

2.5.2 LASER ABLATION

Laser ablation, i.e. the ejection of material from a target following irradiation by short, energetic bursts of light, is a well-known phenomenon and a widely used technique for many applications such as thin film deposition, surface cleaning, micromachining, nanoparticle production, etc. [185]. It has been shown that the physical phenomena taking place during laser/surface interaction strongly depends on beam fluence (energy, expressed as J/m^2) and pulse duration, from femtoseconds to picoseconds to nanoseconds [186,187]. Since metal melting and re-deposition occurs in the nanoseconds regime, femtosecond laser pulses do not produce any molten metal and the physical interaction between the surface and the laser is 'clean' [188]. On the other hand, longer pulse durations may lead to the formation of molten metal, introducing new mechanisms which may give rise to some unique surface features.

2.5.2.1 Femtosecond pulses

By using ultra-short pulse durations, formation of molten metal may be avoided since there is not enough time for the heat wave to fully propagate through the metal, regardless of the beam fluence. Figure 2-16 shows an example of such cases. It should be noted that the specific structure observed in Figure 2-16c is due to the instabilities in the evaporation front.

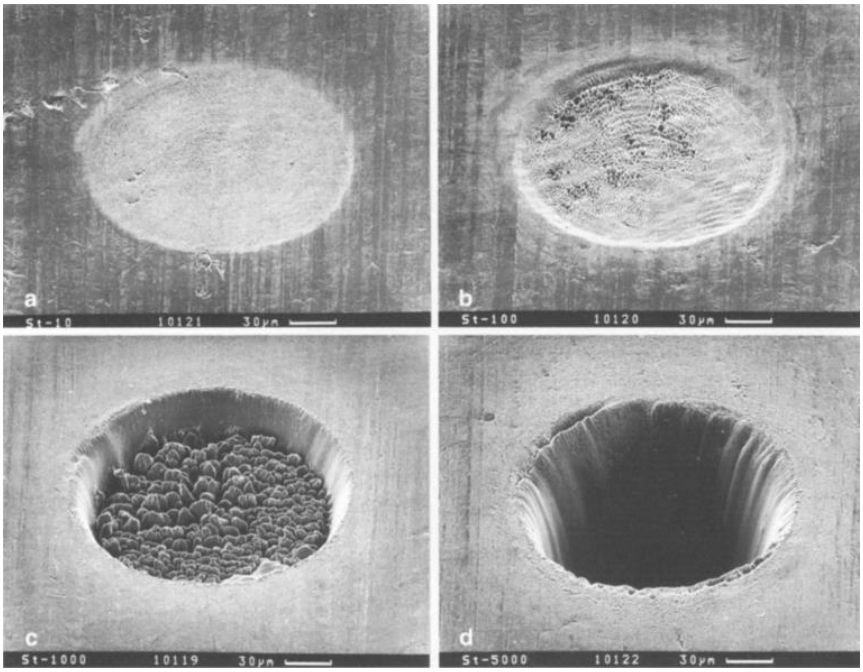

Figure 2-16. Laser processing of a 0.5 mm steel plate with 250 fs, 0.5 m J, and F = 2.5 J/cm² second harmonic radiation (λ = 390 nm) and different number of pulses: (a) 10, (b) 100, (e) 1000 and (d) 5000 laser pulses [186].

2.5.2.2 Pico-second pulses and nano-second low-fluence pulses

Figure 2-17 shows SEM images of holes drilled in a steel foil by laser ablation with pulse durations of (a) 80 ps and (b) 3.3 ns with a fluence of 4.2 J/cm². In such cases, there is enough time for the thermal wave to propagate into the metal target and to create a relatively large molten layer. Therefore, the target material is removed both in vapor and liquid phases. Furthermore, the vaporization process creates a recoil pressure that expels the liquid, the effects of which is clear in Figure 2-17b.

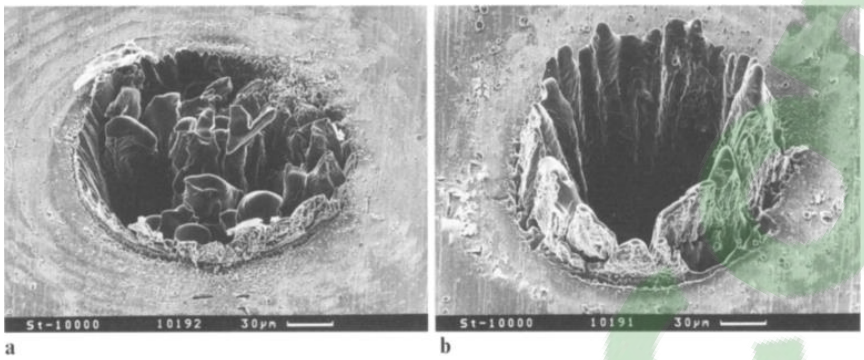

Figure 2-17. Nanosecond-pulse laser ablation and holes drilled in a 100 pm thick steel foil with (a) 80 ps, 900 pJ, F = 3.7 J/cm²; and (b) 3.3 ns, 1 m J, and F = 4.2 J/cm² laser pulses at 780 nm [186].

2.5.2.3 Nano-second high-fluence pulses

When the beam fluence is higher than a measurable threshold value, laser/surface interaction radically changes. In this case, there is enough time for molten metal to form, but unlike the case of shorter pulse duration or lower beam fluence, the sample may be heated well above its boiling temperature. When the temperature reaches $0.8T_c$, where T_c is the critical temperature of the sample, huge density fluctuations take place, metals lose their metallic properties, and nuclei start to shape homogeneously since the conditions for heterogeneous nucleation are no longer valid. The super-heated layer suddenly turns into a mixture of liquid droplets and vapor, and material is removed mainly due to the so-called phase explosion [189–191].

The nature of this phase transformation has been extensively studied through molecular dynamics simulations [185,189,191–193]. It should be noted that the transition from normal vaporization to phase explosion is distinguished by a discontinuous jump in the ablation depth, and was measured by Porneala et al. to occur around a fluence of 5.2 J/cm² for pulse durations of 5 ns (Figure 2-18) [194].

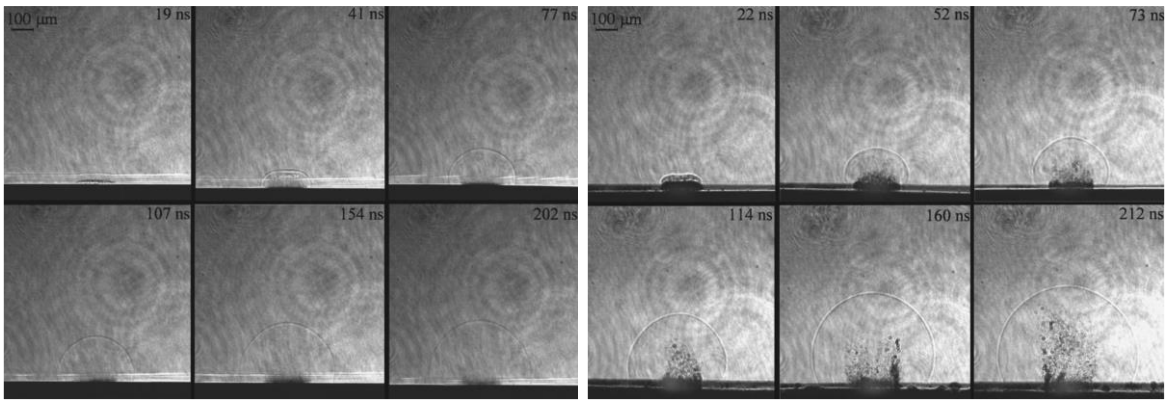

Figure 2-18. Time-resolved photos of phase explosion on the surface of aluminum, (left) F = 4.0 J/cm^{-2} and (right) F = 5.2 J/cm^{-2} [194]. Pulse duration is 5 ns in both cases.

As will be shown later, these surface features and conditions leading to their formation will play an important role in the understanding of the interaction between rotating arc APPJs and aluminum substrates.

2.6 CONCLUSION

In this chapter a thorough review of the literature was presented. The following topics were covered in detail:

- plasma physics and related technologies
- the concepts of wetting, icing, hydrophobicity and icephobicity
- the use of plasma treatment methods in hydrophobic applications
- and the interactions between electric arcs and metallic surfaces.

CHAPTER 3

EXPERIMENTAL PROCEDURE

3.1 INTRODUCTION

In this chapter, the experimental procedure used in this research are described. At first, the reasoning behind sample choice (Al-6061) and the plasma treatment process for both steps along with some details regarding the plasma jet are reviewed. Then, physical and chemical analytical methods used in this are presented in detail and some considerations regarding these analytical methods are mentioned. Finally, the aging procedures (icing/deicing and accelerated weathering) is described.

3.2 SAMPLES

All substrates used in this research are cut from Al-6061 sheets provided by ALCAN and used as-received. The chemical composition of Al-6061 is presented in Table 3-1. It is one of the most common alloys of aluminum, widely used in aircraft and automobile manufacturing, SCUBA tanks, and high-voltage cables due to its corrosion resistance and weldability. Since this study is aimed at the protection of overhead power transmission lines, Al-6061 is chosen as the most common material used for production of high-voltage cables.

Table 3-1. Chemical composition of Al-6061. Values presented in mass percentage.

Si	0.4% -0.8%
Fe	<0.7%
Cu	0.15% – 0.4%
Mn	<0.15%
Mg	0.8% – 1.2%
Cr	0.04% – 0.35%
Zn	<0.25%
Ti	<0.15%
Al	95.85% – 98.56%
Other	No more than 0.05% each, 0.15% total

3.3 PLASMA TREATMENT

An OpenAir AS400 APPJ manufactured by PlasmaTreat (Germany) is used for all of the plasma treatment procedures (Figure 3-1). The schematics of the jet is presented in Figure 3-2.

Figure 3-1. Plasma reactor used in this study.

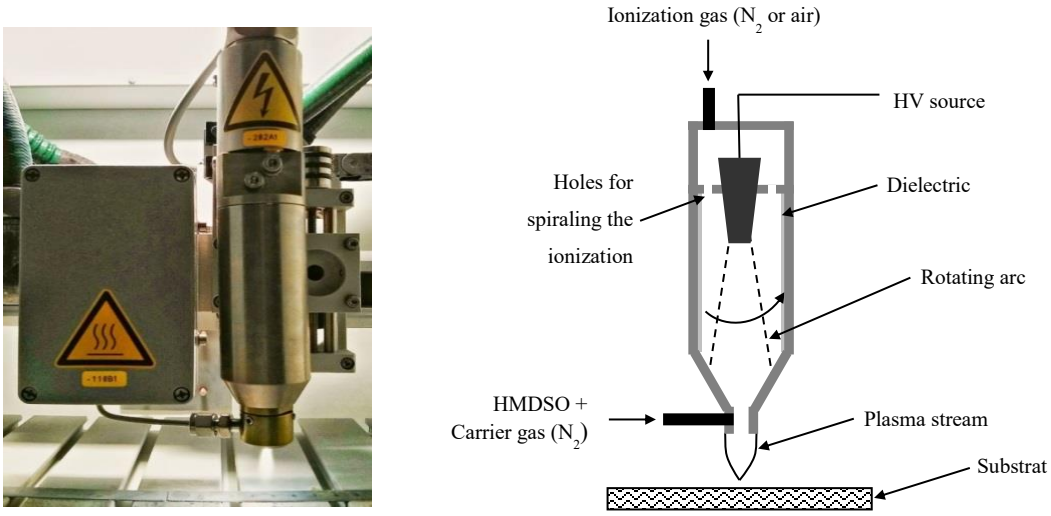

Figure 3-2. Digital image of the working jet (left) and the schematics of the plasma jet (right).

The ionization gas (or the working gas) is injected into the jet through a tube at the top. A low-frequency, high-voltage power source creates a rotating arc discharge inside the source that is responsible for generation of a uniform plasma volume. Due to high gas flow rates, plasma can be pushed downstream through a 5 mm diameter hole located at the bottom of the jet with a diameter of 5 mm. Based on the flow rate of ionization gas, the gas speed at the jet-head can be easily calculated. For instance, for a flow rate of 2500 l/h (air treatment process), the gas speed is determined to be 33.4 m/s, while for a flow rate of 500 l/h (plasma deposition process), the gas speed is 7 m/s.

A precursor injection tube is also implemented in the system which can introduce precursor vapor into the jet-head with a controlled flow rate. Liquid precursors such as HMDSO can be evaporated in the heating unit observed on the left side of the jet in Figure 3-2. The jet is mounted on a two-dimensional automated movement system, which makes it possible to scan a flat sample with various speeds or perform point treatments with adjustable durations. The height of the jet can also be adjusted by a manual dial, located on the right side of the jet.

The power source in this plasma reactor can generate continuous or pulsed discharges. In a pulsed discharge, plasma is turned on only for a small fraction of the total cycle. During the time in which the plasma is disabled, enough time is provided to plasma-generated species to interact with each other and with the surface. The ratio between plasma on time and total cycle is referred to as the plasma duty cycle, and is often abbreviated as PDC. In our system, PDC is expressed as the percentage of plasma on time in a full cycle.

It should be noted that in this plasma reactor, plasma generation voltage is expressed as a percentage of the maximum voltage (≈340 volts) applied to the source. Every voltage value corresponds to a certain generation power and both values are presented in this section.

In this work, the plasma jet is used for two different treatment steps: (1) treatment of Al surfaces in non-depositing environment (N_2 and N_2-O_2 plasma, continuous discharge, maximum power) and (2) the deposition of organosilicon based coatings on Al surfaces (N_2 plasma and a modified jet; pulsed discharge and minimum power).

3.3.1 TREATMENT IN NON-DEPOSITING ENVIRONMENT

Al-6061 plates are cut into 160 x 40 mm pieces and are exposed to the APPJ operating in N_2 or N_2-O_2 (air) with a short distance between the plasma jet and the surface. The conditions used in this step are presented in Table 3-2. Continuous discharge and maximum power are used to ensure maximum interaction with Al sample.

Table 3-2. Plasma conditions used for pre-treatment step.

Plasma voltage percentage	Plasma power	Plasma duty cycle	Jet speed	Jet-substrate distance	Ionization gas flow rate	No. of passes
100%	7.5 kW	100%	1 m/min	5 mm	2500 l/h	3

3.3.2 TREATMENT IN DEPOSITING ENVIRONMENT

50 x 30 mm samples are cut from the pieces treated in non-depositing environment (referred to as pre-treated surfaces) and are used as the substrate for deposition. In this step, the plasma jet is slightly modified to improve the roughness and the chemical composition of the coating (Figure 3-3). The effect of this modification on surface morphology will be discussed in detail later (section 5.4).

In this study, hexamethyldisiloxane (HMDSO) is used as the polymerization precursor (Figure 3-4). HMDSO is liquid at room temperature, easy to handle, cheap and environmentally friendly, thus it is a suitable choice for atmospheric pressure plasma polymerization [129,153,154,168,195]. Besides, methyl groups in the molecular structure of HMDSO can contribute to the hydrophobicity of the surface. Therefore, this precursor appears to be a promising candidate for hydrophobic applications. In this work, HMDSO (>98%) is acquired from Sigma Aldrich and is used as-received.

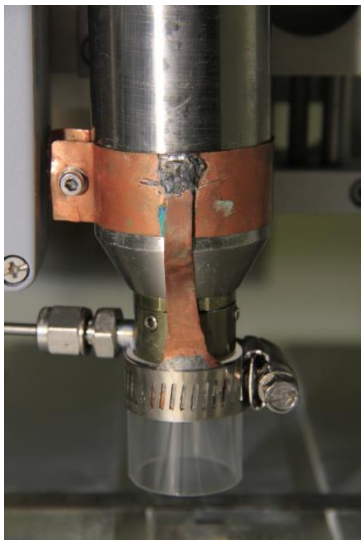

Figure 3-3. Plasma jet setup used for HMDSO deposition. The quartz tube confines the jet, hindering the flow of oxide species and reducing the amount of silica powder on the surface.

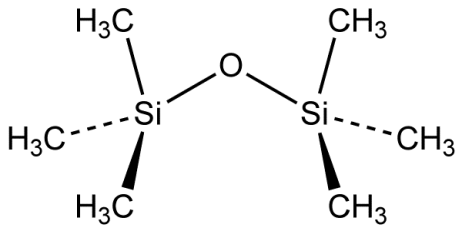

Figure 3-4. Molecular structure of hexamethyldisiloxane.

Plasma conditions used for coating deposition are presented in Table 3-3. Prior to plasma deposition, samples are cleaned in an ultrasonic bath with acetone and deionized water for 30 minutes each. In contrast with the pre-treatment performed in the non-depositing environment, plasma deposition studies are performed under pulsed plasma conditions with minimal generation power. This prevents excessive precursor fragmentation and limits powder formation. This will be further clarified in Chapter 5.

Table 3-3. Plasma conditions used for coating deposition.

Plasma voltage percentage	Plasma power	Plasma duty cycle	Jet speed	Jet-substrate distance	Ionization gas flow rate	Carrier gas flow rate
50%	2.7 kW	50%	1 m/min	30 mm	500 l/h	400 l/h
75%	3.6 kW					

3.4 OPTICAL EMISSION SPECTROSCOPY

An LR2-T optical emission spectrometer, with detector manufactured by Toshiba and the OES Capture acquisition and analysis software developed by Plasmionique, along with a light collection lens is used to study the presence of various chemical components in the plasma. This spectrometer has a spectral resolution of 2 nm, can acquire spectra in the range of 200-1100 nm and is thermoelectrically cooled.

3.5 CONTACT ANGLE MEASUREMENT

Wetting behavior of the samples is studied using a Kruss DSA100 goniometer (Figure 3-5). For sessile droplet measurements, droplet size should be infinitely larger than the surface features and also large enough so that the evaporation effect may be neglected [196]. In this study, static contact angle is measured by depositing a 4 μL droplet on the surface and measuring the contact angle using the Young-Laplace approximation. Static contact angle values presented in this thesis are the average of at least 10 measurements performed on different samples.

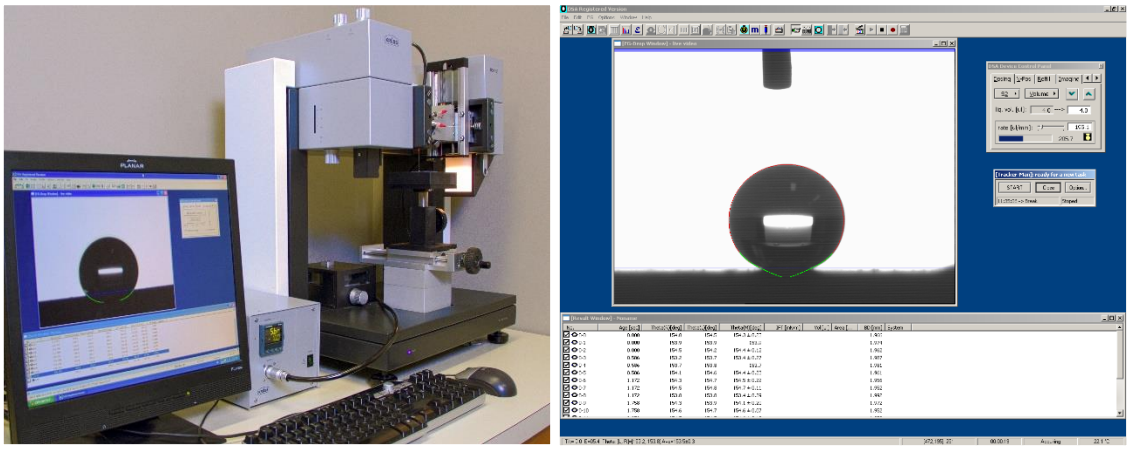

Figure 3-5. Contact angle goniometer used in this study (left) and the software used for image analysis and contact angle measurement (right).

Dynamic contact angle is measured using a method widely accepted as one the most accurate methods to characterize the wetting behavior of a surface [20–22]. At first, the needle is placed close to the surface (Figure 3-6a) and a 4 μL droplet is deposited on the surface (Figure 3-6b). Then the volume of this droplet is steadily increased to 13 μL with a rate of 3 μL/min (Figure 3-6c). The contact angle on each side of the droplet is measured 5 times per second using the tangent method. Advancing contact angle can be defined using the *contact angle vs. time* curve. Similarly, the receding contact angle is defined by reducing the droplet volume back to its initial value (Figure 3-6d) and constantly measuring the contact angle of the moving interface.

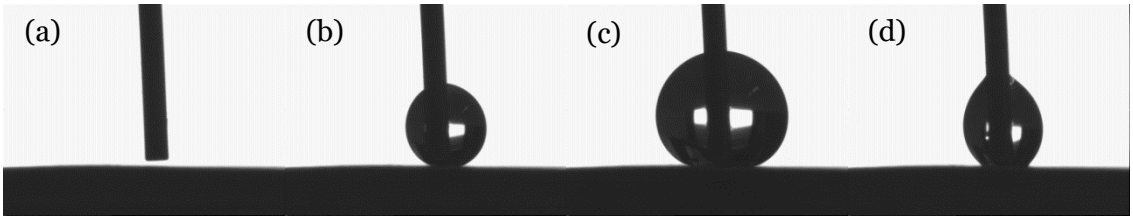

Figure 3-6. Procedure used for measuring the dynamic contact angles.

By definition, advancing contact angle is the contact angle right before the expansion of the droplet baseline. This can be manifested in the contact angle vs. time curves as two possible phenomena: 1) a sudden drop in the contact angle and a subsequent increase until the next drop (baseline sudden expansion) or 2) a constant contact angle value after the initial increase (baseline continuous expansion). Both of these behaviors are observed in this study. Similarly, receding contact angle can be measured (1) at the point before a sudden increase in the contact angle (baseline sudden shrinkage) or (2) at a constant value after the initial drop (baseline continuous shrinkage). Figure 3-7 shows an example of these contact angle vs. time curves for advancing and receding angle measurements.

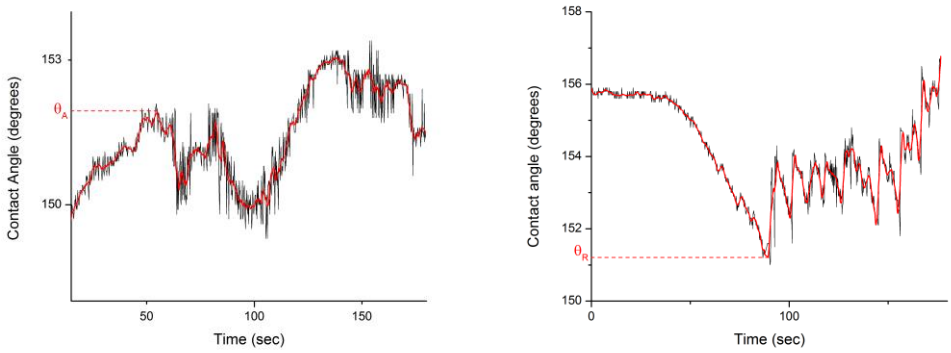

Figure 3-7. An example of advancing (left) and receding (right) curves for dynamic contact angle measurements.

3.6 SCANNING ELECTRON MICROSCOPY

A JSM-7600F scanning electron microscope manufactured by JEOL is used in this study to acquire SEM images of various surfaces. This microscope uses a field emission gun

and has a resolution of 1.4 nm at 1 kV and 1 nm at 15 kV. Due to the low conductivity of the samples studied here, all samples were coated with carbon prior to image acquisition.

3.7 FOURIER TRANSFORM INFRARED SPECTROSCOPY

Chemical composition of the samples is also studied using FTIR spectroscopy. A Bruker Vertex 70 FTIR system is used in ATR mode with a resolution of 2 cm^{-1}. Each one of the FTIR spectra presented in this thesis are averaged over 30 consecutive scans on the sample.

3.8 X-RAY PHOTOELECTRON SPECTROSCOPY

Chemical composition of the surface is studied using an X-ray photoelectron spectrometer (Figure 3-8) with a non-monochromatic Al (max energy 1486.6 eV) anode jointly manufactured by Plasmionique (Canada) and Staib Instruments (Germany). Compared to FTIR, XPS can measure the absolute atomic percentages on the surface, is more accurate and only analyzes the outer few nanometers of the coating. Analysis depth in XPS is usually under 10 nm, but the precise depth depends on the sample conductivity, anode type and material, X-ray beam power, detector, etc.

Figure 3-8. X-ray photoelectron spectrometer used in this study.

The parameters used for the acquisition of survey and high-resolution spectra are presented in Table 3-4.

Table 3-4. Acquisition parameters for survey and high resolution XPS spectra

	Start energy	End energy	Step width	dE	Dwell time	No. of scans	Beam power
Survey	1300 eV (Al anode)	0 eV	1 eV	4 eV	100 ms	5	150 Watts
High resolution	A small window around the peak		0.1 eV	0.3 eV	300 ms	10	300 Watts

This system is equipped with two side chambers which can perform plasma treatment, magnetron sputtering or ion treatment prior to sample analysis. The samples are kept in one of the side chambers in low pressure ($\approx 10^{-7}$ torr) for at least 24 hours before being transferred to the analysis chamber. Unless otherwise mentioned, no other pretreatment steps were taken on the samples before spectra acquisition.

CasaXPS software is used for analysis and interpretation of the spectra acquired from XPS. CasaXPS is a software developed by Casa Software Ltd. (USA) which is capable of spectrum calibration, peak identification, elemental quantification, component quantification, peak shape analysis and several other basic and advanced functions on XPS spectra. No supplementary charge neutralization system is installed on the XPS system used in this study, but charge compensation is performed on the data based on O 1s peak.

In CasaXPS, model peak shapes are expressed as a mathematical function. The most basic form of this function is GL(x), which identifies a mixture between a Gaussian peak and a Lorentzian peak, with x indicating the percentage of Lorentzian shape in the mixture. For instance, GL(0) is a Lorentzian shape, GL(100) is a Gaussian shape, and GL(50) is a shape between Gaussian and Lorentzian. GL is a symmetrical function, but a tail modifier can be

added to the GL function to accommodate non-symmetrical shapes. This modifier is indicated as T(x), and its effect on the peak shape is presented in Figure 3-9.

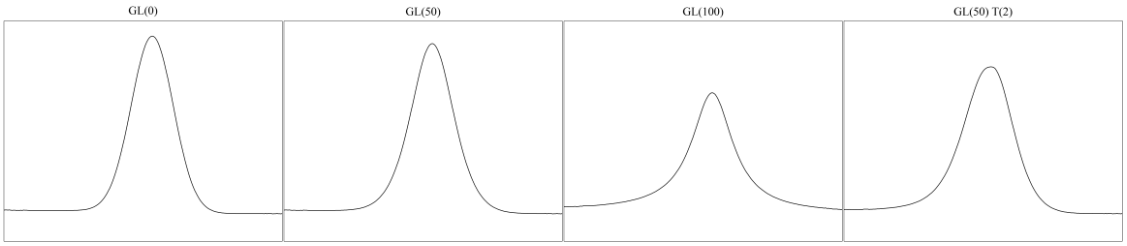

Figure 3-9. Some of the basic peak shape functions available in CasaXPS. Surface area under the peaks presented in this figure equal for all shapes.

The shape of a peak in XPS spectra can provide valuable information about the chemical states of the atoms. When comparing various spectra, similar peak shapes may be correlated to similar chemical states in different cases. Since the shape of the O 1s peak remains very close to GL (65) in all cases examined in this research, it can be concluded that the chemical state of oxygen does not change in different samples, and thus charge compensation can be safely done by calibrating O 1s peak to 532.0 eV.

To better characterize the chemical composition of the coatings, Si 2p core peak is fitted according to the method developed by O'Hare et al. for curve-fitting of Si 2p peak in siloxane based coatings [197,198]. In this method, four different chemical states of silicon are assumed to be present on the surface (Figure 3-10), and the energy shift for each one is accurately determined using standard samples. Each of these species are related to a function in siloxane coatings: M is a chain termination group, D is a chain propagation group and Q and T are both chain cross-linking groups [199]. These species along with their energy shift and their resulting peak position are presented in Figure 3-10 and Table 3-5.

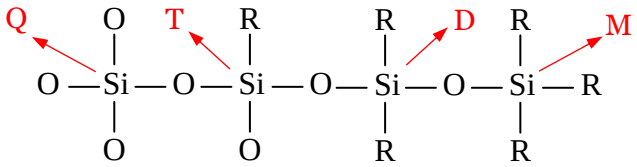

Figure 3-10. Various silicon chemical states in siloxane-based coatings. R denotes the organic functions here.

Table 3-5. Different siloxane species assumed to be present on the surface. The Q peak position is determined from the previous mesurements from a quartz sample and the energy shifts are taken from [197].

	Binding Energy	Energy Shift	Function
Q [$SiO_{4/2}$]	103.69 eV	0 eV	cross-linking
T [$CH_3SiO_{3/2}$]	102.89 eV	0.80 eV	cross-linking
D [$(CH_3)_2SiO_{2/2}$]	102.21 eV	0.68 eV	propagation
M [$(CH3)_3SiO_{1/2}$]	101.85 eV	0.36 eV	termination

Using high-density polyethylene (HDPE) and quartz standard samples, peak width (FWHM) is determined to be approximately 2 eV over the range of experimental conditions investigated here. Furthermore, for accurate curve-fitting of Si 2p core peak, the exact position of SiO_2 (Q in Table 3-5) component and the relative peak shape is determined using a standard UV grade quartz sample acquired from SwissJewel Company (USA). The result shows that the model peak shape for silicon species is GL(50)T(2) and the SiO_2 position is 103.69 eV (Figure 3-11). In all cases, Shirley background type is used for quantification of elemental peaks.

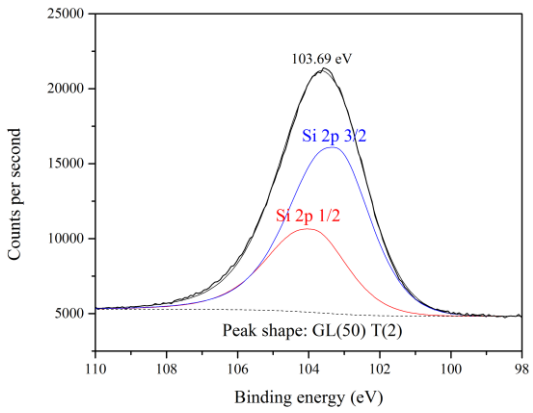

Figure 3-11. High resolution spectra of Si 2p core peak on a clean quartz sample.

3.9 HIGH SPEED IMAGING

A Photron SA1.1 (675K-M2) high-speed camera is used to record the droplet interaction with the superhydrophobic surface (5,400 frames per second) and the streamer discharges during pre-treatment (60,000 and 120,000 frames per second). To study the droplet impact mechanics, the DSA100 goniometer (section 3.5) is used with a supplementary light source to improve the controllability of the experiment.

3.10 ICE ADHESION STRENGTH MEASUREMENT

A horizontal wind tunnel operating in subzero temperatures is used to simulate natural atmospheric icing conditions. The schematics of this wind tunnel is presented in Figure 3-12. It is equipped with three water nozzles (Figure 3-13a) which are responsible for the generation of a super-cooled mist from which the ice accumulation occurs. Prior to icing, samples are kept at -10 °C for at least 1 hour. The samples are then mounted on aluminum beams (Figure 3-13b) and are placed vertically in the test section of the wind tunnel. The operational conditions of the wind tunnel are presented in Table 3-6.

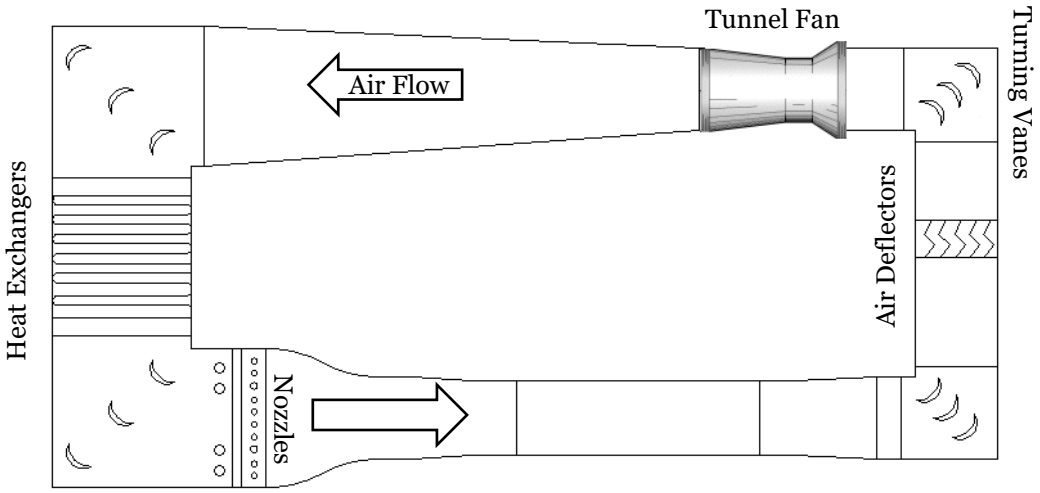

Figure 3-12. Icing conditions used in the wind tunnel to create atmospheric ice on the samples.

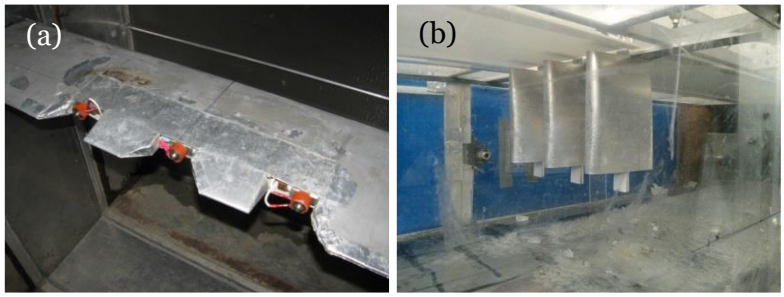

Figure 3-13. (a) Water nozzles and (b) three samples mounted in the test section.

Table 3-6. Icing conditions used in the wind tunnel to create atmospheric ice on the samples.

Wind velocity	Air temperature	Water pressure	Air pressure	Mean volume diameter	Liquid water content
10 m/s	-10 °C	325 kPa	100 kPa	63.3 µm	1.8 gr/m^3

It should be noted that these conditions are chosen to closely mimic the climatic conditions during a natural icing event. However, icing events can occur under different, and often fluctuating, conditions. Therefore, it is important to understand that the results presented in this thesis are limited to the specific conditions studied, and the effects of icing conditions on icephobic properties are not studied.

The samples are exposed to the conditions presented in Table 3-6 for 9 minutes before being transferred into a cold room at -10 °C and are kept there for at least 20 minutes before the deicing procedure using a centrifugal instrument. Deicing is performed by rotating the beams at a controlled speed and measuring the number of rotations per minute at which the ice detaches from the surface. The ice adhesion strength can then be determined through the following equation:

$$\tau = {mr\omega^2}/{A} \tag{3-1}$$

where τ is the ice adhesion strength (kPa), m is the mass of the accumulated ice (kg), r is the beam radius (0.17 m), ω is the rotational speed of the beam at the point of ice detachment (rpm), and A is the contact area between the ice and the surface (m^2).

3.11 ACCELERATED WEATHERING

To estimate the stability of the surface against UV exposure, a QUV accelerated weathering tester manufactured by Q-LAB (USA) is used. This accelerated weathering tester is capable of UV exposure and condensation. The 'accelerated' term indicates that a small period of exposure in the chamber may be correlated to a significantly longer time in natural conditions. According to the data gathered by Natural Resources Canada over a period of 20 years [200], the average annual sunlight energy in normal direction at a site located in Northern Quebec was measured to be 9-12 MJ/m^2. The accelerated weathering chamber was equipped with multiple UV lamps that can generate 0.89 W/m^2 of UV light. Since only 3-6 percent of natural sunlight is in the UV region, a simple calculation shows that 196 hours (rounded to 8 days) in the accelerated weathering chamber can be correlated to 1 year in natural conditions.

Multiple samples are exposed to up to 4 years of natural UV radiation and the effect of UV exposure on surface properties is studied.

3.12 CONCLUSION

In this chapter, the experimental aspects of this research work are presented. The procedures described in this chapter will be used to develop a superhydrophobic/icephobic coating and to characterize the resulting coating regarding its chemical composition, morphological structure, wetting behavior and icephobic properties. Furthermore, these experiments will evaluate surface durability against some aggressive natural factors, such as multiple icing/deicing cycles or UV radiation.

CHAPTER 4

TREATMENT OF ALUMINUM SAMPLES WITH N_2/O_2 PLASMA

4.1 INTRODUCTION

In this chapter, N_2 and N_2-O_2 (air) plasma treatments is described and the results from plasma and surface characterization experiments are presented. As will be seen, such process is introduced as a path to create a micro-roughened porous structure on the Al surface. This complex porous structure is used as a substrate for further deposition of hydrophobic materials.

4.2 TREATMENT PROCESS

As mentioned before, Al-6061 plates are cut into 160 x 40 mm pieces and are exposed to an APPJ operating in either N_2 or N_2-O_2 (air). Continuous operation combined with maximum generation power and short jet-to-substrate distance are used to ensure sufficient interaction between plasma and Al surface. Plasma-induced modifications are studied as a function of the number of passes. The conditions used in this step is presented in Table 3-2.

4.3 MORPHOLOGICAL CHARACTERIZATION OF THE SURFACE

Figure 4-1 compares optical images of the Al substrate after multiple passes of treatment with either N_2 or N_2-O_2 plasmas. As can be seen, the surface obtained after exposure to the N_2 plasma is comparable to the as received sample; this indicates minimal modification, at least over the scale of our observations. The yellowish color observed on the sample treated with N_2 plasma may be due to the nitridation of the surface. On the other hand, significant change in the surface morphology can be observed when the treatment is performed in air. More specifically, a highly porous and roughened Al surface is achieved, with typical dimensions in the micrometer scale.

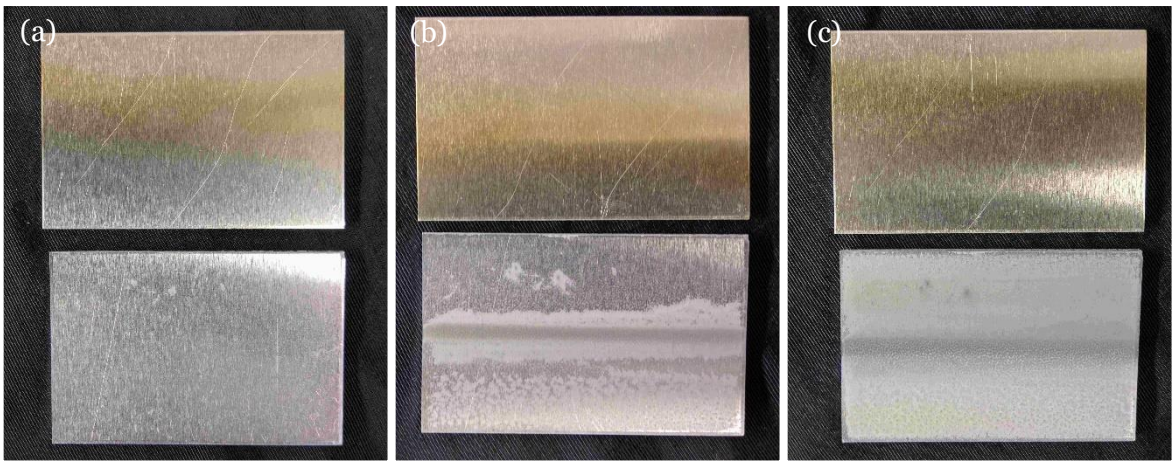

Figure 4-1. Digital images of Al samples (50 mm x 30 mm) treated with N_2 plasma (top) and N_2-O_2 plasma (bottom) after (a) first pass, (b) second pass, and (c) third pass of plasma treatment.

To better understand the physics driving such microstructure evolution after 3 passes of air plasma treatment, surface morphology is studied by SEM after each pass. Figure 4-2 shows a low magnification image of the surface along with a closer look at some of the specific structures observed. Based on the literature review provided in Chapter 2, it can be seen that these structures bear a significant resemblance to what is expected after laser ablation over a wide range of pulse durations and beam fluences, some of which are presented in the inset images of Figure 4-2(b) and Figure 4-2(c).

Figure 4-2(b) shows a circular feature observed on the surface after one pass of plasma treatment. This structure is similar to the holes drilled on the surface with ultrashort laser pulses (femtosecond pulses), which are capable of ejecting aluminum atoms from the surface without forming a liquid phase. It should be noted that in our case, the occurrence of such structures is noticeably rarer than the other two structures discussed in this section.

Figure 4-2(c) shows a different circular feature which is more commonly observed on the surface after one pass of plasma treatment. This feature is also similar to a different type of structure observed in the case of laser ablation. If the pulse duration is long enough for molten aluminum to form, typically in the pico/nanoseconds time scale, liquid phase is pushed away from the beam direction due to the recoil pressure of vaporized aluminum, leading to the features surrounding the drilled hole in the inset of Figure 4-2(c).

Figure 4-2(d) shows another structure commonly observed on the surface after one pass of plasma treatment. Similar to the previous two cases, this structure is also comparable to what may be expected from the phase explosions in laser ablation, typically observed for pulse durations in the nanosecond time scale and beam fluences above a threshold value. In this case, homogenous evaporation of molten aluminum leads to a micro-porous structure, similar to what is observed in Figure 4-2(d).

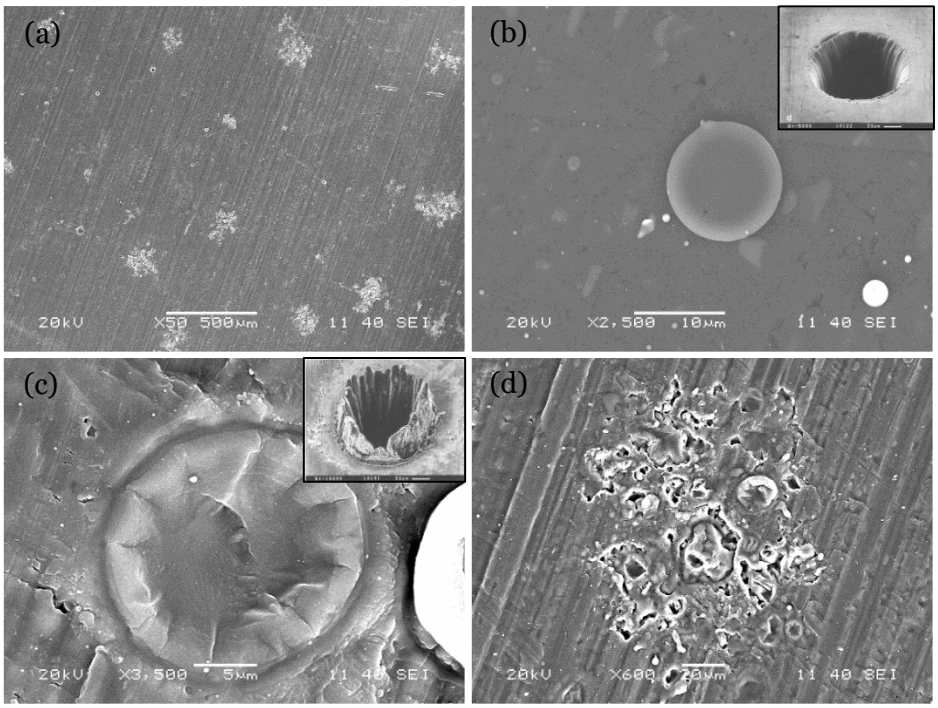

Figure 4-2. SEM images from the sample surface after one pass of air plasma treatment.

By exposing the aluminum surface to multiple passes of air plasma treatment, the features associated to femtosecond interactions (circular spots) and pico/nanoseconds interactions (circular spots with re-deposition on side walls) disappear, such that a uniform micro-porous and micro-roughened structure is observed over the whole substrate (Figure 4-3). Understanding the evolution mechanism of this structure is the main objective in this chapter.

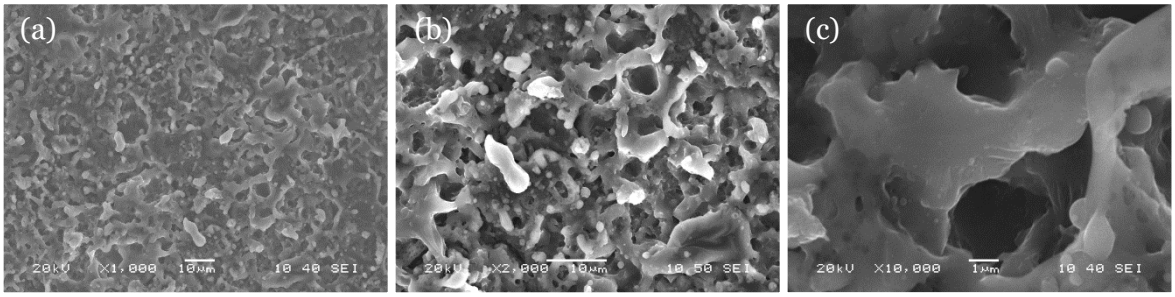

Figure 4-3. Micro-structure formed on the surface after 3 passes of air plasma treatment.

4.4 PLASMA CHARACTERIZATION

4.4.1 OPTICAL CHARACTERIZATION

Digital and high-speed imaging of the jet interacting with the aluminum surface is used to better understand the driving force behind the transformation process discussed in the previous sections. Over the range of experimental conditions investigated, the plasma source consists of small plasma filaments (or streamers), randomly distributed in time and space over the substrate surface. A typical digital image of the APPJ is shown in Figure 4-4 (left) for the N_2-O_2 (air) plasma open to ambient air. Significant color change is observed at the close proximity to the Al surface due to the significant plasma-substrate interactions; these aspects will be discussed in detail later, when reporting optical emission spectroscopy measurements. Optical images obtained with a sequence of 5400 frames per seconds are also displayed in Figure 4-4 (right). Streamer-like discharges produce multiple electric arcs that are randomly distributed in time and space over the Al surface. In the APPJ reactor used in this work, the occurrence of these arcs can be attributed to the transfer of electric charges from the rotating arc source (located in the jet body, see Figure 3-2) to the substrate surface (located below the jet) through the streamer discharge (conducting medium). This charge transfer is facilitated by the near-infinite electrical conductivity of the streamer. Some of these plasma-transferred arcs are presented in Figure 4-5.

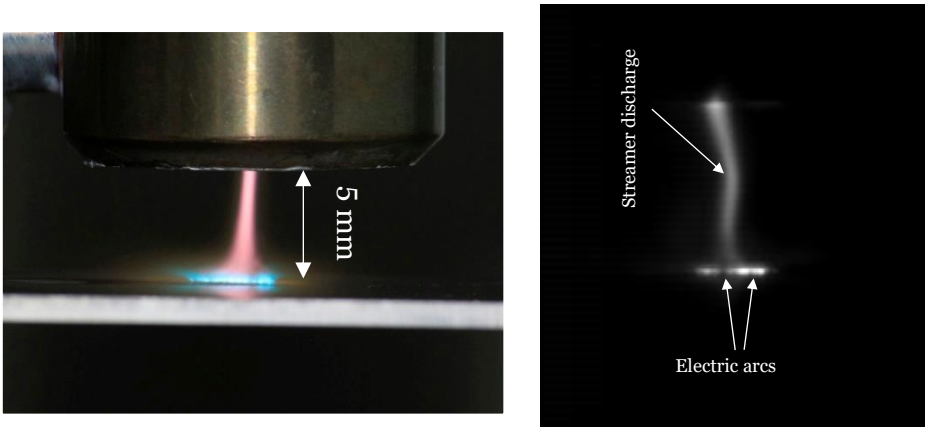

Figure 4-4. Digital image of the plasma jet interacting with the Al substrate (left) and evidence of electric arcs transferred on the surface (left).

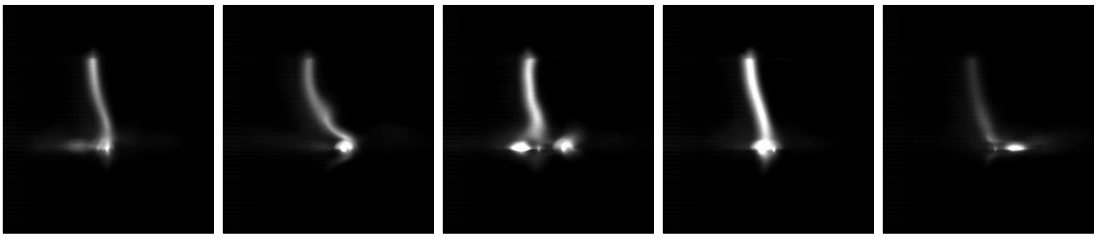

Figure 4-5. Examples of plasma-transferred electric arcs randomly distributed in time and space over the aluminum surface during air plasma treatment.

To examine the role of the plasma gas on the formation of the streamer discharge and electric arcs, high-speed sequences (60,000 frames per second) are captured from air and nitrogen plasma working close to the surface. It is shown that in the case of air plasma, streamer discharges are noticeably brighter and their duration seems to be much longer than in the case of nitrogen plasma (Figure 4-6). This is in agreement with the much more significant morphological change on the Al substrate observed after treatment by air plasma (note that no modification was observed after treatment by N_2 plasma, at least over the scale of our observations, see Figure 4-1). It is worth mentioning that the low brightness of the streamer discharges in nitrogen plasma makes it impossible to measure their exact duration, since unlike air plasma, it is impossible to distinguish between two consecutive discharges.

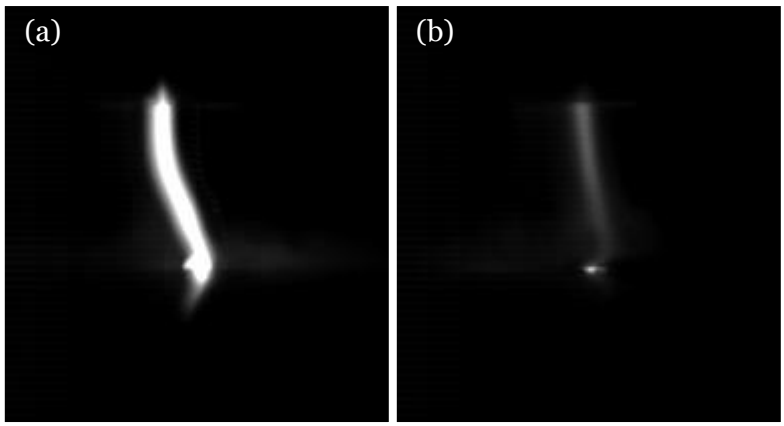

Figure 4-6. Typical streamer discharges during air plasma treatment (a) and nitrogen plasma treatment (b).

A sequence of images similar to Figure 4-6 was acquired with a frame rate of 120,000 frames per second to estimate the duration of each streamer discharge and plasma-transferred electric arcs in air plasma. Note that increasing the frame rate to 120,000 frames per second limits the maximum obtainable resolution to 128 x 32 pixels, and therefore these images are only used for the determination of time scale and are not presented here. It is found that the duration of a single streamer discharge is around 15 μs. However, arc duration can not be determined since the duration of each arc is much shorter than a single frame (~ 8 μs). This result thus confirms that plasma-based energy transfer reactions over a wide range of timescales are driving the observed transformation of the Al substrate after treatment with the APPJ operating in air.

4.4.2 OPTICAL EIMISSION SPECTROCSOPY

OES is used to monitor plasma-generated species in the APPJ operating in either N_2 or N_2-O_2 (air) gas mixtures. Figure 4-7 presents the optical emission spectra acquired for a jet-to-substrate distance of 5 mm. The range is limited to 200-500 nm since emission is very week above 500 nm. In the nominally pure N_2 plasma, the emission is mostly dominated by the N_2(C-B) rovibrational bands, with the emitting N_2(C) state being mostly populated by electron-impact excitation on ground state N_2(X). Similar to other APPJ reactors open to

ambient air, emission from OH(A-X) and NH can also be seen. Both emission bands are linked to the interaction between plasma-generated species and water vapors in humid air. For instance, it has been shown that in humid conditions, water molecules tend to react with plasma-generated N atoms, yielding OH and NH species [201]. Emission from NO can also be seen between 200 and 300 nm; a result ascribed to N atoms interacting with oxygen species present in ambient air (mostly O atoms formed by plasma-induced dissociation of O_2). Similar features are observed in the air plasma. In this case, as expected, NO emission is much more significant due to the higher oxygen content of the plasma.

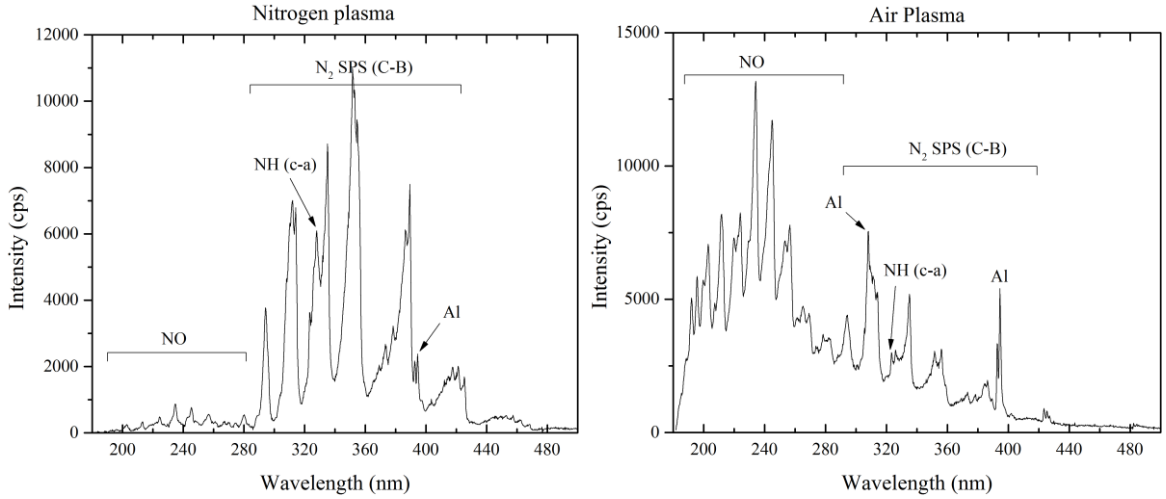

Figure 4-7. Optical emission spectra acquired from a nitrogen plasma (left) and air plasma (right) at a 5-mm distance from the jet head.

The significant plasma-Al interaction observed in the digital image of Figure 4-4 is also confirmed by the presence of atomic Al lines in the optical emission spectra through the peaks observed at 308, 309, 394.4, and 396.1 nm [202]. This can be explained by the ejection of Al atoms from the surface due to the high-energy impacts associated to the presence of streamers and plasma-transferred arcs. Comparing the two spectra presented in Figure 4-7, it can be deduced, from the analysis given above, that nitrogen plasmas cannot provide as much energy to the surface as air plasma, leading to a significantly weaker interaction and thus much weaker emission line intensities of atomic aluminum at 394.4 and 396.1 nm.

In order to confirm the presence of atomic aluminum in the spectra, another experiment is performed by replacing the aluminum substrate with a stainless-steel substrate. The results are presented in Figure 4-8. The absence of Al peaks in the spectrum related to the stainless-steel sample confirms that the atomic aluminum observed in the plasma is in fact due to plasma-aluminum interactions, and not from the jet components or other unaccounted sources.

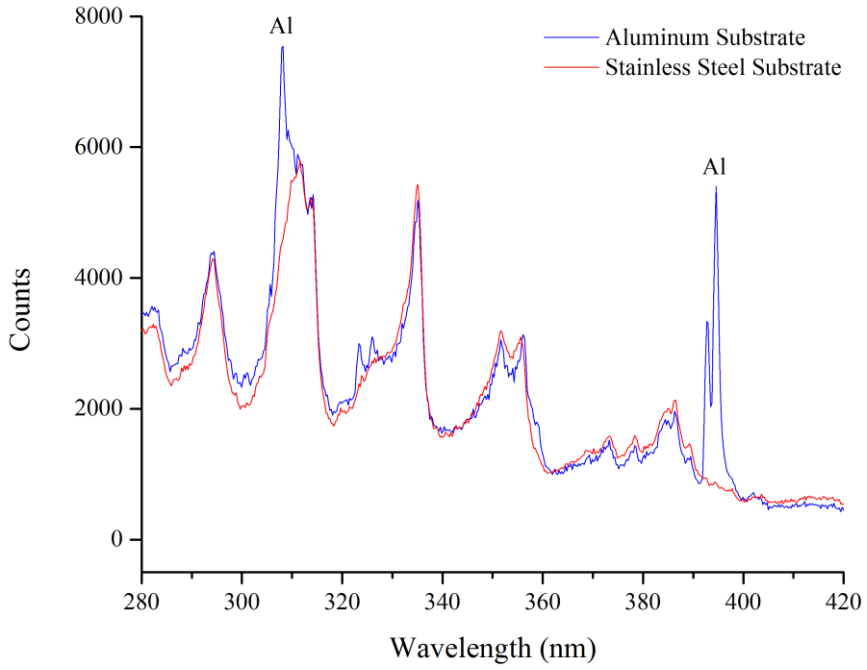

Figure 4-8. Optical emission spectra acquired from the plasma working on an aluminum sample and a stainless-steel sample.

4.5 CHEMICAL CAHRACTERIZATION OF THE SURFACE

The chemical composition of the air-treated surface is studied through XPS analysis. To ensure that surface contamination does not affect the spectra, the samples are cleaned using an argon ion gun for 5 minutes. During the ion treatment, generation power is set to 75 watts and the emission voltage is set to 2.5 kV. In comparison with common procedure, these are relatively mild conditions, which minimize the unwanted effects of ion treatment on the surface composition.

The results of survey quantification are presented in Table 4-1. The chemical composition of the pre-treated sample is almost identical to what one would expect from Al_2O_3, while the aluminum control sample exhibits an Al/O ratio which is higher than that of Al_2O_3.

Table 4-1. Atomic quantification of the porous structure compared to the aluminum control sample

	Aluminum (Atomic %)	Oxygen (Atomic %)
Pre-treated Sample	39.72	60.28
Al Control Sample	42.40	57.60

This is further confirmed by Al 2p core peak high resolution spectra, presented in Figure 4-9. The results suggest that in Al control sample, the thickness of the oxide layer on the surface is less than the analysis depth of the X-Ray (which is around 10 nm). However, after air plasma treatment the metallic shoulder in Al 2p core peak is removed. Figure 4-9 further confirms that from a purely chemical point of view, air plasma treatment highly oxidizes the surface, resulting in a thicker Al_2O_3 layer.

It should be noted that the peak width is restricted to 3 ± 0.1 eV for aluminum oxide component and to the half of that for metallic aluminum component. In addition, the residual for both fits are less than 5, which confirms the mathematical accuracy of the fit.

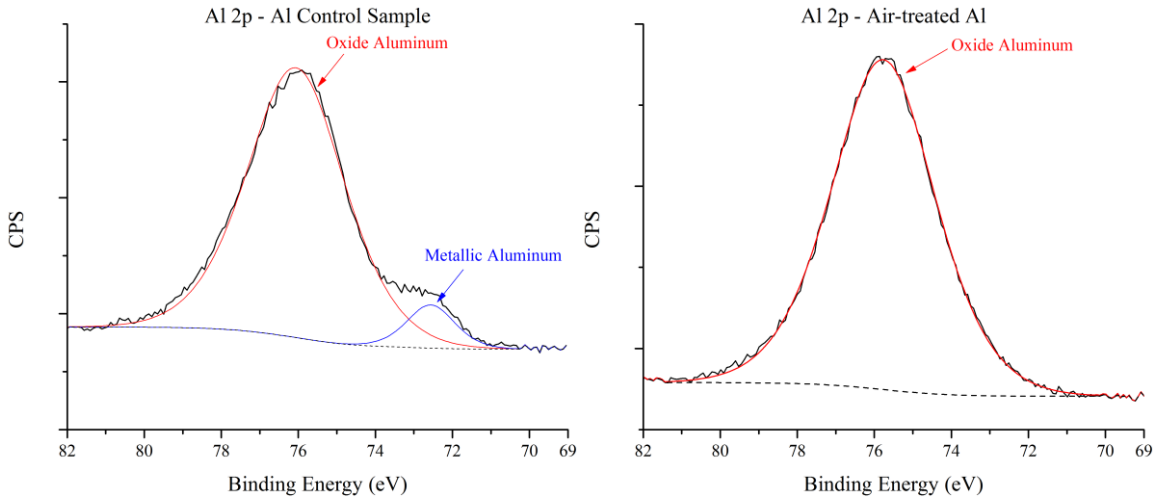

Figure 4-9. Al 2p core peak high resolution spectra for aluminum control sample (left) and pretreated sample (right)

By combining the results from SEM and XPS, one thus concludes that the creation of micro-porous and micro-roughened Al surface by air plasma treatment is accompanied by significant substrate oxidation. Therefore, both physical (as in laser ablation) and chemical (as in oxidation) mechanisms are involved in surface transformation.

4.6 DISCUSSION

As mentioned before, the structures observed on the surface after one pass of air plasma treatment bear a significant resemblance to what may be expected after laser ablation with various pulse durations, from femtoseconds to pico/nanoseconds. As described in literature review, various pulse durations and beam fluences lead to various surface features, all of which are observed in our case.

In laser ablation, laser pulses in the fluence range of 2 – 4 J/cm^{-2} are used. In order to draw similarities between laser ablation and APPJ treatments, both techniques must involve a comparable energy flux to the surface. As an example, Chichkov et al. used 3.5×10^4 laser pulses, each with a pulse duration of 250 ps and an energy of 0.5 mJ, to drill holes with a diameter of approximately 200 μm on the surface of aluminum nitride (Figure 4-10). In

this case, the total amount of energy being delivered to the surface per unit of time and area can be calculated:

$$E_{Laser} = \frac{\text{Number of pulses} \times \text{Pulse energy}}{\text{Pulse time} \times \text{Affected area}} = \frac{(3.5\times10^{4})\times(0.5\times10^{-3}J)}{(250\times10^{-12}s)\times[\pi\times(100\times10^{-6}\ m)^{2}]}$$

$$= 2.23\times10^{13}\ {}^{W}/_{m^{2}} \qquad (4\text{-}1)$$

In the case of APPJ treatments, similar features to Figure 4-10(c), even though smaller, are observed. The diameter of these features, from which an example is presented in Figure 4-10(d), is measured to be around 10 μm. As an upper energy limit, and a crude approximation, it is assumed that the entirety of the plasma power (7.5 kW) is being transferred locally to the aluminum surface. It is assumed that this energy transfer takes place over the size of the observed features (10 μm) and over a very short period of time associated with the presence of streamers and plasma-transferred electric arcs. Therefore, the total amount of energy being delivered to the surface per unit of time and area can be calculated:

$$E_{APPJ} = \frac{\text{Generation power}}{\text{Affected area}} = \frac{7500\ {}^{J}/_{s}}{\pi\times(5\times10^{-6}\ m)^{2}} = 9.6\times10^{13}\ {}^{W}/_{m^{2}} \qquad (4\text{-}2)$$

By comparing the energy flux values acquired from equations 4-1 and 4-2, one concludes that the energy flux in both cases is of the same order of magnitude such that the analogy between laser ablation processes and AAPJ treatments is highly plausible. It should be noted, nonetheless, that since most studies on laser ablation do not mention the full set of data required for such energy calculations, these values are determined based on a single case of picosecond laser pulse treatment.

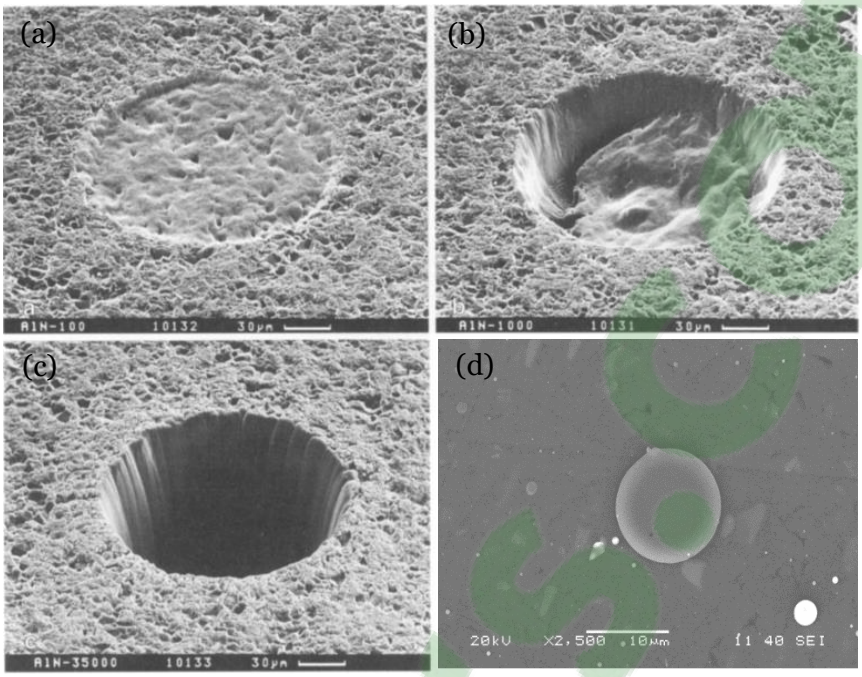

Figure 4-10. Femtosecond ablation of a 0.8 mm AlN target with 250 fs, 0.5 mJ, and F = 2.5 J/cm² second harmonic radiation (λ= 390 nm) and different number of pulses: (a) 10, (b) 10^3, (e) 3.5 × 10^4 laser pulses and (d) a similar feature observed in plasma assisted arc treatment [186].

It is worth highlighting that due to surface irregularities, some points on the aluminum surface are expected to have different electrical characteristics. Furthermore, air plasma can oxidize the surface, creating a dielectric region and adding to these surface irregularities. These regions can accumulate electric charge and create a relatively large electric field, which subsequently can induce arcing between the source and the substrate. Therefore, the presence of a streamer discharge can lead to multiple plasma-transferred electric arcs in the vicinity of such points. Since these arcs occur at seemingly random spots close to the endpoint of the streamer discharge, such phenomena could be the driving force behind the observed surface transformation (Figure 4-11).

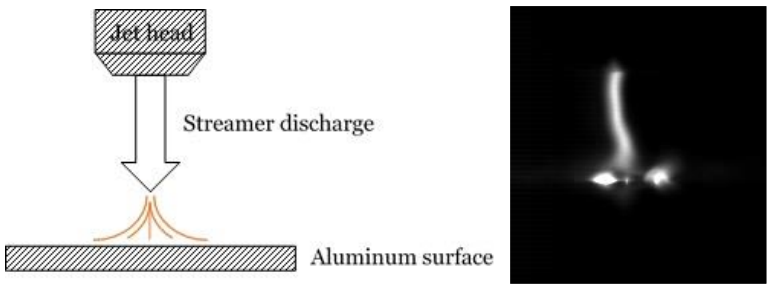

Figure 4-11. The location of electric arcs relative to the streamer discharge (left) and a high-speed image demonstrating the streamer discharge and electric arcs on the surface (right).

More specifically, the circular features observed on the aluminum surface after only one pass of APPJ treatment (Figure 4-2b) are similar to the holes drilled by laser ablation with ultrashort laser pulses (note that the energy flux delivered by plasma-transferred arcs was shown to be comparable to that of laser pulses). However, the scarcity of these features on the surface indicates that ultrashort electric arcs are not very common in APPJ. On the other hand, the circular features with significant sidewall re-deposition presented in Figure 4-2(c) are more common, and can be due to longer arc durations with low energy in the range of nanoseconds. This is consistent with our observations highlighting that plasma-transferred arcs have durations much below the minimal time frame of our high-speed optical imaging experiment (much shorter than microsecond scale). Finally, the structure observed in Figure 4-2(d) can be linked to either longer arcs, in the range of microseconds, or to a nanosecond arc with higher energy. Both are expected to induce a phase explosion on the aluminum surface resulting in a micro-porous and micro-roughened structure. This significant interaction is confirmed by the presence of aluminum vapor peaks in the optical emission spectra (Figure 4-7). With each pass of plasma treatment, more surface irregularities are introduced to the surface structure, facilitating the formation of longer and stronger electric arcs during treatment. For instance, a phase explosion site formed in the first pass may be a preferred location for the occurrence of plasma-transferred electric arcs in the second pass. Therefore, by exposing the surface to multiple treatment passes, a

uniform surface structure is formed, which is very similar to the texture of phase explosion sites.

4.7 CONCLUSION

In this chapter, the effects of air plasma treatment on the surface of Al-6061 is discussed. This process is introduced as a path to generate a micro-porous and micro-roughened structure as a substrate for further deposition of hydrophobic materials. It is shown that a streamer discharge forms through the plasma column between the APPJ source and the substrate surface. This discharge leads to the occurrence of multiple, plasma-transferred electric arcs on the surface that are believed to be the driving force behind the transformation mechanism. Energy transfer reactions leading to phase explosion and thus to micro-porous and micro-roughened structure is accompanied by significant oxidation of the surface due to the high oxygen content of the air plasma.

CHAPTER 5

TREATMENT OF ALUMINUM SAMPLES WITH N_2/HMDSO PLASMAS

5.1 INTRODUCTION

In this chapter, the details of nitrogen plasma treatment process in depositing environment in the presence of HMDSO is discussed. At first, the effects of monomer flow rate and ionization gas on surface properties are presented. Then, a simple modification to the jet is proposed that can significantly affect the surface morphology and facilitate the development of superhydrophobic coatings. Based on this modification, multiple superhydrophobic/icephobic samples are prepared using various plasma parameters. These samples are then studied regarding their surface topography, chemical composition, wetting behavior and icephobic properties to understand the effects of monomer flow rate, plasma power and number of deposition passes on surface characteristics.

5.2 EFFECT OF MONOMER FLOW RATE AND IONIZATION GAS

14 different values of monomer flow rate are chosen (3, 4, 5, 6, 7, 8, 10, 15, 20, 30, 40, 50, 60, 70 g/h) and plasma deposition is carried out using two different ionization gases. For each individual condition, 2 identical samples are created and static contact angle is measured 5 times on each sample. The results are presented in Figure 5-1.

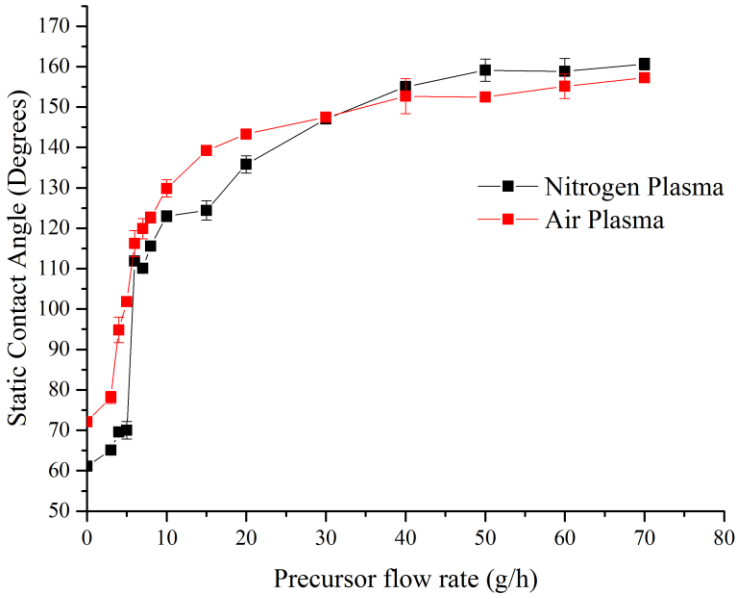

Figure 5-1. Contact angle vs. monomer flow rate for different ionization gases: N_2 and N_2-O_2 (air).

Static contact angle on untreated aluminum is around 90 degrees. It is shown that air or nitrogen plasma treatment without monomer injection decreases the contact angle of aluminum. This can be explained by the fact that plasma activation can lead to the formation of various oxygen and nitrogen compounds on the surface, which are known to be hydrophilic and can increase the surface energy. Nitrogen functions are usually considered to have higher surface energy compared to oxides, and therefore nitrogen plasma treatment will lead to a greater decrease in the contact angle.

On the other hand, for flow rates higher than 40 g/h, the contact angle in both cases remains almost constant. This can be explained by the complete coverage of the surface at a flow rate around 40 g/h. Increasing the flow rate beyond this point does not seem to change the surface morphology or chemical composition. However, it should be noted that as the precursor flow rate increases, a white powder forms on the surface. In the case of organosilicon precursors in open-air configuration, such powders most likely correspond to silica and can decrease the mechanical stability of the coating. Therefore, it is essential to

identify a condition in which superhydrophobicity can be achieved without the excessive formation of such powders.

To investigate the effect of ionization gas on the surface structure, SEM images are acquired from the two samples polymerized at the same flow rate (70 g/h) using either N_2 or air plasma. The images are presented in Figure 5-2.

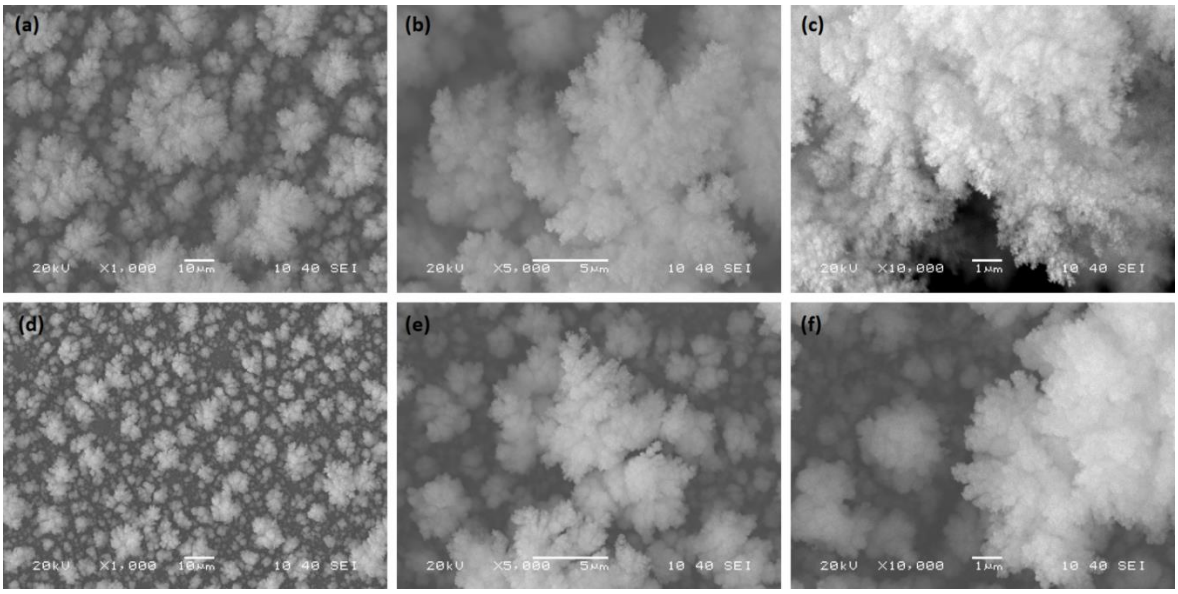

Figure 5-2. SEM images of coatings polymerized under air plasma (a-c) and nitrogen plasma (d-f) with various magnifications.

From Figure 5-2, in both cases, the coating consists of dendrite-like structures with multiple levels of roughness. Similar hierarchical structures have been identified in various cases of chemical vapor deposition processes and are usually referred to as cauliflower-like surfaces [203,204] due to their apparent similarity to cauliflower. The formation of these structures is generally attributed to some sort of non-uniformity in thin film growth. The mathematical equations governing the topography of such deposition fronts are beyond the scope of this thesis, but a detailed physical model is defined in [203] which shows perfect agreement with experimental data.

Hierarchical multi-leveled surface structures have proven to be ideal for superhydrophobic and specifically for icephobic applications [89]. From Figure 5-2, it can also be seen that nitrogen plasma leads to significantly smaller features on the surface. This has been previously reported by others [205], where addition of nitrogen or argon to air plasma was shown to reduce the size of the deposited particles. As mentioned before, smaller surface features may facilitate the manifestation of Cassie-Baxter wetting regime, which exhibits lower contact angle hysteresis and higher droplet mobility compared to Wenzel wetting regime. Contact angle hysteresis is a deciding factor in icephobic applications. This, along with the lower presence of oxide functions in nitrogen plasma, makes nitrogen a more suitable choice for this work.

5.3 POWDER FORMATION DYNAMICS

As mentioned before, the formation of silica powders on the surface at high flow rates may lead to a weakened surface structure with low mechanical stability. To understand the powder formation dynamics, the effects of flow rate and jet-to-substrate distance on surface structure are studied.

In the first step, samples are prepared under five different flow rates (3, 5, 10, 15, 30 g/h) with a constant jet-to-substrate distance (10 mm). Surface structure are studied using SEM and the results are presented in Figure 5-3. At low flow rates (Figure 5-3a and Figure 5-3b), a spherical deposition was observed on the surface. As the flow rate increases, these particles form some agglomerates while losing their spherical shape, thus increasing the roughness.

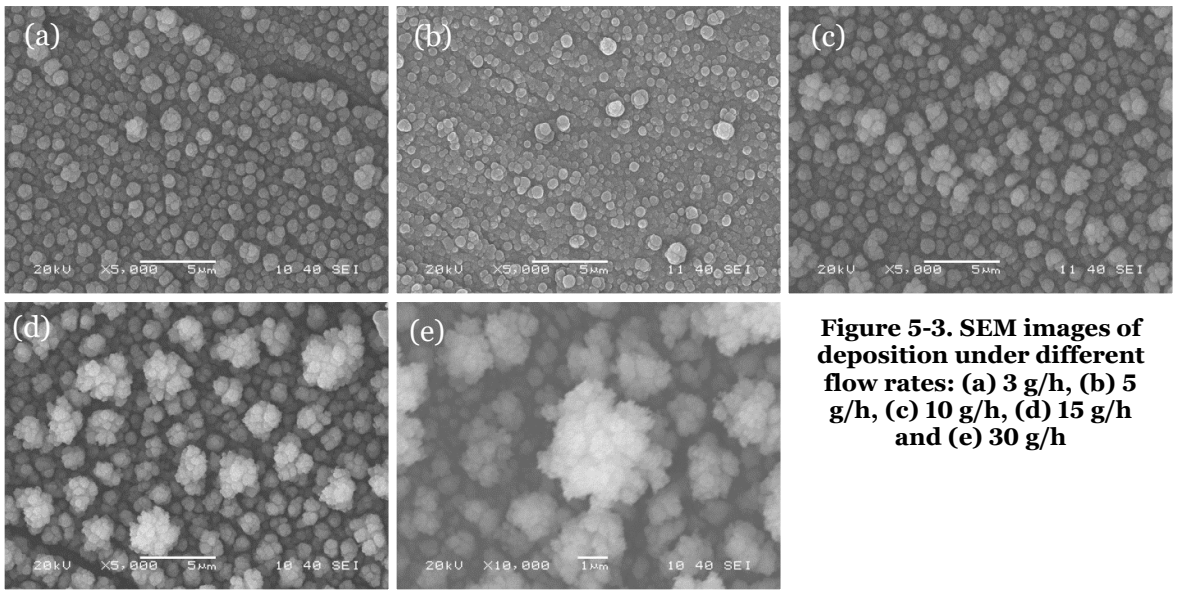

Figure 5-3. SEM images of deposition under different flow rates: (a) 3 g/h, (b) 5 g/h, (c) 10 g/h, (d) 15 g/h and (e) 30 g/h

To further clarify this mechanism, two flow rates in each morphological regime (3 g/h for spherical and 30 g/h for agglomerates) are chosen and the effect of jet-to-substrate distance on surface morphology is studied (Figure 5-4). It is shown that the effect of jet-to-substrate distance is not as pronounced as the effect of monomer flow rate, but one may observe that increasing the jet-to-substrate distance while keeping the flow rate constant will increase the number of agglomerates in spherical regime and increase the size of the agglomerates in agglomerate regime. This is consistent with an increase of gas phase dissociation reactions as the residence time of plasma generated species increases with jet-to-substrate distance.

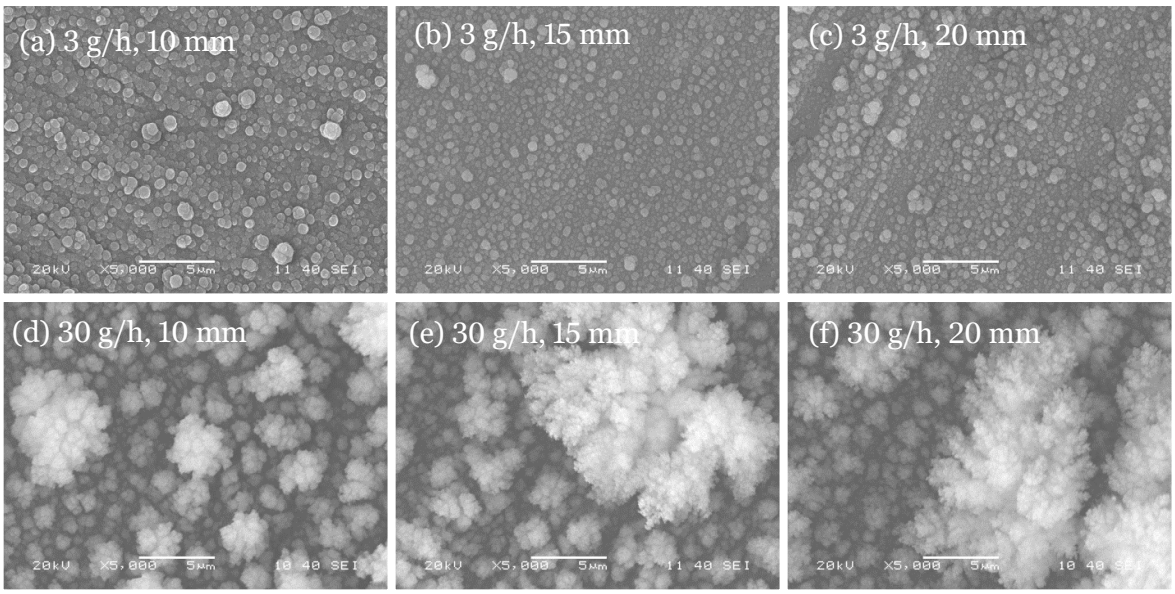

Figure 5-4. SEM images of samples polymerized under HMDSO flow rate of 3 g/h (top) and 30 g/h (bottom) at different jet substrate distances: (a) and (d) 10 mm, (b) and (e) 15 mm, (c) and (f) 20 mm.

5.4 JET MODIFICATION

To facilitate the formation of a superhydrophobic coating, plasma jet is slightly modified. Using a simple hand-made copper clamp, a quartz tube with a diameter of 25 mm and a length of 30 mm is mounted on the jet-head (Figure 3-3). This tube affects the deposition process in a number of ways:

- It confines the plasma in a closed space, and therefore reduces oxygen diffusion into the plasma, leading to more organic coatings.
- It makes the generation and maintenance of a very weak plasma possible, which leads to lower monomer fragmentation and is generally favorable in hydrophobic applications.

Plasma composition in the presence of the quartz tube is studied using OES and the results are presented in Figure 5-5. Since the ionization gas flow rate and the precursor flow rate are identical in both cases, higher intensity of the bands in the case of the sample created in the presence of the quartz tube is suggestive of a higher plasma density, at least at the

position of OES measurements (sample surface). It is worth mentioning that the presence of Si lines is suggestive of significant precursor fragmentation. Atomic Si lines are rarely observed during plasma polymerization in cold, atmospheric-pressure plasmas; this can most likely be attributed to the much higher electron densities and temperatures in the streamer-based discharges than in other systems such as homogeneous dielectric barrier discharges [206].

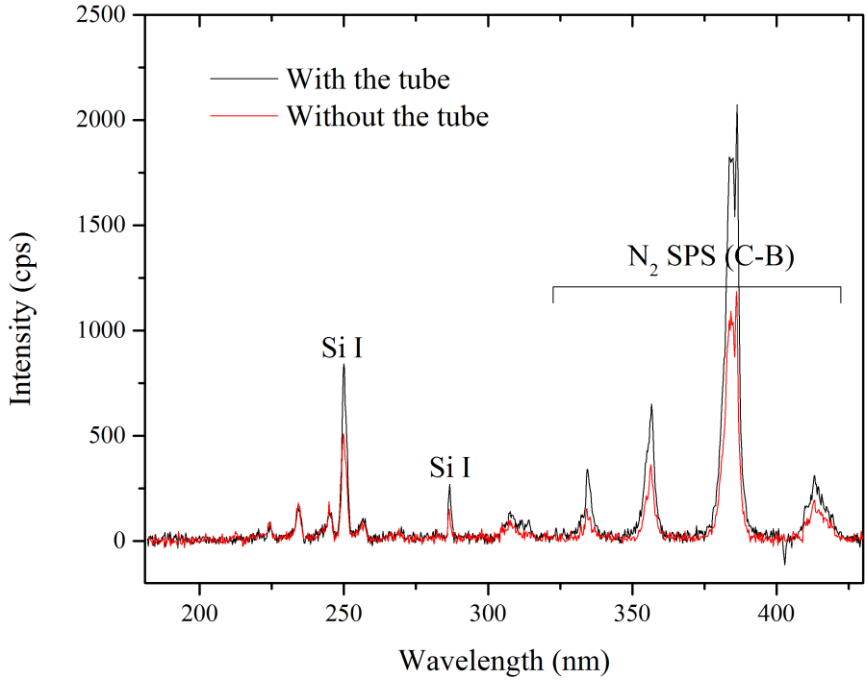

Figure 5-5. OES spectra acquired from the plasma with and without the quartz tube surrounding the jet-head.

To study the effect of this modification on surface properties, two samples are prepared using nitrogen plasma with an HMDSO flow rate of 5 g/h with and without the quartz tube surrounding the jet. Figure 5-6 shows the surface structure after plasma deposition without the quartz tube. In this case, deposition consists of spherical nanoparticles covering the micro features obtained after the pre-treatment step (Chapter 4). These particles seem to be distributed uniformly on the surface and their diameter range from a few to hundreds of nanometers.

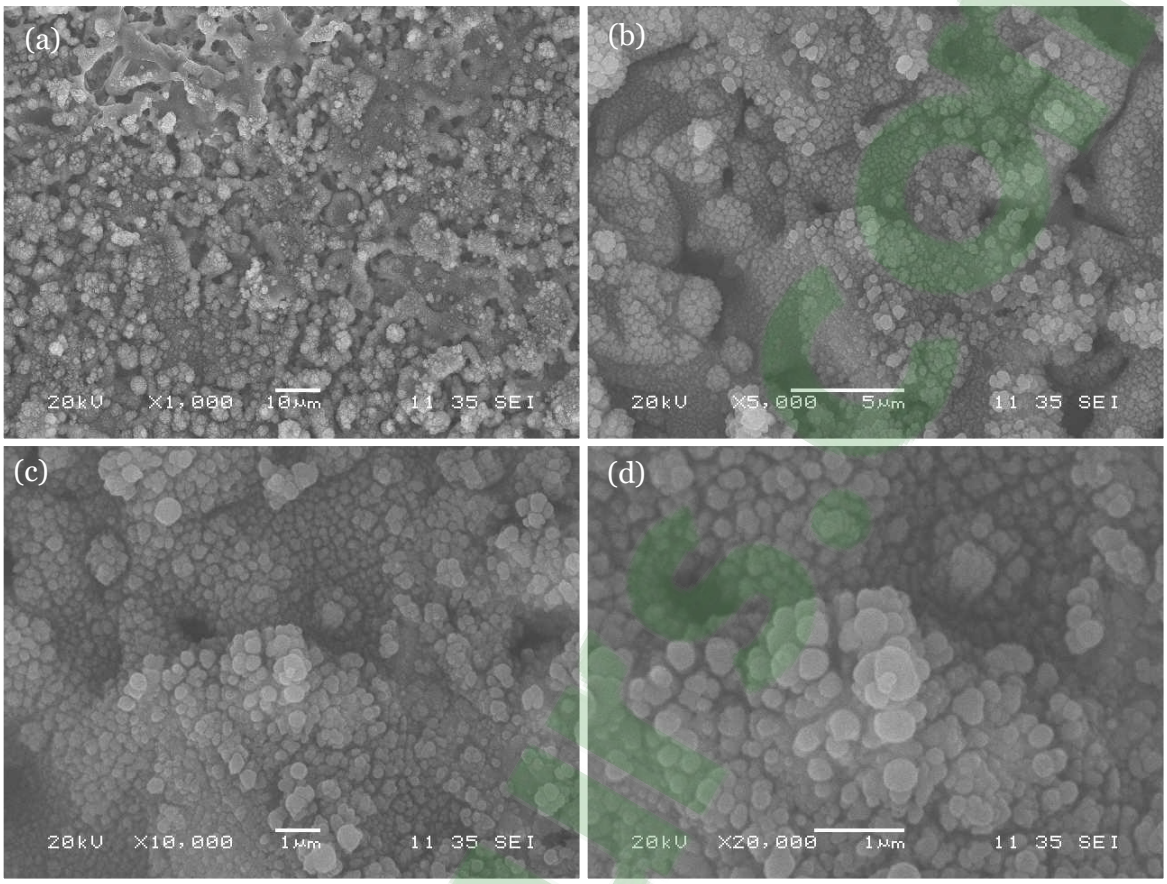

Figure 5-6. Surface structure of the coating deposited in the absence of quartz tube with nitrogen plasma and 5 g/h of precursor flow rate on pre-treated surfaces.

SEM images of the coating deposited in the presence of the quartz tube are presented in Figure 5-7. In this case, surface structure is consisted of dendrite-like structures with multiple levels of roughness, ranging from tens of micrometers to only a few nanometers. As mentioned before, such structure is ideal for hydrophobic applications, and since this structure is developed using a relatively low precursor flow rate, the formation of silica powder is expected to be minimal. Similar features have been reported by Kilicaslan et al. during the deposition of HMDSO-based nanomaterials in atmospheric-pressure plasmas sustained by microwave electromagnetic fields [207]. While spherical silica nano-particles were obtained in the presence of O_2 in Ar/HMDSO plasma, dendrite like SiOCH nanostructures were formed in the absence of O_2.

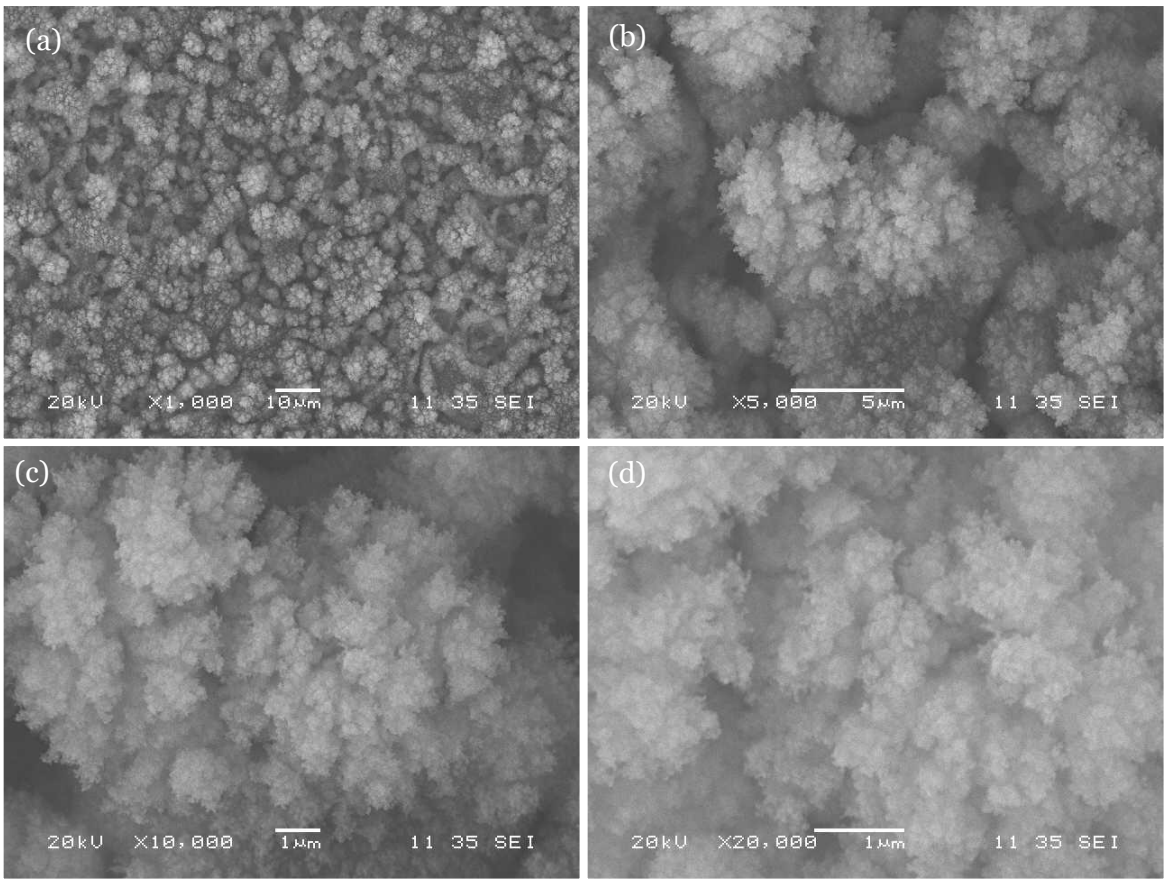

Figure 5-7. Surface structure of the coating deposited in the presence of quartz tube with nitrogen plasma and 5 g/h of precursor flow rate on pre-treated surfaces.

Chemical composition of the samples acquired from nitrogen plasma deposition with and without the quartz tube surrounding the jet is also studied using FTIR spectroscopy and the results are presented in Figure 5-8. Si-$(CH_3)_n$ group is easily recognizable by a strong, sharp band at around 1275 cm^{-1} (CH symmetric deformation in Si-CH_3) together with three bands in the range of 865-750 cm^{-1}.

The intense band between 1000 cm^{-1} and 1200 cm^{-1} is generally assigned to Si-O-Si and Si-O-C asymmetric stretching modes [208]. This band is usually assumed to be the sum of three Gaussian components which correspond to different bond angles in Si-O-Si: TO_2 mode at 1120 cm^{-1} (170°-180° bond angle), TO_1 mode at 1070 cm^{-1} (140° bond angle), and TO_3 mode at 1030 cm^{-1} (120° bond angle). TO_1 mode is typically related to crystalline silicon

dioxide, which is the most stable form of silicon oxide in normal condition and is sometimes referred to as α-quartz. TO_2 mode is often associated to fragments of Si-O-Si chains, but in organic films this wavenumber is also populated by Si-O-C stretching mode. In Figure 5-8, the position of this band in the sample prepared with the quartz tube is closer to TO_3 mode. This mode is related to coesite-like structures, but in $SiO_xC_yH_z$ films, such low Si-O-Si bond angle is often observed because of the methyl environment of the bond [209]. On the other hand, a shift to higher wave numbers is observed in the sample prepared in the absence of the quartz tube, suggesting that without the tube this region is dominated by either Si-O-C bonds or Si-O-Si bond in TO_2 mode, which may be associated with the fragments of Si-O-Si chains. This, along with the lower deposition in the case without the quartz tube, suggests that the addition of the quartz tube to the plasma jet leads to more organic and probably longer chains of $SiO_xC_yH_z$ structures.

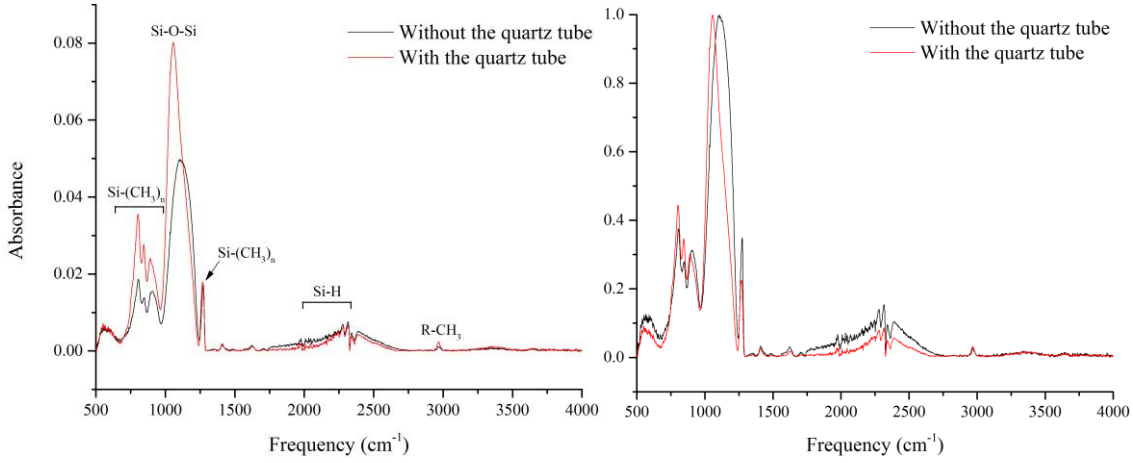

Figure 5-8. absolute (left) and normalized (right) FTIR spectra of samples prepared with nitrogen plasma deposition of HMDSO with a flow rate of 5 g/h, with and without the quartz tube surrounding the jet.

5.5 INITIAL PLASMA CONDITIONS

At this point, the initial plasma deposition conditions can be identified for further investigation. All samples discussed here are prepared with N_2/HMDSO plasma after the jet modification on pre-treated aluminum surfaces (Chapter 4). Three different precursor flow

rates are chosen: 3 g/h, 5 g/h, and 7 g/h, resulting in PT3, PT5 and PT7, respectively. To study the effect of the number of deposition passes on surface properties, PT3x3 is prepared with the same conditions as PT3 but with 3 passes of plasma deposition. Similarly, PT5x3, and PT5x6 are prepared with the same conditions as PT5 but with 3 and 6 passes of plasma deposition, respectively. Finally, to study the effects of plasma power on surface properties, PT5P75 is prepared using the same conditions as PT5 but with increased plasma power. Deposition conditions were previously presented in Table 3-3. A specific point should be made about jet-to-substrate distance in plasma deposition, as it is much larger than that of the pre-treatment process. This ensures that that the plasma-surface interactions are driven by the deposition of plasma-generated species, rather than by energy transfer processes as discussed in Chapter 4. Table 5-1 clarifies the difference between the samples investigated in the following sections.

Table 5-1. Plasma conditions used for preparation of samples studied here.

	Precursor flow rate (g/h)	Plasma generation power (kW)	Number of deposition passes
PT3	3	2.7	1
PT3x3	3	2.7	3
PT5	5	2.7	1
PT5P75	5	3.6	1
PT5x3	5	2.7	3
PT5x6	5	2.7	6
PT7	7	2.7	1

5.6 SUPERHYDROPHOBIC/ICEPHOBIC COATINGS

5.6.1 SURFACE MORPHOLOGY

SEM is used to study the effects of plasma parameters on the surface structure and the results are presented in this section.

Figure 5-9 shows the effect of precursor flow rate on surface morphology. Comparing different surface structures at different monomer flow rates, one can conclude that the only condition where surface features originating from the pre-treatment and surface features originated from plasma polymerization are sufficiently pronounced simultaneously is PT5. In PT3, precursor flow rate is not sufficient for complete coverage of the pre-treated surface. On the other hand, in PT7, the pre-treated surface porosity is largely covered by the coating, and therefore a significant level of roughness is lost. For the sake of brevity, this phenomenon will be referred to as '*morphological saturation*' for the rest of this document. It should be noted that SEM images in Figure 5-9 are acquired with a different instrument and therefore they may look slightly different from other images presented in this section.

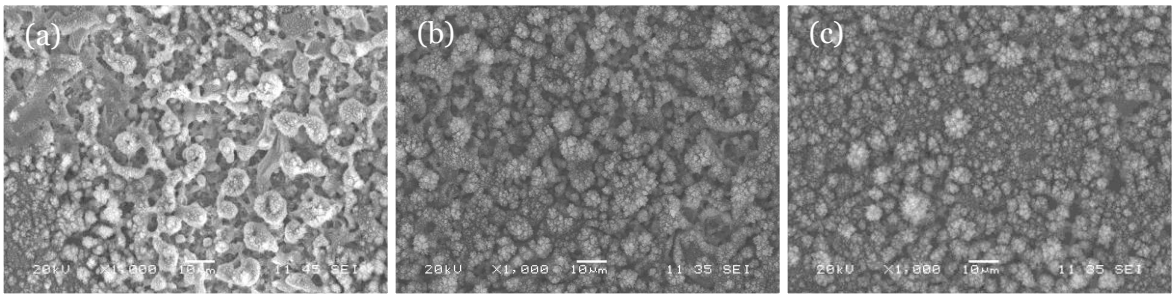

Figure 5-9. SEM images of (a) PT3, (b) PT5, and (c) PT7

Figure 5-10 shows SEM images of PT3 and PT3x3. It is shown that multiple passes of plasma deposition in this case will lead to a thicker coating and larger deposited features on the surface. In both cases, multiple levels of roughness are observed, ranging from tens of micrometers to a few nanometers. However, in the case of PT3x3, particle agglomeration gives rise to an extra level of roughness which contributes to the icephobic properties.

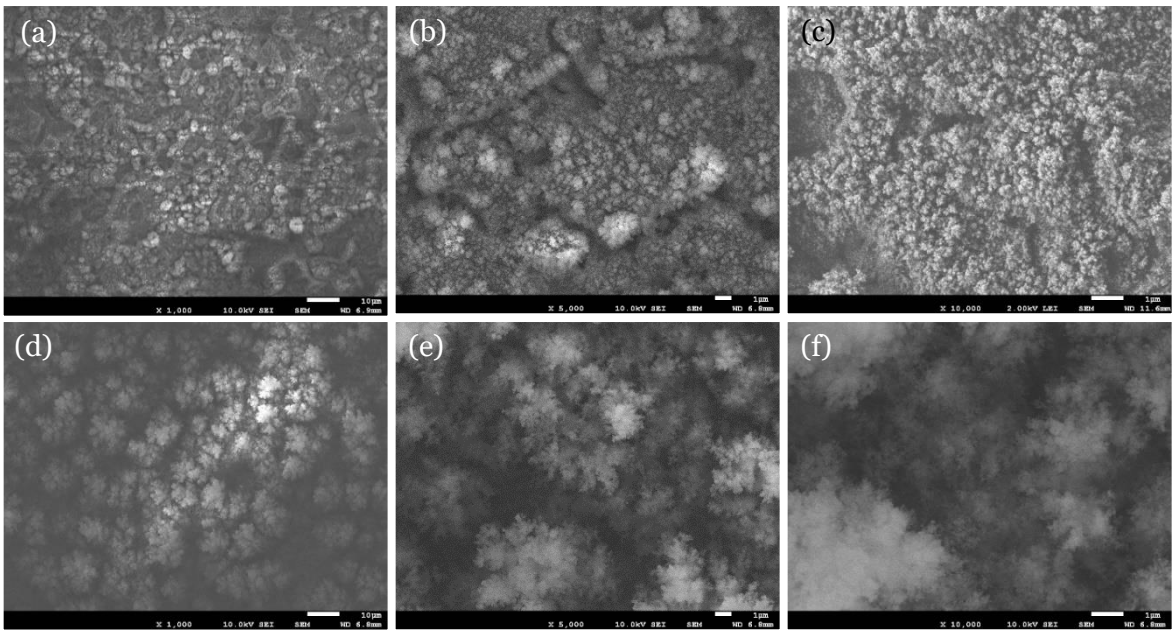

Figure 5-10. SEM images of PT3 and PT3x3: (a) PT3 1000x, (b) PT3 5000x, (c) PT3 10000x, (d) PT3x3 1000x (e) PT3x3 5000x and (f) PT3x3 10000x

Figure 5-11 shows SEM images of PT5, PT5x3 and PT5x6. Similar to the case of PT3 and PT3x3, multiple passes lead to a thicker coating and larger agglomerates on the surface. However, since monomer flow rate is higher in this case, large agglomerates are observed even after one pass of plasma deposition.

Figure 5-12 shows the SEM images of PT5P75 with two different magnifications. Comparing Figure 5-12(a) with Figure 5-11(a), it seems that the effect of plasma power on surface morphology is minimal. However, as will be discussed later in section 5.6.2, the chemical composition of PT5P75 varies significantly with that of PT5.

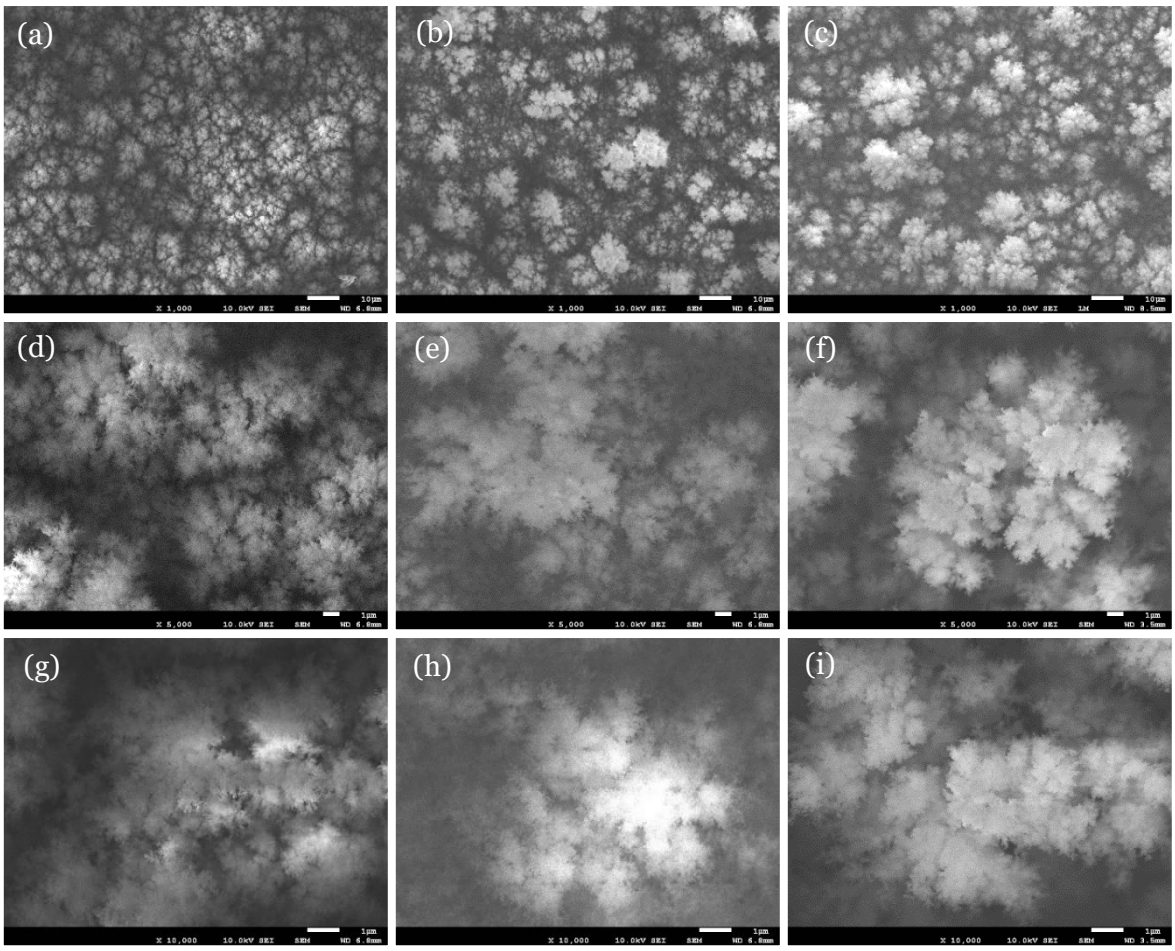

Figure 5-11. SEM images of PT5, PT5x3 and PT5x6: (a) PT5 1000x, (b) PT5x3 1000x, (c) PT5x6 1000x, (d) PT5 5000x, (e) PT5x3 5000x, (f) PT5x6 5000x, (g) PT5 10000x, (h) PT5x3 10000x and (i) PT5x6 10000x

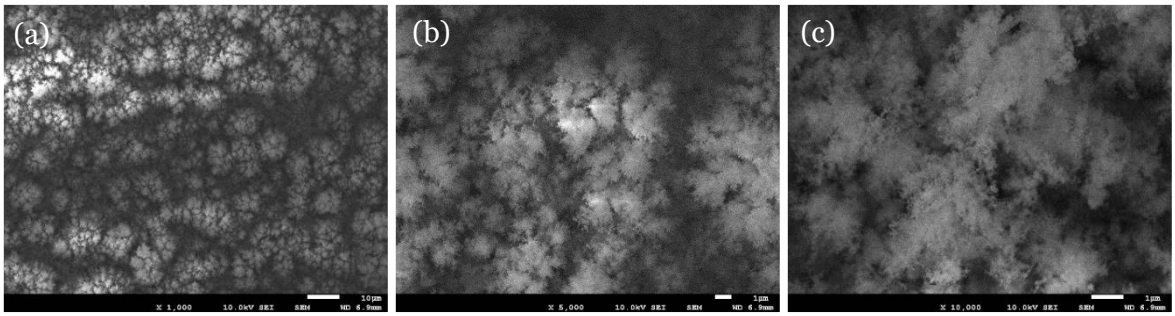

Figure 5-12. SEM images of PT5P75: (a) 1000x, (b) 5000x and (c) 10000x

5.6.2 NUMBER OF DEPOSITION PASSES

Before presenting any discussion on the chemical composition of the surface, and to reliably correlate plasma parameters with coating's chemistry, OES is used to study the

presence of various chemical functions in the plasma for two precursor flow rates (3 g/h and 5 g/h) and for up to 6 number of deposition passes. Figure 5-13 shows the optical emission spectrum for a precursor flow rate of 3 g/h for up to 3 passes of plasma deposition. It is observed that the intensity of all lines, specifically atomic Si lines observed at 250 nm and 287 nm [210], remains relatively constant with the number of deposition passes. This is in contrast with the case of higher precursor flow rates (5 g/h), presented in Figure 5-14, where there is an increase in the intensity of emission lines with the number of passes. Since no additional source of nitrogen or silicon is provided after the first pass, this increase in emission intensity can be correlated to an increase in plasma density with the number of deposition passes. This may be due to the presence of a previously deposited dielectric layer of the plasma. In the case of multiple plasma deposition passes for PT3, this dielectric layer is expected to be significantly thinner, and therefore its effect on plasma density is less noticeable. The effects of multiple deposition passes on surface chemistry will be discussed in detail in section 5.6.3.

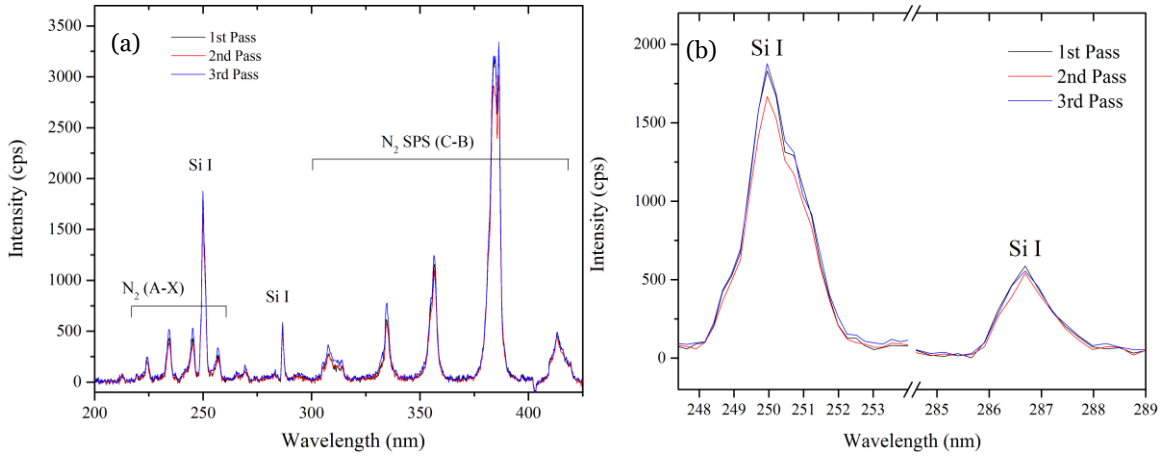

Figure 5-13. Optical emission spectra acquired from different passes with a precursor flow rate of 3 g/h: (a) full range of spectra with all peaks and features and (b) a closer look at the atomic silicon line at 250 and 287 nm.

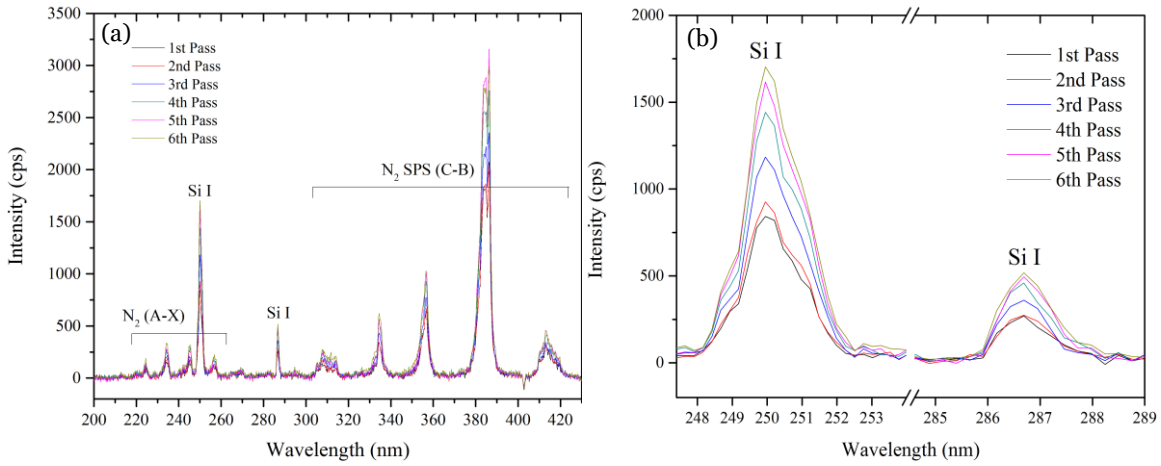

Figure 5-14. Optical emission spectra acquired from different passes with a precursor flow rate of 5 g/h: (a) full range of spectra with all peaks and features and (b) a closer look at the atomic silicon line at 250 and 287 nm.

5.6.3 CHEMICAL COMPOSITION

To achieve a comprehensive understanding on the chemical composition of the coating, different plasma parameters are isolated and their effect on the chemical composition of the coating are separately studied.

5.6.3.1 Monomer flow rate and plasma power

FTIR spectroscopy and XPS are used to study the chemical composition of different samples. Figure 5-15 shows the FTIR spectra acquired from PT3, PT5, and PT5P75.

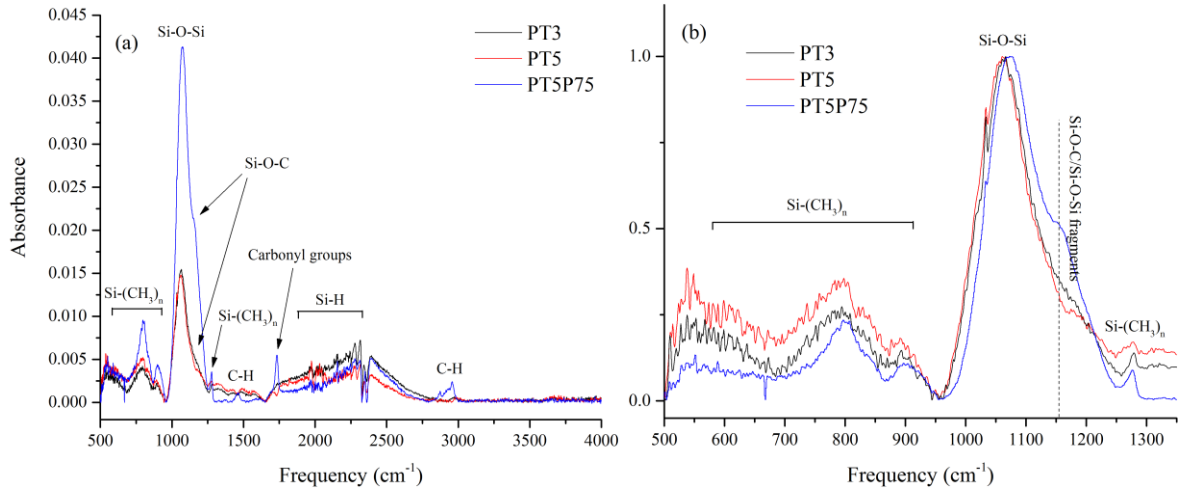

Figure 5-15. FTIR spectra acquired from PT3, PT5, and PT5P75: (a) absolute values for the full range and (b) the fingerprint region normalized according to Si-O-Si peak

In all cases, the fingerprint region of the spectrum is dominated by the features common to siloxane-based coatings. The wide band located at around 1100 cm^{-1} is assigned to Si-O-Si stretching and the peaks located at around 1275 cm^{-1} along with the peaks located between 500 cm^{-1} and 800 cm^{-1} are suggestive of Si-$(CH_3)_n$ functions [211]. The absolute intensity of these bands is significantly stronger in PT5P75, which is suggestive of a thicker coating and higher deposition rate in higher plasma powers. The presence of carbonyl groups (C=O) in PT5P75, evident by the sharp peak at around 1750 cm^{-1}, confirms higher precursor fragmentation. This increases the presence of oxygen in the plasma and subsequently increases the deposition rate.

In order to accurately compare siloxane state in these coatings, the fingerprint region of the spectra is normalized according to Si-O-Si peak and the results are presented in Figure 5-15b. Si-$(CH_3)_n$/Si-O-Si ratio for PT3 is lower than that of PT5. This is because the plasma power is identical in both cases, thus in the case of PT3 the same amount of energy is being used to induce fragmentation in a lower amount of precursor. Therefore, higher monomer fragmentation is expected in lower precursor flow rates. Si-$(CH_3)_n$/Si-O-Si ratio is even lower for PT5P75 which suggests that higher power leads to higher amount of deposited oxide, which is consistent with higher monomer fragmentation.

The intense band between 1000 cm^{-1} and 1200 cm^{-1} is of great interest because it may be used to determine the structural integrity of $SiO_xC_yH_z$. As it was mentioned before, this peak is the sum of three Gaussian components related to different bond angles. In all cases presented in Figure 5-15b, TO_2 mode is manifested as a shoulder located on the higher wave number side of TO_3 mode. This shoulder is assigned to either Si-O-C stretching modes [212] or fragments of Si-O-Si chains [209]. The intensity of this component is the highest for PT5P75, which is consistent with the effect of higher plasma energy on precursor molecules.

X-ray photoelectron spectroscopy was also used to study the atomic composition of the surface along with the chemical state of silicon in all coatings. Figure 5-16 shows the atomic percentages of Si, C and O based on the survey spectra acquired from XPS. In PT5, lower precursor fragmentation degree along with the sufficient presence of precursor molecules in the plasma leads to the highest organic content on the surface (manifested as higher C percentage and lower O percentage). From FTIR data, it was shown that the deposition rate in PT5P75 is higher than that of PT5, but the coating is less organic. This is consistent with the XPS data presented here, where PT5P75 has a higher content of silicon and oxygen and a lower content of carbon. Finally, comparing the atomic percentages of PT3 with PT5, one can conclude that the deposition is lower in PT3, leading to a lower percentage of Si and C, which subsequently increases the atomic percentage of oxygen.

High resolution spectra of Si 2p core peak were used to determine the chemical state of silicon atoms in the siloxane structure. The curve-fitting models are presented in Figure 5-17 and the results of the component quantification is presented in Figure 5-18.

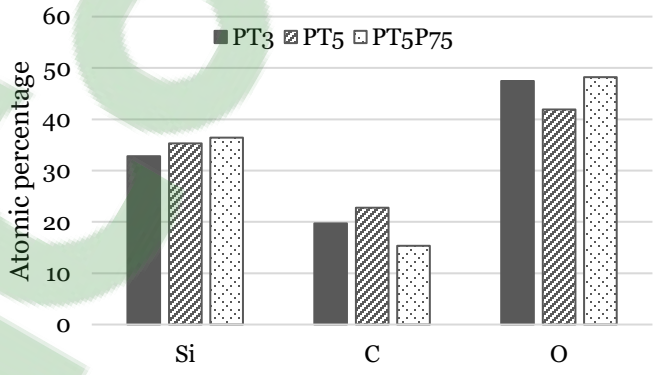

Figure 5-16. Atomic percentages of silicon, carbon and oxygen acquired from XPS for PT3, PT5, and PT5P75.

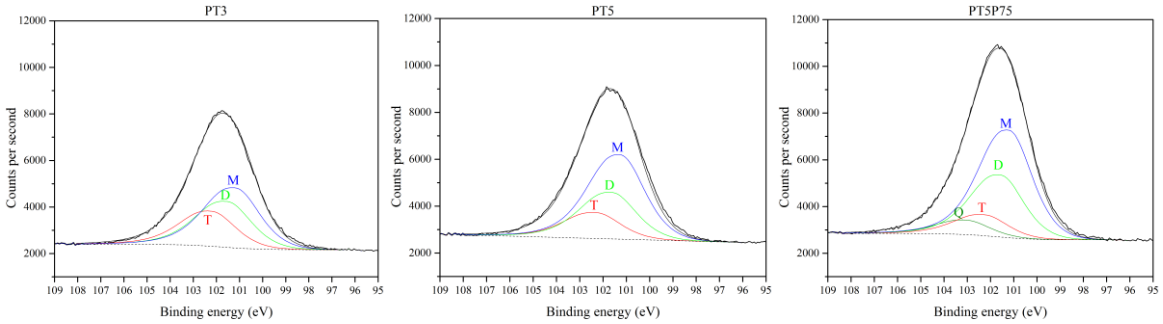

Figure 5-17. Curve-fitting models applied to the Si 2p core peak spectra acquired from high resolution scanning of PT3, PT5, and PT5P75.

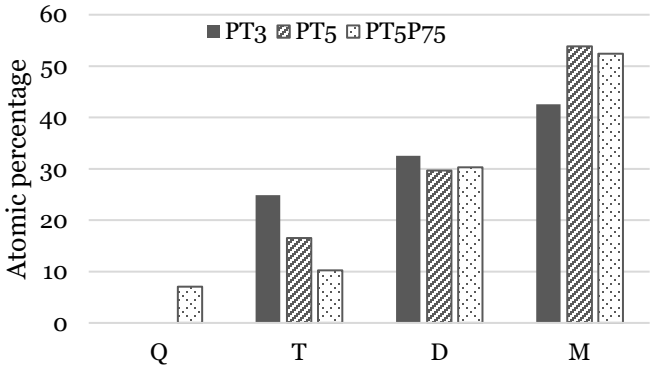

Figure 5-18. component quantification of PT3, PT5, and PT5P75 determined through high resolution spectroscopy of Si 2p core peak.

The only case where Q (silicon atom in contact with four oxygen atoms, in other words SiO_2) is observed is PT5P75. This is consistent with atomic quantification and FTIR data, where it was suggested that PT5P75 favors the formation of oxide functions due to the higher plasma energy. Comparing PT3 and PT5, an increase in the percentage of M and a decrease in the percentage of T is observed, which corresponds to a more organic coating. This is also in agreement with the FTIR and XPS data previously presented.

5.6.3.2 Number of deposition passes

The effect of number of deposition passes on surface chemistry is also studied through FTIR spectroscopy and XPS analysis. The presence of various chemical functions and radicals in the plasma during multiple passes of plasma deposition was discussed in

section 5.6.2. It was shown that in the case of PT3, the number of passes does not affect the bands intensity in OES spectra, whereas in the case of PT5, band intensities significantly increase with the number of passes. This suggests that the plasma density increases with the number of passes, which in turn affects the coating's chemical composition.

After the first pass of plasma deposition, similar to most siloxane-based coatings, the deposition consists of a silica-like structure with organic groups replacing oxygen atoms at some places. Further treatment passes can interact with the previously deposited material, breaking the Si-C bonds in the structure and removing methyl radicals from the coating [213,214] (Si-C bond energy is 76 kcal/mol while Si-O bond energy is 110 kcal/mol, thus removal of methyl groups takes priority over the destruction of silica-like structures). In fact, surface activation of poly-dimethylsiloxane (PDMS) with oxygen plasma is a well-known process used extensively in microfluids [215,216] to increase the hydrophilicity of polymer surface. The process described here is quite similar, leading to the removal of methyl radicals from the polymeric structure of the surface. These ejected radicals may be responsible for the increased plasma density reported in section 5.6.2.

The ejection of organic molecules and radicals from the surface during atmospheric pressure plasma treatment has been previously reported by Koulik et al. [217]. It has been argued that ejection can occur through one or more of the following four mechanism: (1) '*plasmochemical*' reactions, such as oxidation and etching; (2) electron bombardment; (3) UV irradiation; and (4) surface ablation. In atmospheric pressure plasmas, electron bombardment is limited due to the short electron mean free path, but plasmochemical reactions and UV radiation are intense and therefore significant material ejection may occur.

In the case of PT3, coating is less organic due to the lower presence of precursor molecules in the plasma. The lower precursor flowrate during the second and third passes, will lead to significant fragmentation of the organic groups in the coating. Some of the

possible products of such fragmentation (e.g. carbonyl groups, C-H radicals, or Si-O-C groups [213]) can be observed in the FTIR spectrum acquired from PT3x3 (Figure 5-19). Furthermore, Si-O-Si/Si-$(CH_3)_n$ ratio is lower in the coating created with only one pass, which confirms the removal and fragmentation of methyl functions during multiple passes of plasma deposition.

Figure 5-20 shows the atomic percentages of silicon, oxygen and carbon on the surface of PT3 and PT3x3. As mentioned before, XPS data are relevant to the outmost layer of the surface, and therefore the measurements presented in Figure 5-20 show the chemical composition in a thin nano-scale layer. It is observed that the coating developed with three passes of plasma deposition contains more carbon at the outmost layer. This can be due to the reorganization of organic groups (mobilized by the plasma-coating interactions) towards the surface to reach the minimum surface energy achievable.

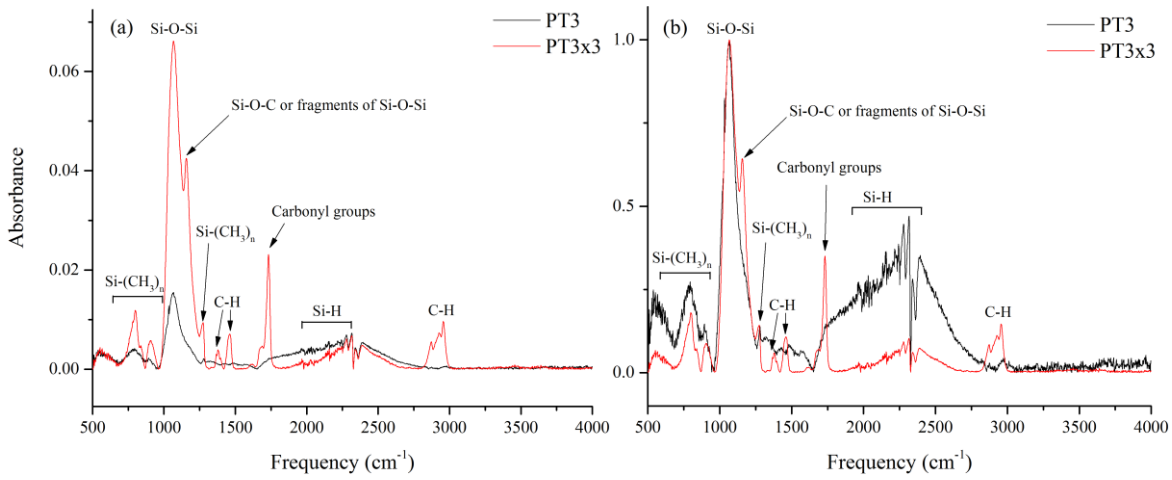

Figure 5-19. FTIR spectra acquired from PT3, and PT3x3: (a) absolute values (b) normalized values according to Si-O-Si peak

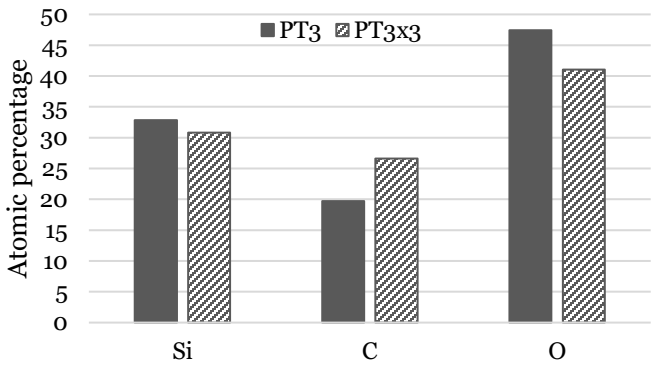

Figure 5-20. Atomic percentages of silicon, carbon and oxygen acquired from XPS for PT3 and PT3x3.

To better study the chemical state of silicon atoms in the coating structure, high resolution spectra of Si 2p core peak was acquired and curve-fitting models were developed based on the method previously discussed in section 3.8. These models are presented in Figure 5-21 and the component quantification results based on the curve-fitting models are presented in Figure 5-22. It is shown that the percentage of T groups (silicon atom in contact with three oxygen atoms) is significantly reduced and the percentage of M groups (silicon atom in contact with three methyl groups) is significantly increased. This is also consistent with methyl remobilization hypothesis presented before.

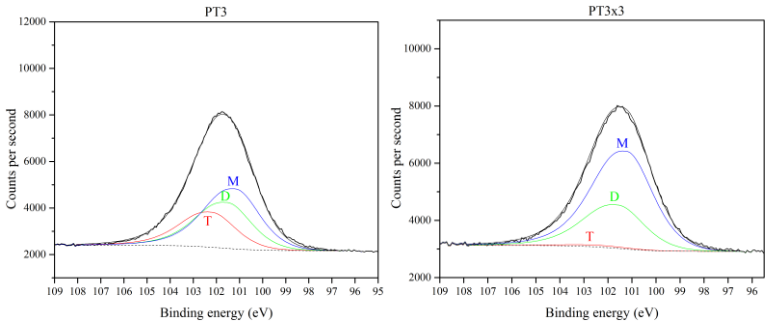

Figure 5-21. Curve-fitting models applied to the Si 2p core peak spectra acquired from high resolution scanning of PT3 and PT3x3.

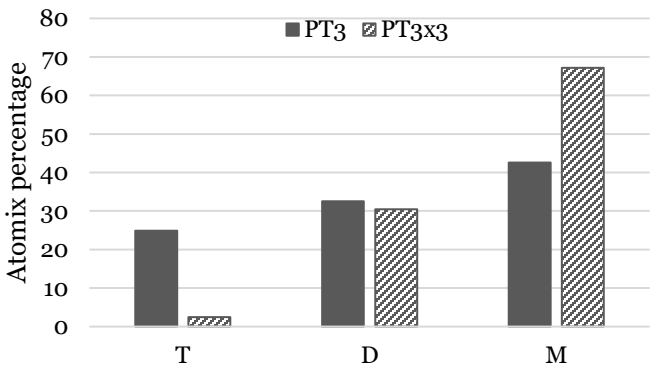

Figure 5-22. component quantification of PT3 and PT3x3 determined through high resolution spectroscopy of Si 2p core peak.

By increasing the precursor flow rate to 5 g/h, the presence of organic groups in the plasma and on the surface after the first pass is increased, leading to a decrease in precursor fragmentation compared to PT3. Figure 5-23 shows the FTIR spectra acquired from PT5, PT5x3, and PT5x6. In this case, PT5x3 and PT5x6 exhibit a stronger TO_2 shoulder, which corresponds to Si-O-Si fragments or Si-O-C functions. This is suggestive of a higher fragmentation in the case of PT5x3 and PT5x6 compared to PT5. However, unlike PT3x3, no carbonyl band is observed, implying that coating over-fragmentation is mainly avoided. The increased intensity with increasing the number of deposition passes can be attributed to the effect of thickness on band intensity.

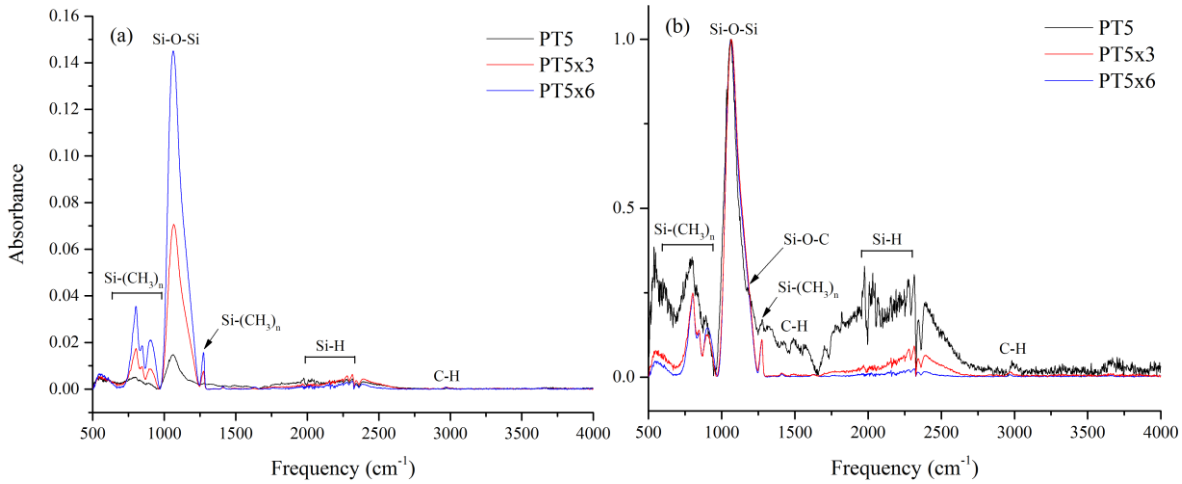

Figure 5-23. FTIR spectra acquired from PT5, PT5x3, and PT5x6: (a) absolute values (b) normalized values according to Si-O-Si peak

Figure 5-24 shows the atomic percentages of silicon, carbon and oxygen for PT5, PT5x3 and PT5x6 acquired from XPS analysis. The initial decrease in carbon atomic percentage with the number of passes can be attributed to the fragmentation of organic functions on the surface due to the interaction with plasma. Similar to the case of PT3 and PT3x3, the by-products of such fragmentation may be ejected from the surface in the form of carbon dioxide, carbon monoxide, water vapor, etc. However, there is an increase in carbon content from 3 to 6 passes which will be explained through the determination of silicon chemical state.

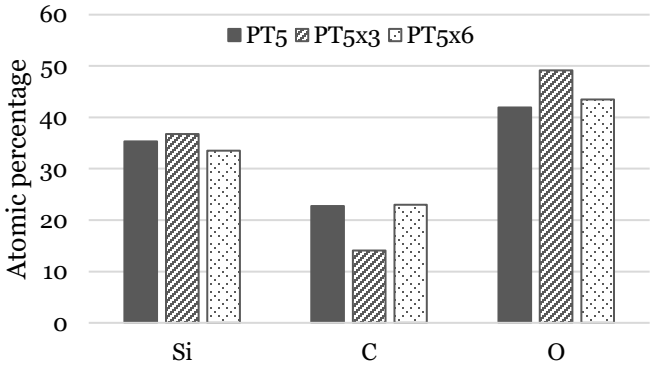

Figure 5-24. Atomic percentages of silicon, carbon and oxygen acquired from XPS for PT5, PTx3, and PT5x6.

To study the chemical state of silicon in the case of PT5, curve-fitting models on Si 2p core peak are developed for PT5, PT5x3 and PT5x6. These models are presented in Figure 5-25 and the component quantification based on them is presented in Figure 5-26. It is shown that the chemical state of silicon on the outmost layer of the coating remains the same from 1 to 3 passes of plasma deposition. This can be explained by the higher presence of precursor molecules in the plasma. In this case, a higher amount energy is required for precursor fragmentation, and thus the remobilization of organic function in the coating is less significant. However, by increasing the number of passes from 3 to 6, organic part of the deposition becomes more mobile, leading to an immigration of organic functions towards

the surface, increasing the atomic percentage of C and converting T functions in PT5x3 to M functions in PT5x6.

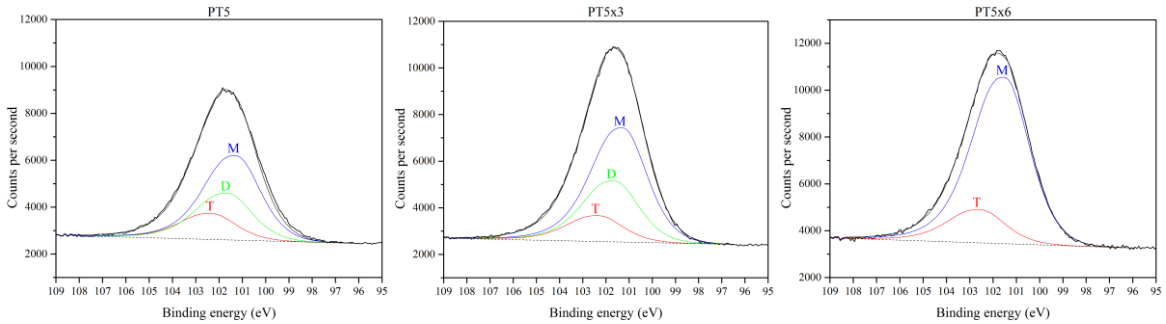

Figure 5-25. Curve-fitting models applied to the Si 2p core peak spectra acquired from high resolution scanning of PT5, PT5x3, and PT5x6.

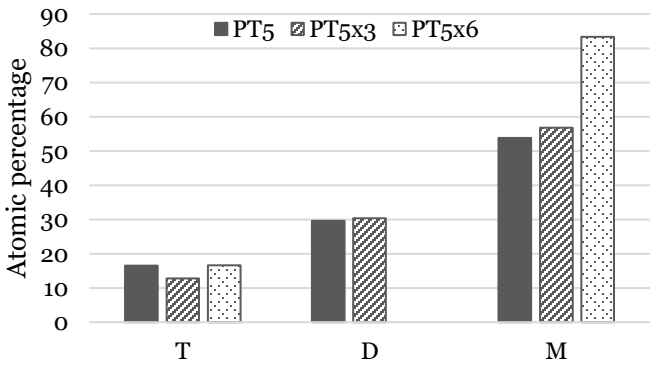

Figure 5-26. component quantification of PT5, PT5x3, and PT5x6 determined through high resolution spectroscopy of Si 2p core peak.

5.6.3.3 Consideration relevant to the curve-fitting process

At this point, it should be noted that in a typical curve fitting process, the results may be examined by developing a curve model on a different peak related to a different atom and confirming the agreement between the results acquired from both models. In this case, it may be done by developing synthetic models on C 1s peak based on (T), (D), and (M) functions along with other possible carbon states (such as C-C, C-H and C=O). However, the binding energies for C $1s^{(T)}$, C $1s^{(D)}$, and C $1s^{(M)}$ are in a 0.5 eV range (284.7 eV, 284.5 eV and 284.2 eV, respectively). Furthermore, the binding energy of adventitious carbon (carbon

originated from exposure to air or other sources of contamination) is also in the same range. Due to the relatively large FWHM of the high-resolution spectra (~ 2eV), distinguishing the peaks in such a short range is practically impossible, and therefore no confirmation was performed on the models presented in this section. However, the models presented here were developed using as many restrictions as possible (on peak position, peak width, peak shape, etc.) to ensure mathematical and chemical accuracy of component quantification. Furthermore, the results from this quantification is in complete agreement with FTIR results and the expectations based on the literature. Therefore, we feel confident that these models can accurately represent the chemical composition of the surface.

5.6.4 WETTING BEHAVIOR

Static contact angle was measured on all samples and the results are presented in Figure 5-27. All surfaces are shown to be superhydrophobic (WCA > 150°) with variations due to differences in flow rate, plasma power and number of polymerization passes. It is shown that in the case of PT3 and PT3x3, multiple polymerization passes will lead to a higher contact angle. This can be due to the abundance of organic functions and a thicker coating in the case of PT3x3. A similar trend is also observed in the case of PT5 and PT5x3. However, PT5x6 shows lower contact angle compared to PT5x3. This is due to morphological saturation of the surface, a concept which was introduced in section 5.6.1. Multiple passes of plasma deposition can have a similar effect to that of increased flow rate, thus the water contact angle on PT5x6 is lower than that of PT5x3. The same explanation is also valid for the difference in contact angle between PT7 and PT5.

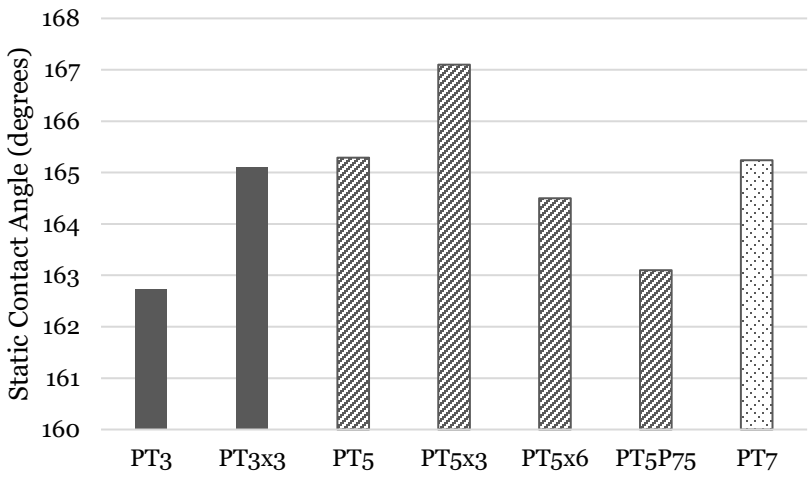

Figure 5-27. Static contact angle for PT3, PT3x3, PT5, PT5x3, PT5x6, PT5P75, and PT7.

As mentioned before, static contact angle alone is not an accurate representation of the wetting behavior on a given surface. Specifically, in icephobic applications, it has been shown that the correlation between ice adhesion and dynamic wetting parameters is stronger than that of static contact angle [6]. However, all samples discussed here show contact angle hystereses lower than 2° (not presented here), which confirms the perfect roll-off behavior observed on all coatings prior to icing. Contact angle hysteresis changes rapidly with the number of icing/deicing cycles though, a phenomenon which will be discussed in detail in section 6.2.1.

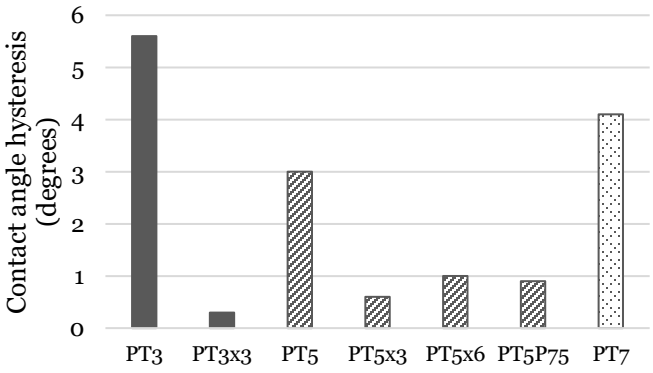

Figure 5-28. Contact angle hysteresis measured for PT3, PT3x3, PT5, PT5x3, PT5x6, PT5P75, and PT5x6.

5.6.5 DROPLET MOBILITY

As mentioned before, free rolling of water droplets on superhydrophobic surfaces is a major mechanism through which ice adhesion strength can be reduced. In order to study the droplet mobility, droplet impact on 6 coatings (PT5, PT5x3, PT5x6, PT5P75, PT3 and PT3x3) was recorded using a high-speed camera with a framerate of 5400 frames per second. To demonstrate the effect of droplet speed on the time of impact as well as its size on rebound behavior, three different droplet volumes (2, 6 and 10 µL) and three different droplet heights (10, 20 and 30 mm) were studied. Due to the massive number of files acquired from this method (~180,000 images for each case), presenting them in this report as a whole is impossible, but an example recorded from a 10 µL droplet is presented in Figure 5-29.

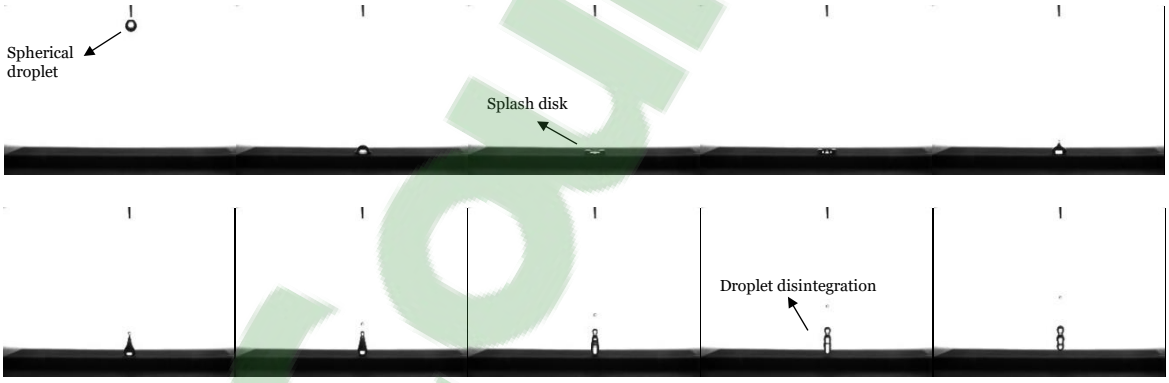

Figure 5-29. Droplet impact behavior on PT5x3 in 1.6 ms intervals. In this case, droplet volume is 10 µL and it falls towards the surface from a height of 30 mm.

Based on the number of frames in the sequence in which the droplet is in contact with the surface, the total contact time can be determined. Figure 5-30 shows the droplet contact time under different conditions for different coatings.

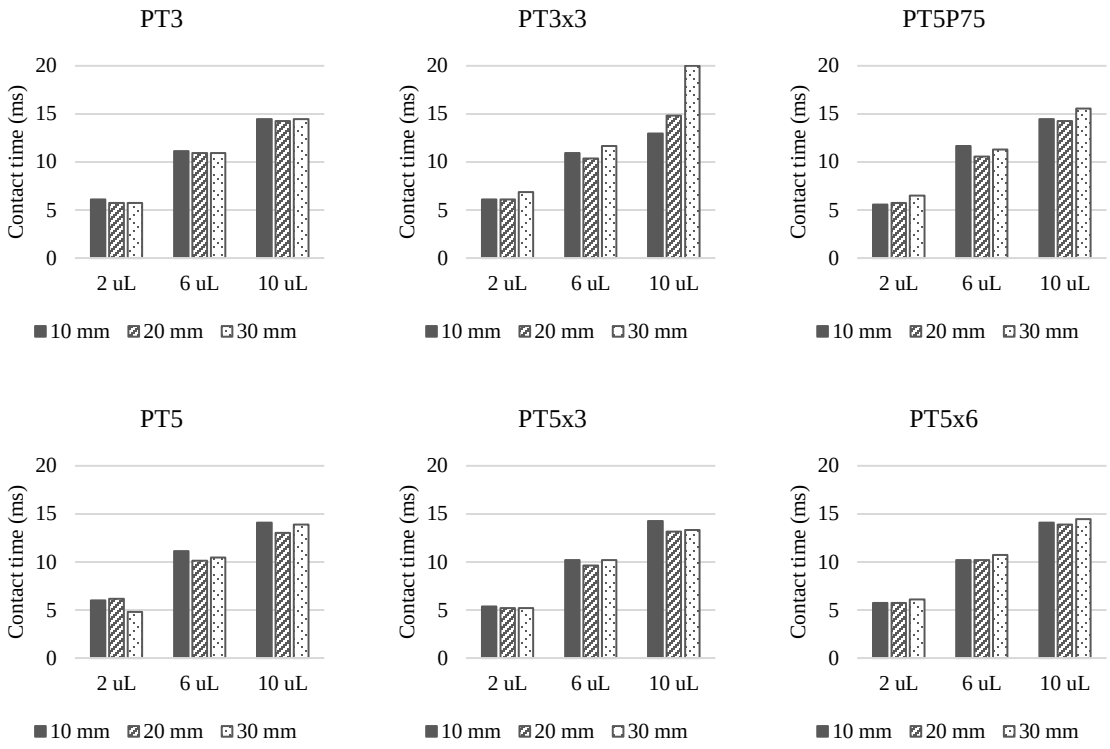

Figure 5-30. Impact time for various droplet volumes and impact heights for PT3, PT3x3, PT5P75, PT5, PT5x3 and PT5x6

In all cases, contact time increases significantly with the droplet volume. This is due to the fact that larger droplets create larger splash disks which increases the contact time. However, impact height (or impact speed) does not seem to have a noticeable effect on the impact time. Although faster droplets have a higher impact force (i.e. they are pinned to the surface with a stronger force), the repelling force from the surface is also proportionally increased, and therefore no significant effect is observed on the impact time.

PT5x3 exhibits the shortest impact time compared to all other samples studied here. This is in agreement with the ice adhesion strength measurement results, which will be discussed in the next section.

5.6.6 ICEPHOBIC CHARACTERISTICS

In this section, the results from ice adhesion strength measurement will be discussed. Adhesion strength is presented in two forms: (1) ice adhesion strength, which is the direct

value of strength (kPa) and (2) adhesion reduction factor (ARF), which is the ratio between ice adhesion strength on untreated aluminum (≈350 kPa) and ice adhesion strength on any given coating. The effect of precursor flow rate on ice adhesion strength and adhesion reduction factor is presented in Figure 5-31. It is shown that PT5 has the lowest ice adhesion strength and highest ARF during the first three cycles of icing/deicing. This is in agreement with the results obtained from morphological and chemical characterization of the samples.

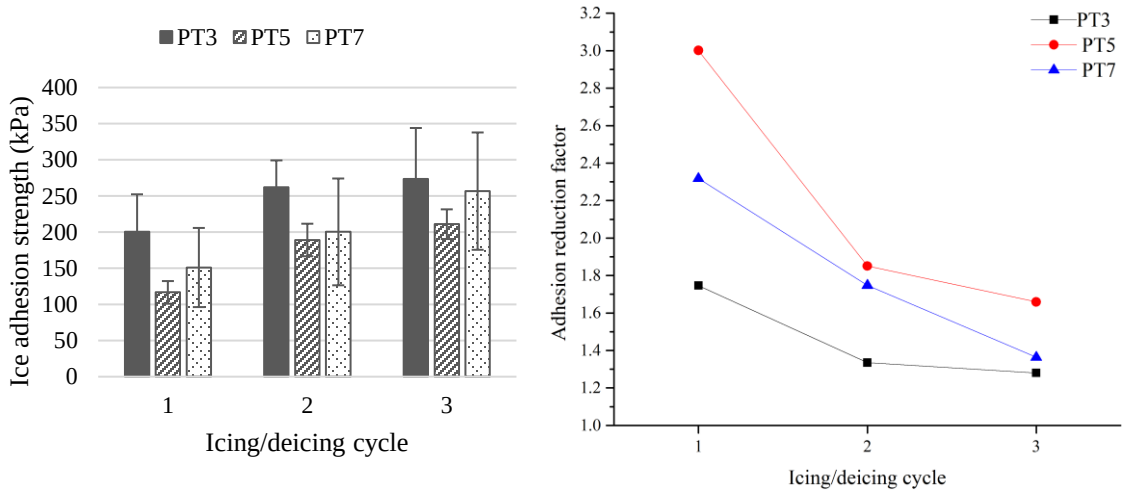

Figure 5-31. Effect of precursor flow rate on ice adhesion strength for up to three cycles of icing/deicing. Ice adhesion strength values are presented on left and adhesion reduction factor values are presented on right. Ice adhesion strength of untreated Al-6061 is around 350 kPa.

Figure 5-32 and Figure 5-33 show the effect of multiple deposition passes on ice adhesion strength for two different flow rates: 3 g/h and 5 g/h, respectively.

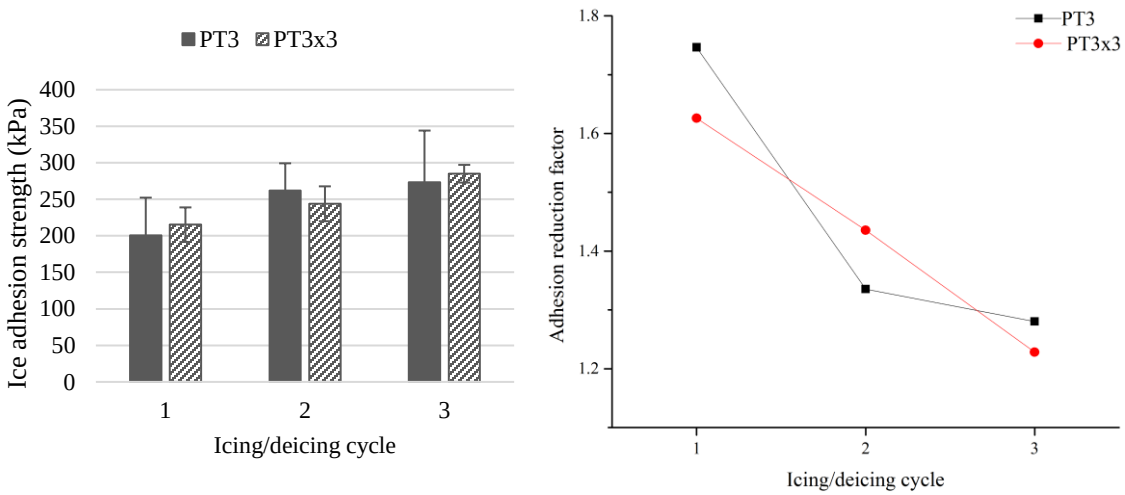

Figure 5-32. Ice adhesion strength on PT3 and PT3x3 for up to 3 cycles of icing/deicing. Ice adhesion strength values are presented on left and adhesion reduction factor values are presented on right. Ice adhesion strength of untreated Al-6061 is around 350 kPa.

For a flow rate of 3 g/h, similar ice adhesion strength is observed on the samples created with 1 and 3 passes of plasma deposition.

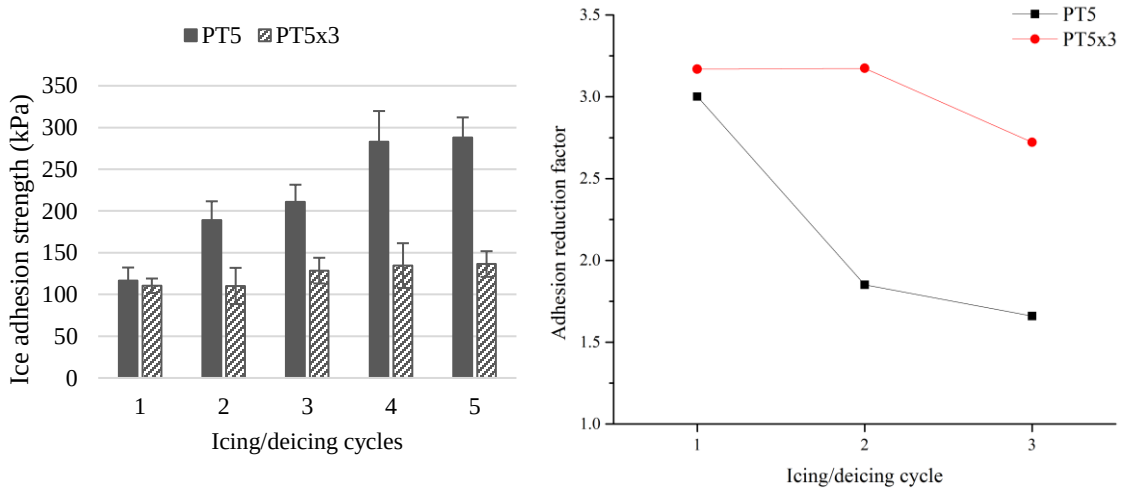

Figure 5-33. Ice adhesion strength on PT5 and PT5x3 for up to 5 cycles of icing/deicing. Ice adhesion strength values are presented on left and adhesion reduction factor values are presented on right. Ice adhesion strength of untreated Al-6061 is around 350 kPa.

In the case of PT5 and PT5x3, ice adhesion strength for the first cycle is almost equal for both samples. However, ice adhesion strength for the second cycle on PT5 increases by almost 100%, whereas this rapid increase is not observed in PT5x3. This can be explained by the removal of the coating during the aggressive deicing process in both cases. PT5x3 is

expected to be thicker than PT5, and therefore it can retain its icephobic properties after multiple icing/deicing cycles.

Figure 5-34 compares the ice adhesion strength for the first three cycles for PT5, PT5x3 and PT5x6. It is shown that increasing the number of passes from 3 to 6 has an adverse effect on ice adhesion strength. This is in agreement with chemical and morphological analysis of PT5x6, where it was argued that the additional passes would lead to the saturation of the surface asperities (surface saturation) and altering the chemical state of silicon (absence of D and abundance of M in PT5x6), which would ultimately increase the ice adhesion strength.

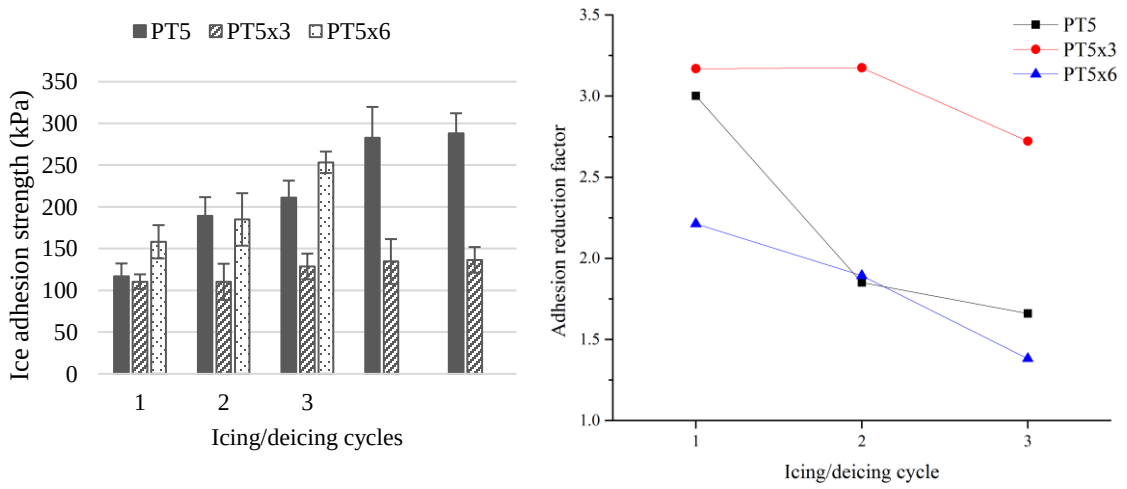

Figure 5-34. Effect of the number of passes on ice adhesion strength. Ice adhesion strength values are presented on left and adhesion reduction factor values are presented on right. Ice adhesion strength of untreated Al-6061 is around 350 kPa.

Figure 5-35 compares the ice adhesion strength for PT5 with that of PT5P75. Increasing the plasma generation power increases the monomer fragmentation degree, which in turn increases the deposition of oxide functions while increasing the coating's thickness. Therefore, PT5P75 is thicker than PT5, but the amount of organic hydrophobic species in PT5P75 is less than PT5. This places PT5P75 somewhere between PT5 and PT5x3. Ice adhesion strength measurement confirms this hypothesis.

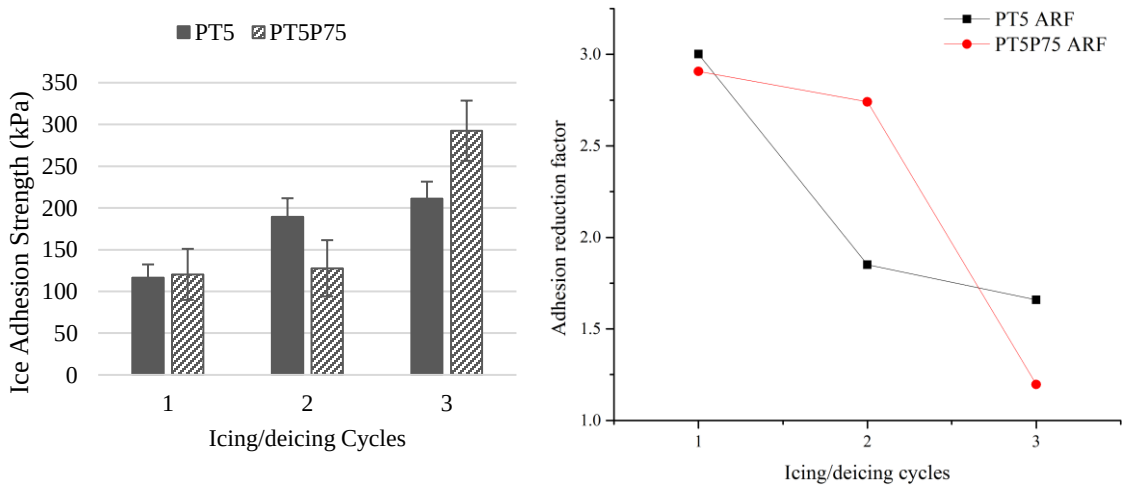

Figure 5-35. Ice adhesion strength on PT5 and PT5P75 for up to 3 cycles of icing/deicing. Ice adhesion strength of untreated Al-6061 is around 350 kPa.

Figure 5-36 shows the ice adhesion strength on PT5x3 during 10 consecutive icing/deicing cycles. The increasing trend in ice adhesion strength confirms the removal of the coating materials during deicing. It can be observed that for the first 9 icing/deicing cycles, ice adhesion strength on PT5x3 is reduced by a factor of at least two compared to the ice adhesion strength on unpolished aluminum (ARF > 2). Ice adhesion strength increases to 228 for the 10th cycle, which is more than double the ice adhesion strength for the 1st cycle.

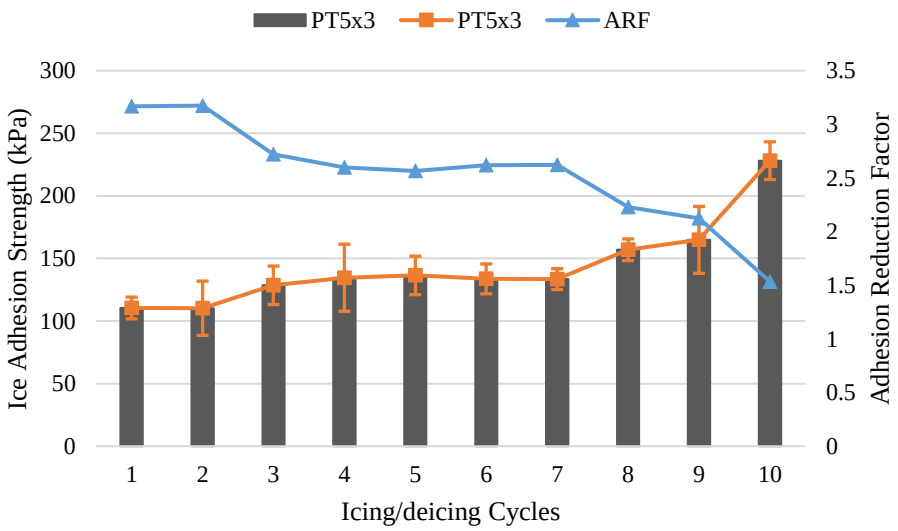

Figure 5-36. Ice adhesion strength on PT5x3 for up to 10 cycles of icing/deicing. Ice adhesion strength of untreated Al-6061 is around 350 kPa.

5.7 CONCLUSION

In this chapter, the details regarding the plasma deposition process in the presence of HMDSO using nitrogen plasma was discussed. It was shown that compared to air plasma deposition, nitrogen plasma can create more organic coatings with smaller surface features. Therefore, nitrogen was identified as the preferable choice for ionization gas. Furthermore, the effects of precursor flow rate on surface structure, wetting behavior and surface chemistry was studied. It was argued that by gradually increasing the precursor flow rate, smaller spherical nano-particles on the surface may agglomerate, forming larger irregular particles with multiple levels of roughness, which is suitable for hydrophobic applications. However, increasing the flow rate above a threshold leads to the formation of a white powder on the surface, which can decrease the mechanical stability of the coating. It was concluded that to retain the hierarchical structure while preventing powder formation, a small modification to the jet is necessary. In order to reduce oxygen diffusion from ambient air into the treatment region, a quartz tube was mounted on the jet head using a simple copper clamp to confine the plasma jet and allow the ignition and maintenance of weak plasmas.

Using this quartz tube, multiple samples were created with different plasma parameters and the effects of these parameters on surface morphology, chemical composition, wetting behavior and icephobic characteristics was studied. It was shown that the sample created with three passes of plasma deposition using minimum power under a precursor flow rate of 5 g/h exhibits the best properties (highest static contact angle, lowest contact angle hysteresis and lowest ice adhesion strength) among all coatings studied here. The effects of various environmental factors on surface properties will be discussed in the next chapter.

CHAPTER 6

SURFACE STABILITY AGAINST ENVIRONMENTAL FACTORS

6.1 INTRODUCTION

In this chapter, the effects of various environmental factors, such as icing/deicing cycles, UV exposure, and water immersion, will be studied on surface properties of the plasma-deposited coatings. Currently, most of the studies on icephobic surfaces report ice adhesion strength or some other icing-related parameters as a representation of surface efficiency in icing applications. However, in order to reliably estimate the effectiveness of an icephobic coating in practical conditions, coating's integrity against natural factors should be studied.

6.2 EFFECTS OF ICING/DEICING ON SURFACE PROPERTIES

6.2.1 WETTING BEHAVIOR

The wetting behavior of all samples is studied through static and dynamic contact angle measurements after each icing/deicing cycle. It should be noted that in Figure 6-1 to Figure 6-4, error bars (maximum of ±5° and thus not statistically significant) are intentionally removed from the graphs to improve the clarity. Figure 6-1 shows the variations of static contact angle and contact angle hysteresis with the number of

icing/deicing cycles for PT3, PT5 and PT7. Although all samples exhibit a reduction in static contact angle after each icing cycle, they retain their superhydrophobic behavior even after three icing/deicing cycles. Among the three samples presented in Figure 6-1, PT5 shows the best stability against icing/deicing cycles. This can be due to the fact that PT5 has the most efficient combination of roughness and chemistry, and therefore the contact area between the water and the surface is minimized. This results in the surface being less affected by the ice removal.

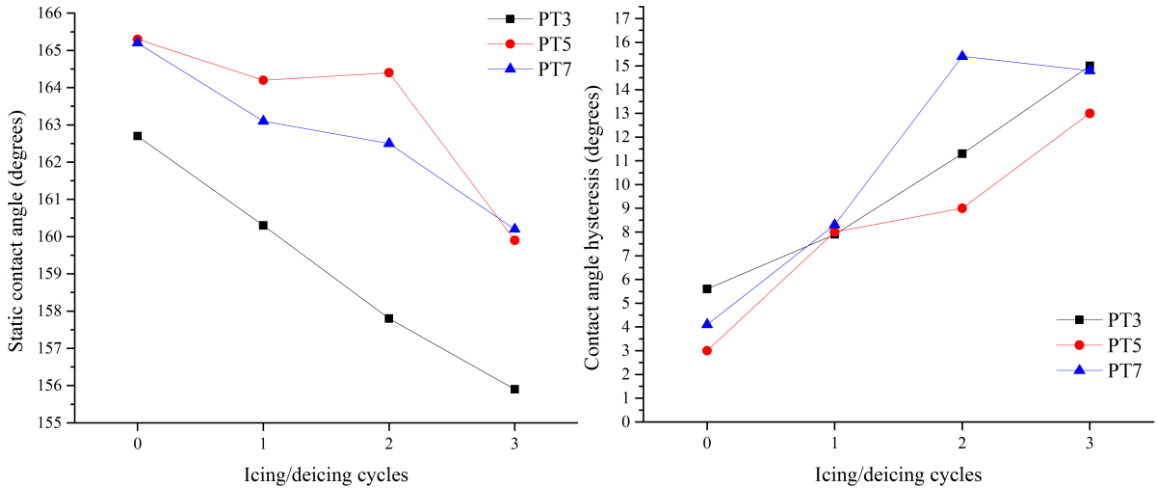

Figure 6-1. Static (left) and dynamic (right) contact angle measurements for PT3, PT5, and PT7 for up to 3 cycles of icing/deicing.

Figure 6-2 shows the static and dynamic contact angle values for PT3 and PT3x3. In both cases, static contact angle decreases while contact angle hysteresis increases with the number of icing/deicing cycles. Although the static contact angle for PT3 remains lower than that of PT3x3, and hysteresis for PT3 remains higher than that of PT3x3, there is no noticeable difference in the increasing/decreasing trend between the two coatings. This suggests that both coatings are affected by deicing to the same degree, and despite minor morphological and chemical differences, the mechanical stability of both coatings are similar.

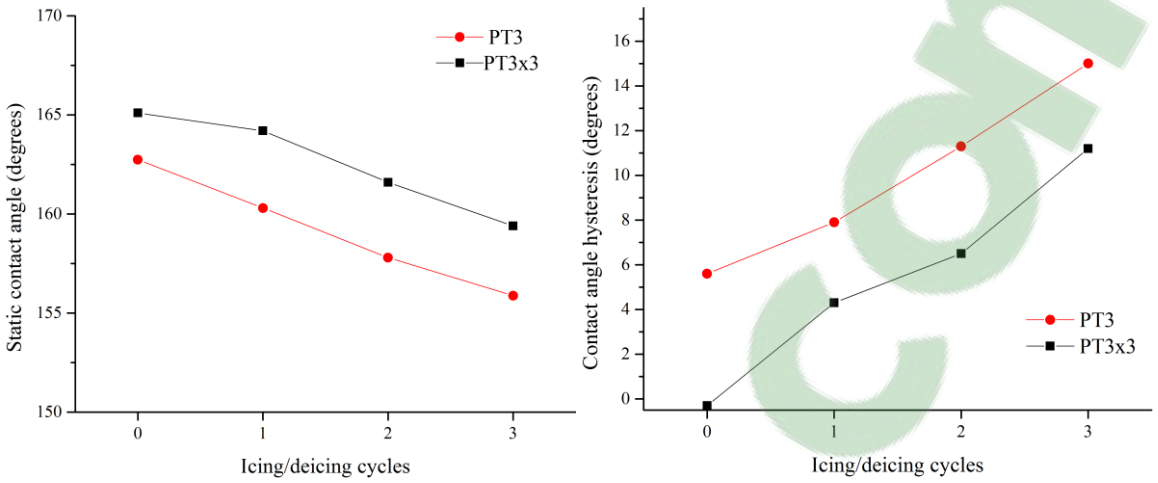

Figure 6-2. Static (left) and dynamic (right) contact angle measurements for PT3 and PT3x3 for up to 3 cycles of icing/deicing.

Figure 6-3 compares the effect of 3 icing/deicing cycles on contact angle and contact angle hysteresis for PT5, PT5x3 and PT5x6. For PT5x6, there are no significant increase/decrease in contact angle and contact angle hysteresis with the number of icing/deicing cycles. This can be due to the fact that PT5x6 is expected to be thicker than PT5 and PT5x3, and therefore it can maintain its hydrophobicity even after significant coating removal. However, in the case of PT5x6, 3 icing/deicing cycles have a more pronounced effect on the micro/nano features of the surface structure compared to PT5x3. This can explain the higher increase in ice adhesion strength in the case of PT5x6. Icing/deicing have an almost identical effect on the static contact angle for PT5 and PT5x3. Coating removal leads to a steady decrease in static contact angle. However, PT5x3 exhibits a slightly higher initial static contact angle which can be explained by higher coverage of the surface and thicker coating.

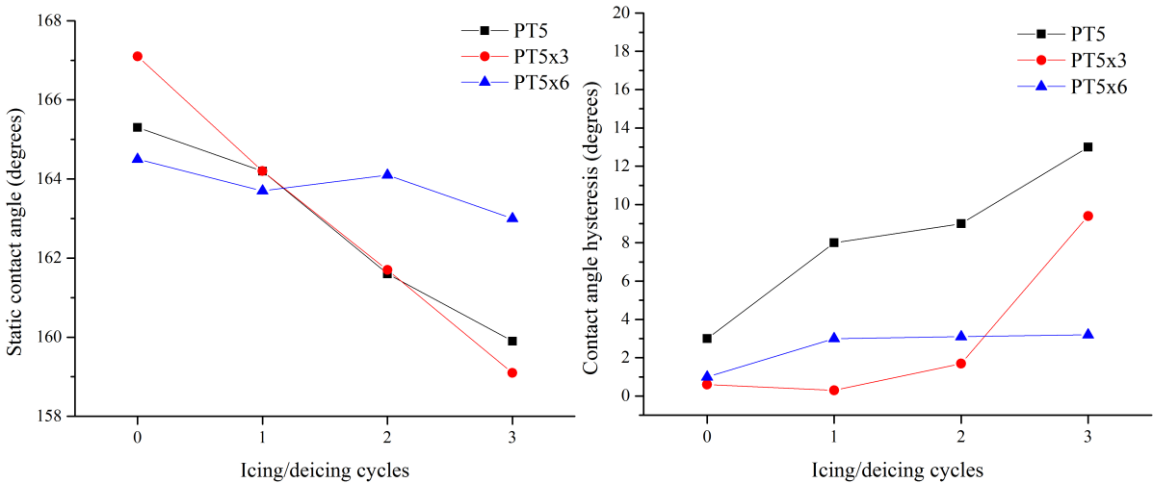

Figure 6-3. Static (left) and dynamic (right) contact angle measurements for PT5, PT5x3 and PT5x6 for up to 3 cycles of icing/deicing.

For PT5 and PT5x3, contact angle hysteresis increases with the number of icing/deicing cycles. For the first two cycles, PT5x3 exhibits lower hysteresis compared to PT5x6, which can be explained by the fact that the surface features and deposited particles are larger in the case of PT5x6. It has been shown [218] that smaller surface geometries can lead to wetting regimes closer to Cassie-Baxter which will in turn results in lower contact angle hysteresis. However, after the second icing/deicing cycle, PT5x3 may lose a portion of these smaller features, while the larger agglomerates in PT5x6 remain on the surface.

Figure 6-4 shows the effect of plasma power on the wetting behavior of the coatings. In both cases, static contact angle decreases while contact angle hysteresis increases with the number of icing/deicing cycles.

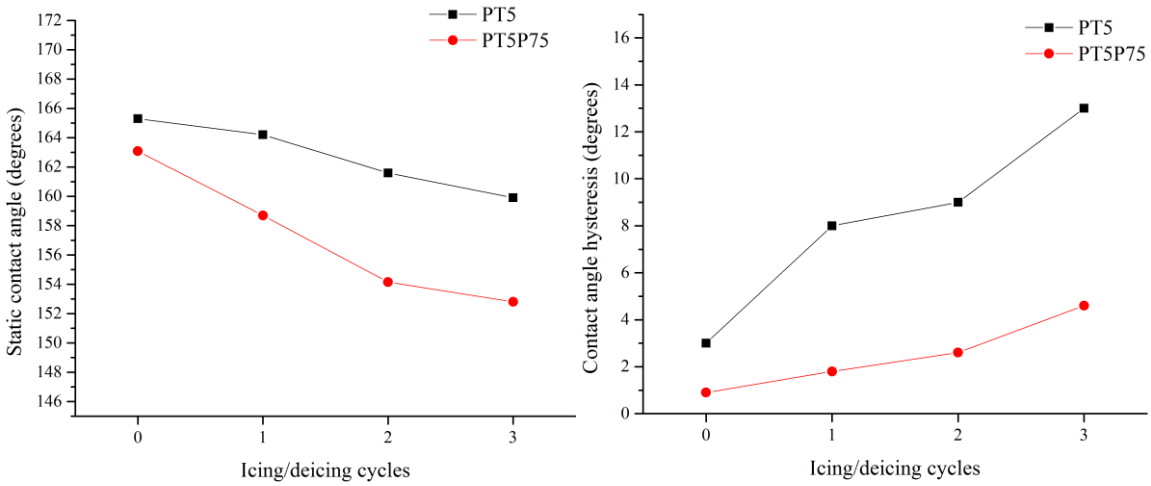

Figure 6-4. Static (left) and dynamic (right) contact angle measurements for PT5 and PT5P75 for up to 3 cycles of icing/deicing.

Figure 6-5 shows the variation of static contact angle with the number of icing/deicing cycles for PT5x3. Although there is a steady decrease in static contact angle, PT5x3 can maintain its superhydrophobic behavior for up to at least 7 cycles of icing/deicing.

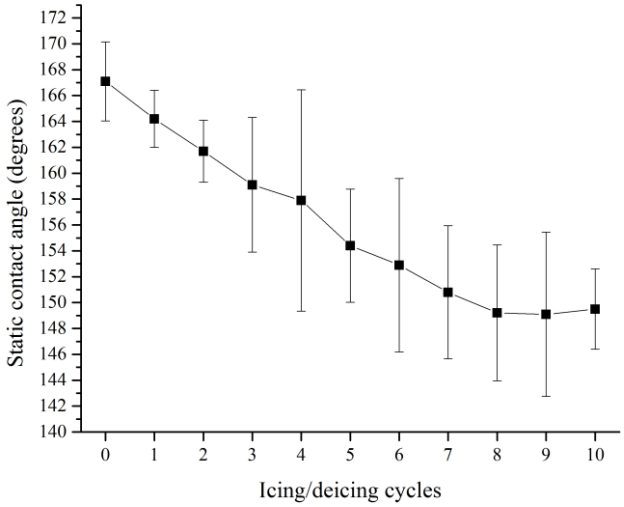

Figure 6-5. Static contact angle values for PT5x3 for up to 10 cycles of icing/deicing.

Dynamic wetting behavior was also studied extensively for PT5x3 and the results are presented in Figure 6-6. The decrease in advancing contact angle with icing/deicing cycles

is not as significant as that of the receding contact angle. There is a sharp drop in the receding angle after the first three icing deicing cycles, which leads to a rapid increase in contact angle hysteresis. It has been suggested that ice adhesion strength correlates to $1 + \cos\theta_{rec}$ (see Equation 2-4) [69,218]. This is in agreement with the results presented here, since the ice adhesion strength remains relatively constant for the 4th, 5th, 6th, and 7th icing/deicing cycles, which is the range where receding contact angle is constant. The drop in contact angle hysteresis after the 5th cycle is due to the decreasing advancing angle while the receding angle remains relatively constant.

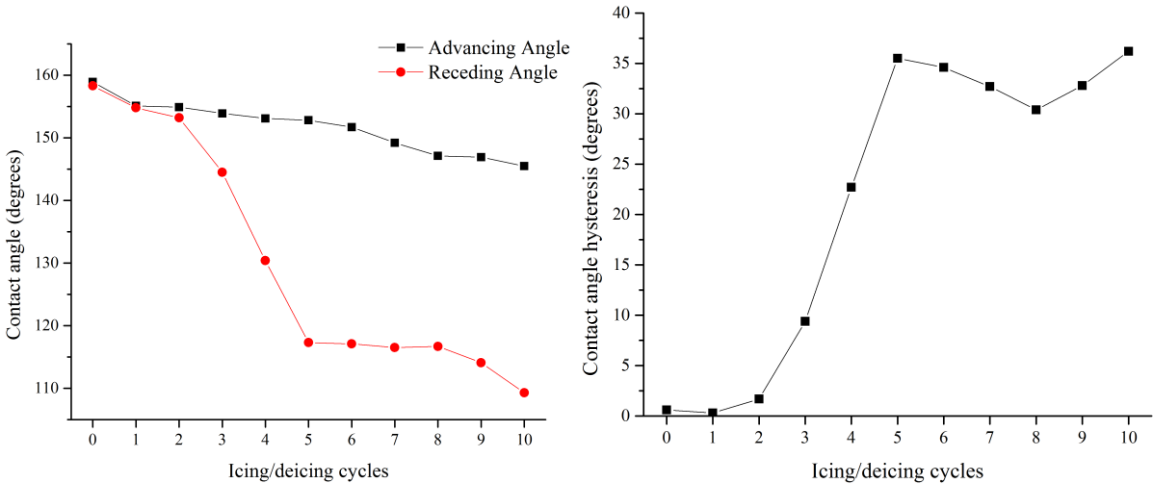

Figure 6-6. Advancing and receding angles (left) and contact angle hysteresis for PT5x3 for up to 10 cycles of icing/deicing.

Figure 6-7 shows the correlation between $1 + \cos\theta_{rec}$ and ice adhesion strength values for up to 10 icing/deicing cycles for PT5x3. Although this correlation is reported to be linear in the literature, Pearson's coefficient value for the regression line is rather unsatisfactory (r = 0.67943, where r = 1 indicates a full linear correlation and r = 0 indicates a non-linear correlation). There is a better linear fit (dashed red line) for the first 5 data points (r=0.8495), which may be suggestive of a more linear regime at lower ice adhesion strengths, followed by a constant ice adhesion strength regime and a constant work of adhesion regime (dashed grey lines). At this point, these 'regimes' are only reported as an

observation since more data points are required in order to reliably distinguish and explain this behavior.

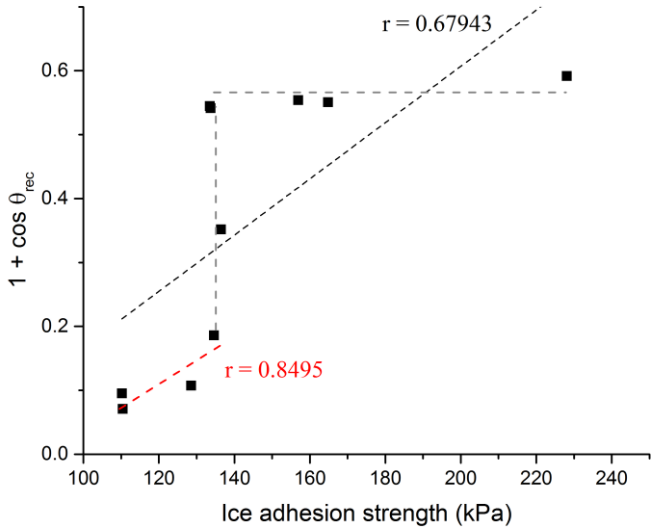

Figure 6-7. Ice adhesion strength values for PT5x3 graphed against 1+cos θ_{rec}.

6.2.2 CHEMICAL COMPOSITION

Table 6-1 shows the results acquired from atomic quantification of all samples through XPS. For the sake of clarity, these values will also be presented in several graphs in this section.

Table 6-1. Atomic percentage of silicon, carbon and oxygen on all samples before and after multiple icing/deicing cycles.

	Si	C	O
PT3 Before	32.8	19.7	47.5
PT3 After	29.3	26.1	40.7
PT3x3 Before	30.8	26.6	41.1
PT3x3 After	26.9	36.4	35.1
PT5 Before	35.3	22.8	41.9
PT5 After	29.3	26.1	40.7
PT5P75 Before	36.4	15.4	48.2
PT5P75 After	34.9	17.8	47.3
PT5x3 Before	36.8	14.1	49.1
PT5x3 After	32.3	26.4	41.3
PT5x6 Before	33.5	23.0	43.5
PT5x6 After	29.5	35.9	34.6
PT7 Before	31.5	23.1	45.5
PT7 After	19.6	41.5	33.9

Figure 6-8 shows the effects of 3 icing/deicing cycles on the chemical composition of PT3, PT5, and PT7. In all cases, the atomic percentages of silicon and oxygen decrease while the atomic percentage of carbon increases with the number of icing/deicing cycles. The decrease in the percentage of silicon and oxygen can be attributed to the coating removal from the surface due to deicing. Subsequently, carbon atomic percentage will increase

regardless of the carbon content. However, surface contamination during icing/deicing cycles may be at least partially responsible for this increase in carbon percentage.

It is shown that the decrease in silicon and oxygen atomic percentages in the case of PT5 is not as significant as that in the case of PT3 or PT7. This suggests that compared to PT3 and PT7, PT5 is more capable of maintaining its surface structure after deicing.

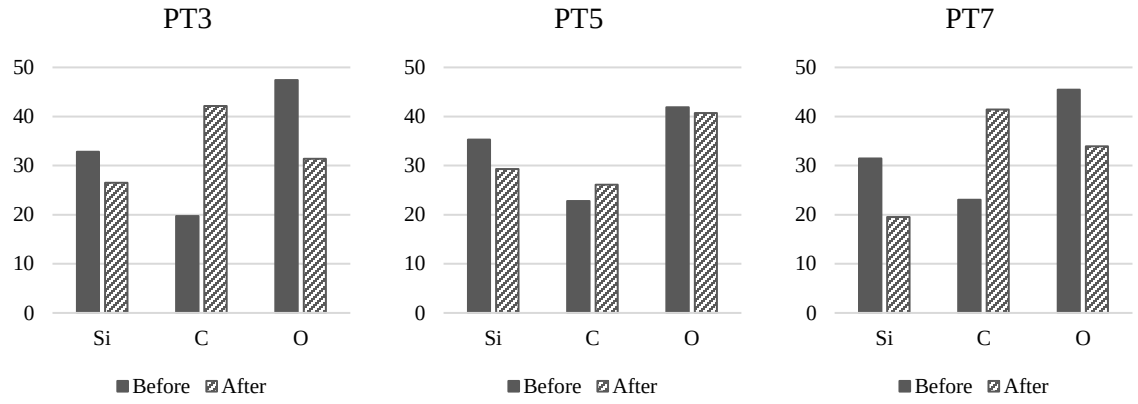

Figure 6-8. Chemical composition of the coating for PT3, PT5 and PT7 before and after 3 icing/deicing cycles.

Figure 6-9 shows the coating's chemical composition before and after 3 cycles of icing/deicing for PT3 and PT3x3. Similar to the previous cases, silicon and oxygen atomic percentage decreases while carbon atomic percentage increases after 3 cycles of icing/deicing. However, it can be seen that the decrease in oxygen and silicon content in the case of PT3 is significantly stronger compared to PT3x3. This suggests that PT3x3 exhibits higher stability against icing/deicing cycles, leading to a lower coating removal which manifests itself in a lower reduction in silicon and oxygen content.

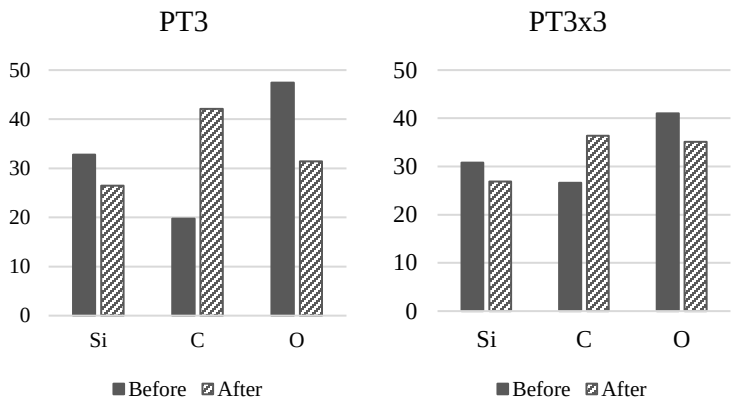

Figure 6-9. Chemical composition of the coating for PT3 and PT3x3 before and after 3 icing/deicing cycles.

Figure 6-10 shows the effect of multiple icing/deicing cycles on the chemical composition of PT5, PT5x3 and PT5x6. It should be noted that for PT5x3, chemical composition is acquired after 10 cycles of icing/deicing, while for the other two cases presented in Figure 6-10, chemical composition is acquired after 3 cycles of icing/deicing. It is shown that in all cases, silicon and oxygen atomic percentage decrease with the number of icing/deicing cycles, which can be attributed to the removal of coating material from the surface after each deicing step. However, comparing the extent of this reduction in different cases can provide valuable information regarding coating's stability. It is shown that the reduction of oxygen and silicon content in PT5x6 is slightly higher than that of PT5. This can be explained by the absence of D units in PT5x6 (Figure 5-26), which may lead to lower stability against icing/deicing cycles. Furthermore, atomic percentage of silicon in PT5x3 after 10 icing/deicing cycles is slightly higher than the atomic percentage of silicon in PT5 and PT5x6 after 3 icing/deicing cycles. This may suggest that coating removal after 10 cycles of icing/deicing in the case of PT5x3 is comparable to the coating removal after 3 cycles of icing/deicing in the case of PT5 and PT5x6.

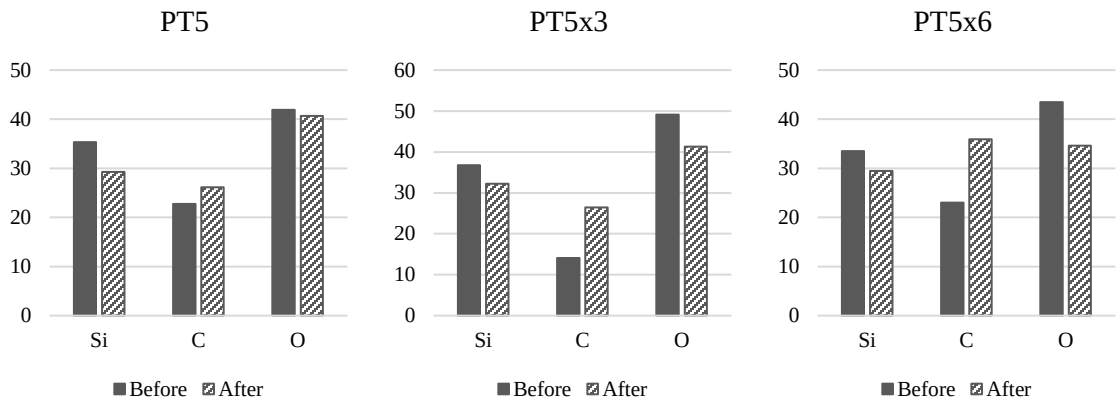

Figure 6-10. Chemical composition of the coating for PT5, PT5x3 and PT5x6 before and after 3 icing/deicing cycles (PT5 and PT5x6) and 10 icing/deicing cycles (PT5x3).

Figure 6-11 shows the effects of 3 icing/deicing cycles on the chemical composition of PT5 and PT5P75. In this case, the variations in the atomic percentage of Si, O, and C due to icing/deicing cycles are very similar. Therefore, one may conclude that PT5 and PT5P75 exhibit similar stability against icing/deicing cycles.

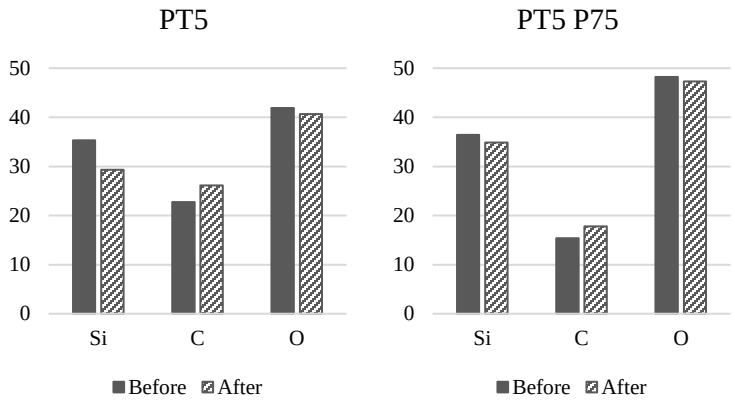

Figure 6-11. Chemical composition of the coating for PT5 and PT5P75 before and after 3 icing/deicing cycles.

Silicon chemical states were also studied before and after icing and the results are presented in Figure 6-12 and Table 6-2. It is shown that the change in the silicon chemical state due to deicing is negligible.

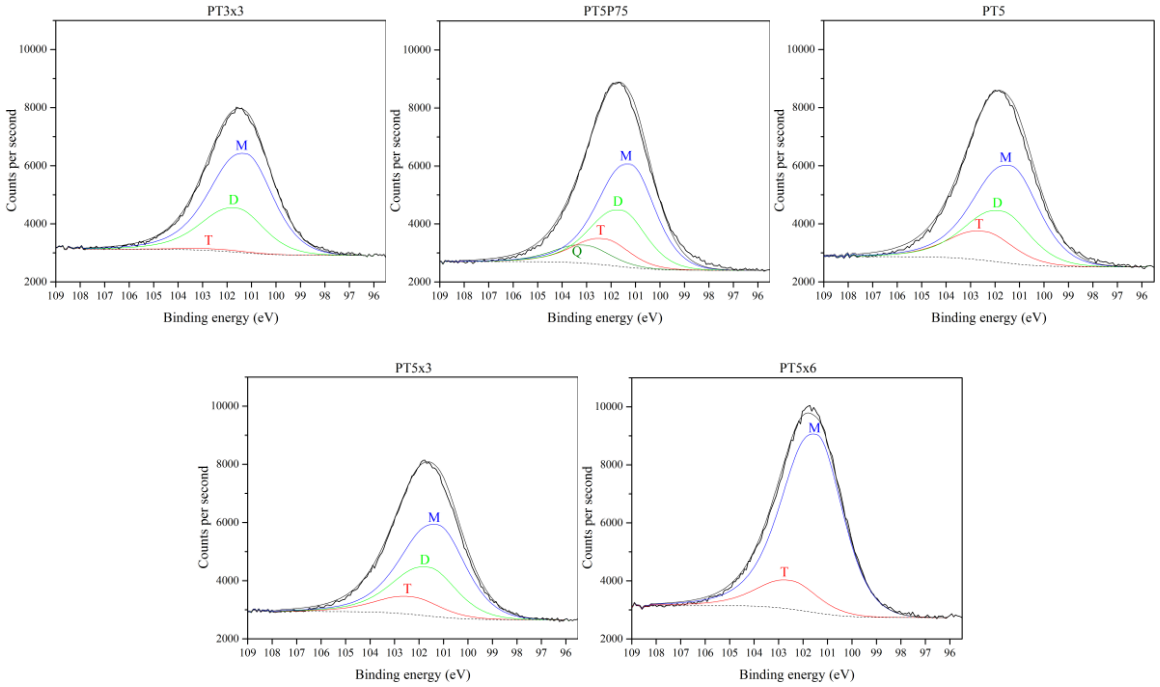

Figure 6-12. High resolution Si 2p core peak spectra acquired from PT3x3, PT5, PT5P75, PT5x3, and PT5x6 after 3 icing/deicing cycles (for PT3x3, PT5P75 and PT5x6), 5 icing/deicing cycles (for PT5) and 10 icing/deicing cycles (PT5x3).

Table 6-2. Various chemical states of silicon for different coatings before and after icing/deicing.

	Before icing				After icing			
	Q	T	D	M	Q	T	D	M
PT3x3	0	2.4	30.4	67.2	0	1.2	30.4	68.4
PT5	0	16.5	29.7	53.8	0	16.2	28.8	54.9
PT5P75	7.1	10.2	30.3	52.4	8.8	12.8	27.7	50.7
PT5x3	0	12.8	30.4	56.8	0	11.1	30.8	58.1
PT5x6	0	16.6	0	83.4	0	13.8	0	86.2

6.2.3 SURFACE MORPHOLOGY

Repeated icing/deicing cycles can affect the surface morphology by removing the coating and thus reducing the surface roughness. In this section, SEM images of various coatings before and after icing/deicing cycles is presented. It should be noted that the images

presented in Figure 6-13 are acquired with a different microscope, and therefore the appearance of the surface structure may seem different from the other images presented in this section.

Figure 6-13 shows the coating removal after 3 cycles of icing/deicing for PT3, PT5 and PT7. Despite the apparent removal of coating material from the surface, all samples retain some level of nano-roughness after 3 icing/deicing cycles.

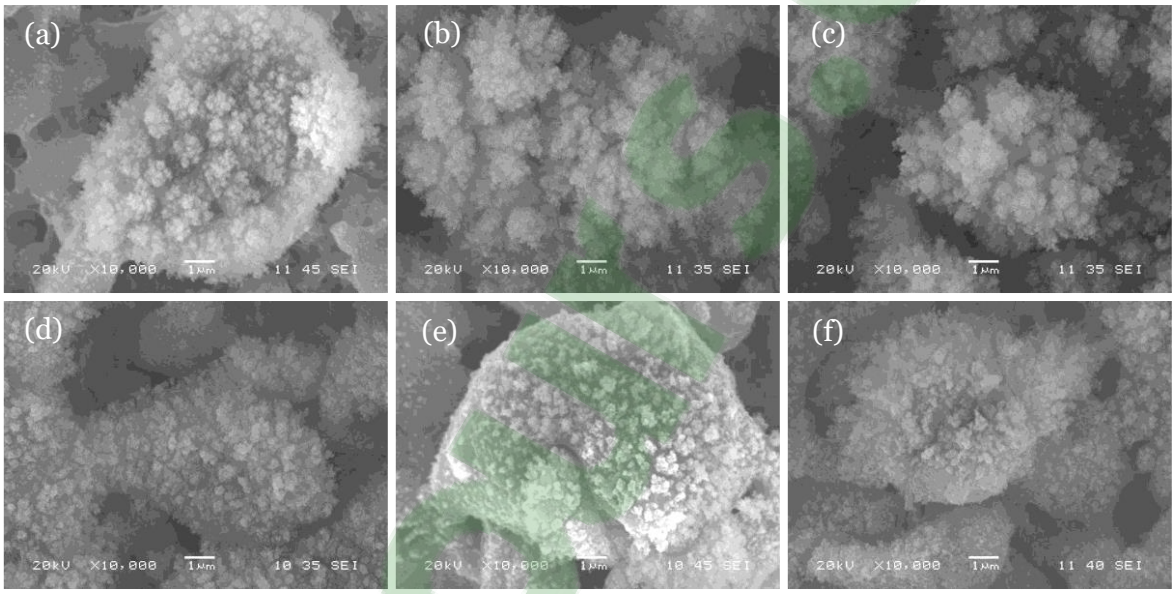

Figure 6-13. SEM images of PT3 (a and d), PT5 (b and e), and PT7 (c and f) before and after 3 icing/deicing cycles.

Figure 6-14 shows the SEM images acquired from PT3x3 before icing and after 3 icing/deicing cycles. It is clear that a noticeable amount of deposited materials is removed and most of the dendritic structures on the coating is lost after 3 cycles of icing/deicing. This is in agreement with the loss of silicon suggesting coating removal, and can be responsible for the increased ice adhesion strength after each deicing step.

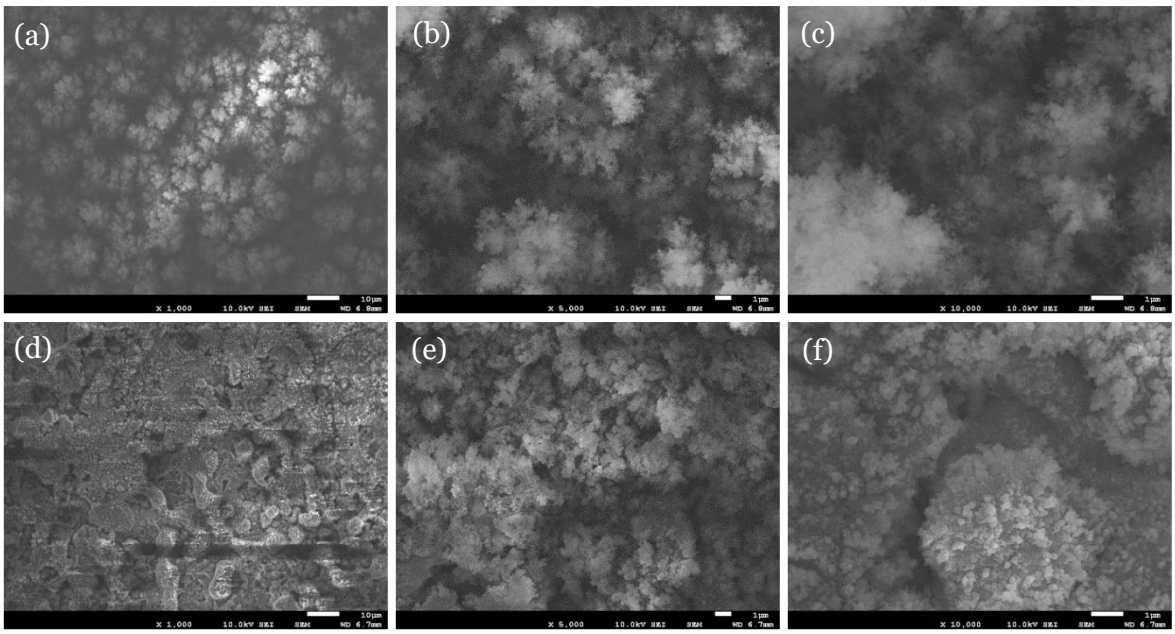

Figure 6-14. SEM images of PT3x3 before and after 3 cycles of icing deicing: (a) before icing 1000x, (b) before icing (5000x), (c) before icing 10000x, (d) after icing 1000x, (e) after icing 5000x, (f) after icing (1000x)

Since PT5 is the basis for the most efficient coating developed in this research, a more detailed set of images from before and after 5 cycles of icing/deicing on PT5 is presented in Figure 6-15. It is shown that multiple icing/deicing cycles can lead to a significant coating removal from the surface, exposing the underlying porous structure and ultimately increasing the ice adhesion strength.

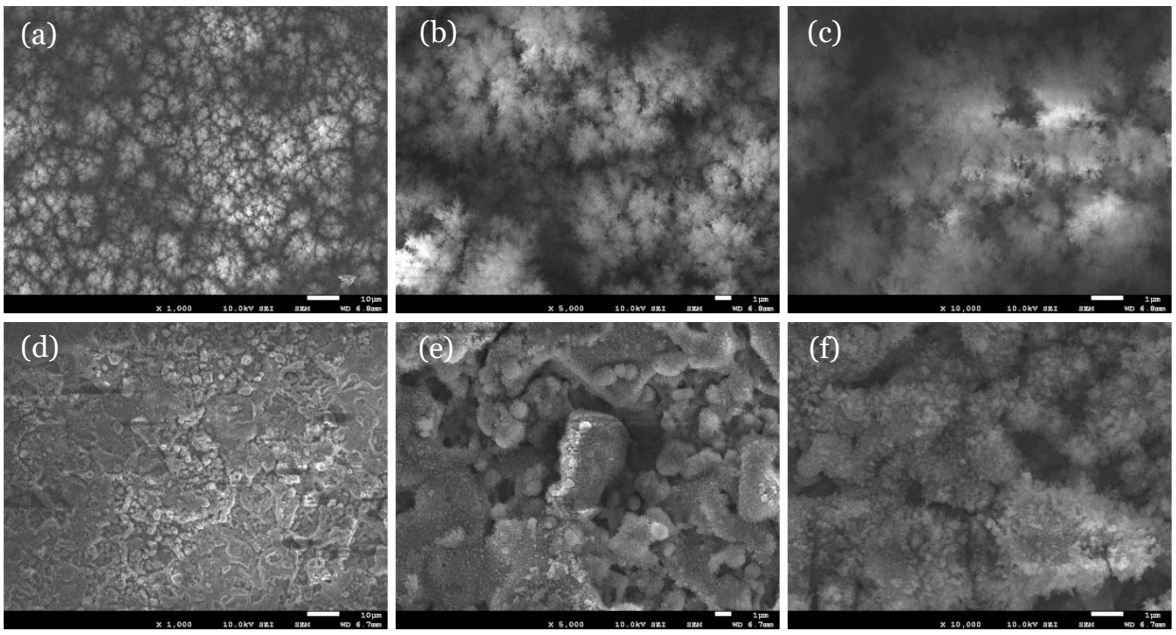

Figure 6-15. SEM images of PT5 before and after 5 cycles of icing deicing: (a) before icing 1000x, (b) before icing (5000x), (c) before icing 10000x, (d) after icing 1000x, (e) after icing 5000x, (f) after icing (1000x)

Figure 6-16 shows the SEM images acquired from PT5x3 before icing and after 10 icing/deicing cycles. Coating removal due to deicing is also observed in the case of PT5x3, but it should be noted that the images presented here are acquired from the samples after 10 cycles of icing/deicing (as opposed to 3 cycles, which is the case for all other coatings in this study except for PT5 and PT5x3). Even after 10 icing/deicing cycles, Figure 6-16(e) suggests that the dendrite-like structure is partially maintained on the surface. Since this structure plays a very important role in reducing the ice adhesion strength, this observation is in agreement with the fact that PT5x3 exhibits the smallest increase in ice adhesion strength due to icing/deicing cycles.

Figure 6-17 shows the SEM images acquired from PT5x6 before icing and after 3 icing/deicing cycles. The coating in this case is thicker and is consisted of larger features, which may have an adverse effect on the mechanical stability of the surface structures. In fact, it seems like the effect of 3 icing/deicing cycles on PT5x6 can be compared to that on PT5x3 after 10 icing/deicing cycles. The lower durability of PT5x6 during icing/deicing

cycles can be due to the morphological and chemical differences between PT5x3 and PT5x6 which were previously discussed.

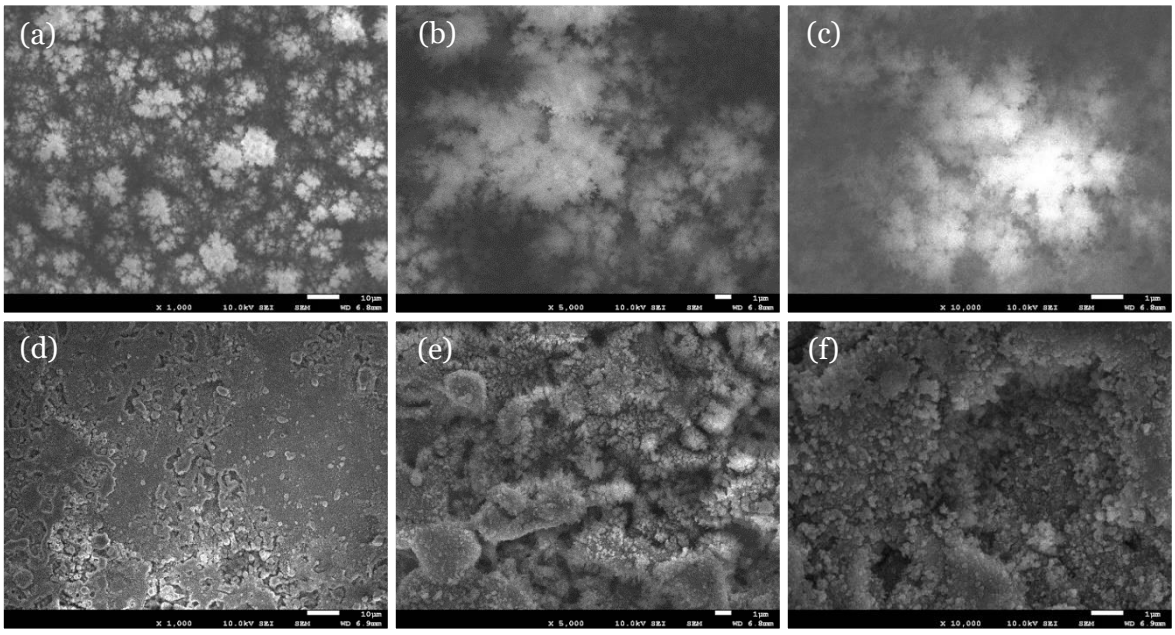

Figure 6-16. SEM images of PT5x3 before and after 10 cycles of icing deicing: (a) before icing 1000x, (b) before icing (5000x), (c) before icing 10000x, (d) after icing 1000x, (e) after icing 5000x, (f) after icing (1000x)

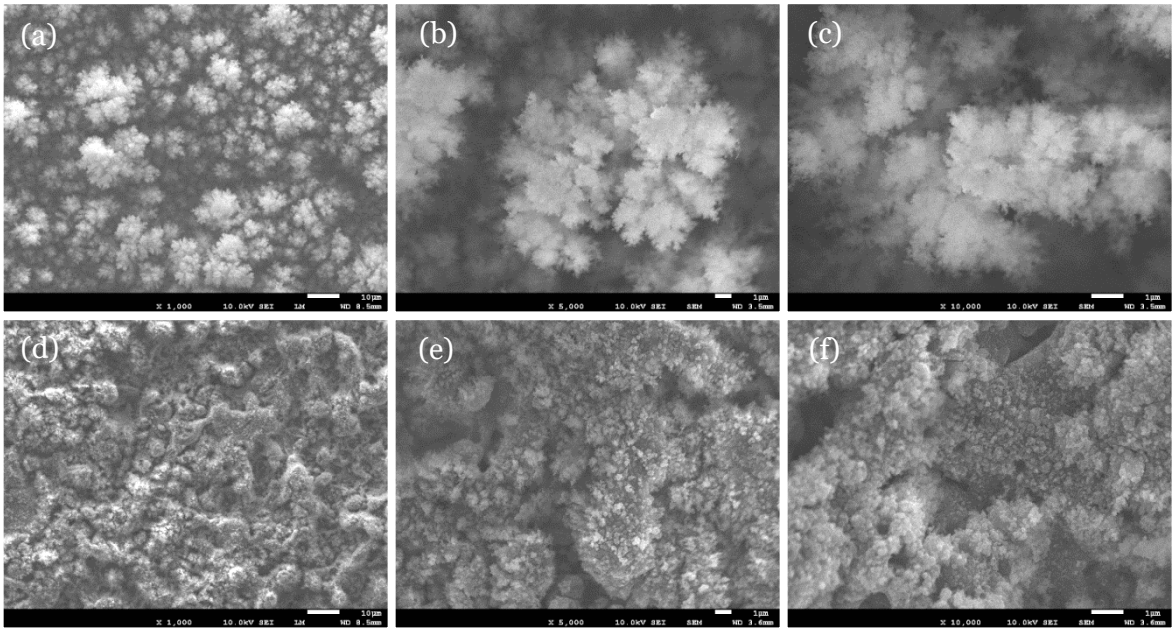

Figure 6-17. SEM images of PT5x6 before and after 3 cycles of icing deicing: (a) before icing 1000x, (b) before icing (5000x), (c) before icing 10000x, (d) after icing 1000x, (e) after icing 5000x, (f) after icing (1000x)

Figure 6-18 shows the SEM images acquired from PT5P75 before icing and after 3 icing/deicing cycles. As mentioned before, increasing the plasma generation power leads to higher monomer fragmentation, which will in turn increase the amount of silica powder deposited on the surface. This can drastically affect the coating's mechanical stability, resulting in a noticeable coating removal after only 3 icing/deicing cycles.

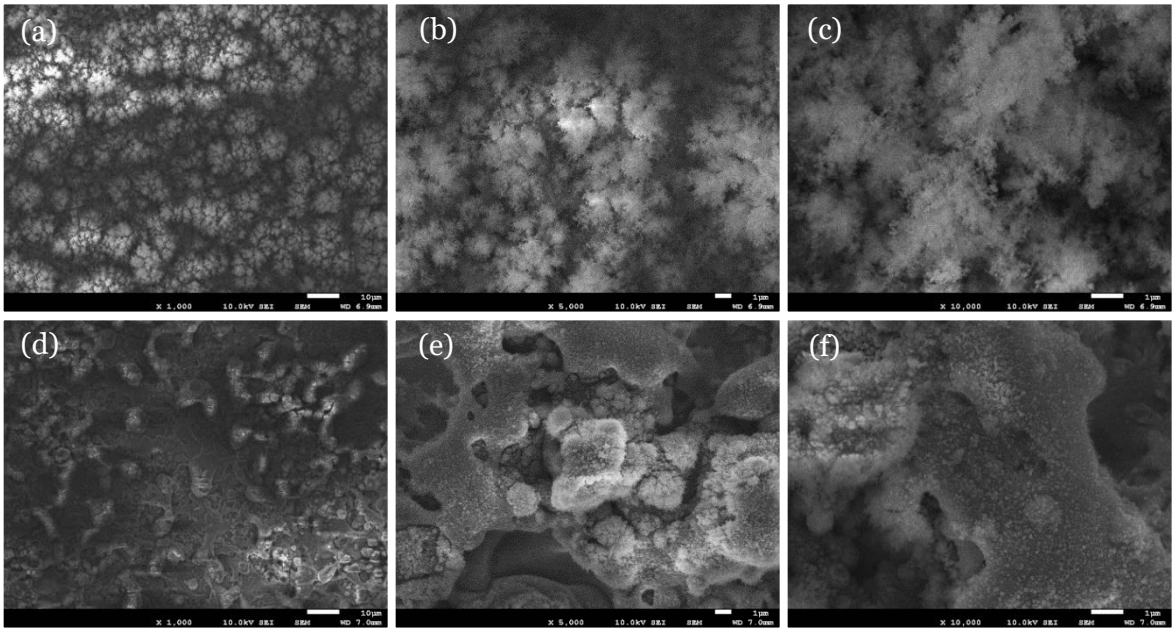

Figure 6-18. SEM images of PT5P75 before and after 3 cycles of icing deicing: (a) before icing 1000x, (b) before icing (5000x), (c) before icing 10000x, (d) after icing 1000x, (e) after icing 5000x, (f) after icing (1000x)

The coating removal observed in PT5P75 (Figure 6-18f) is significantly increased compared to PT5 after 5 icing/deicing cycles (Figure 6-15f). This suggests that with the same conditions, increasing the plasma generation power will decrease the coating's mechanical stability against icing/deicing cycles.

6.3 EFFECT OF UV EXPOSURE ON SURFACE PROPERTIES

The effect of prolonged UV exposure on surface chemical composition, surface morphology and ice adhesion strength was studied for PT5x3 and the results are presented here. Figure 6-19 shows the effect of various UV exposure durations on surface morphology

of PT5x3. Based on the SEM images presented here, it seems that UV exposure has no apparent effect on the surface morphology. This was expected since the backbone of the coating is consisted of Si_2O_4 units which, similar to almost every other ceramic, are fairly resistant to UV exposure. However, ultraviolet radiation is able to break or reorganize some of the organic bonds in the hydrophobic functions, and therefore chemical characterization of the surface was essential to fully understand the effects of ultraviolet radiation on surface behavior.

Figure 6-20 shows the variations in silicon, oxygen and carbon atomic percentages with UV exposure duration. For the first two cycles, the loss of silicon atoms is suggestive of silicon powder removal from the surface. After that, silicon content on the surface remains fairly constant. The slight increase in the atomic percentage of silicon can be attributed to the decreasing carbon percentage. There is also a sharp initial decrease in the atomic percentage of oxygen which, similar to the case of silicon, can be explained by the removal of silica powder from the surface. The subsequent increase in oxygen content can be attributed to the surface oxidation under UV exposure which is a well established phenomenon in UV degradation [219,220].

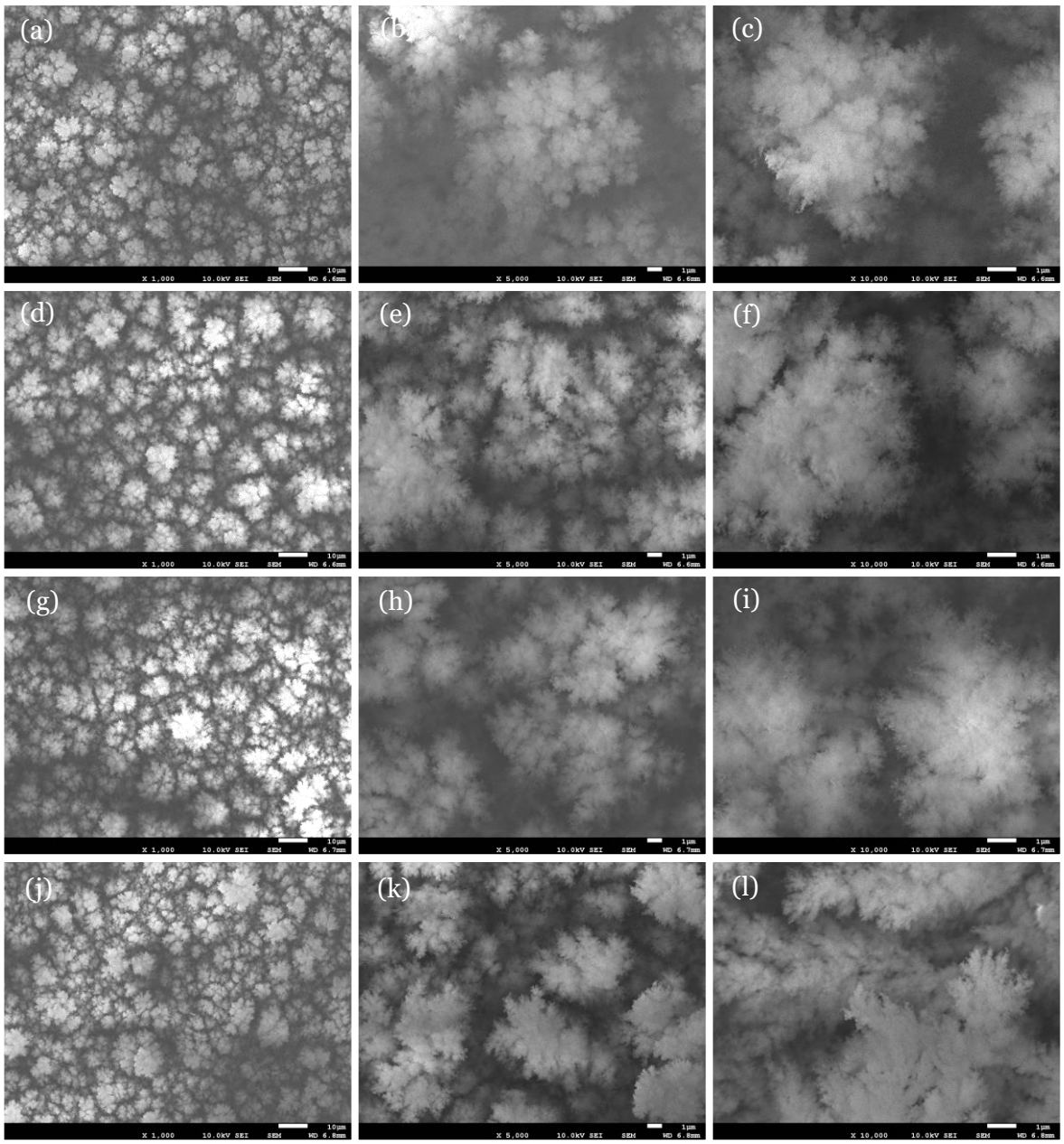

Figure 6-19. Effect of UV exposure on surface morphology: (a), (b) and (c) 1 year of UV exposure; (d), (e) and (f) 2 years of UV exposure; (g), (h) and (i) 3 years of UV exposure; and (j), (k) and (l) 4 years of UV exposure.

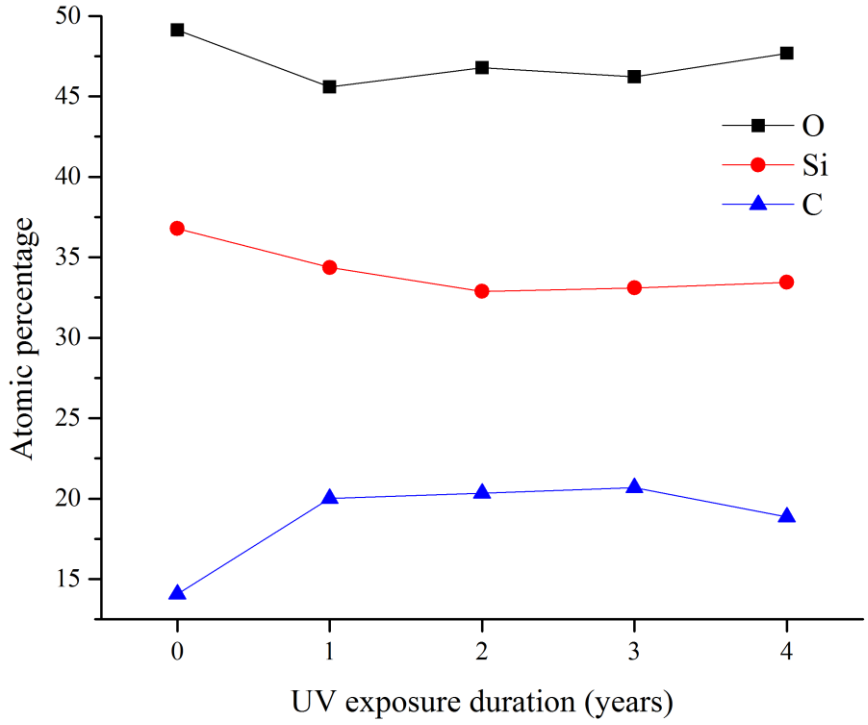

Figure 6-20. The effect of various UV exposure durations on the atomic percentage of silicon, oxygen and carbon

Figure 6-21 shows the results of Si 2p core peak curve-fitting for PT5x3 after various UV exposure durations and Figure 6-22 summarizes component quantification results. It is shown that the percentage of D decreases while the percentages of T and M increase with UV exposure duration. Since D and T are considered to be responsible for the propagation and cross-linking of siloxane structure respectively, it may be suggested that UV radiation is capable of reorganizing the methyl functions and reducing the chain length while increasing the cross-linking degree in the coating structure. This may be responsible for the lower ice adhesion strength observed in the coatings after UV exposure (Figure 6-23).

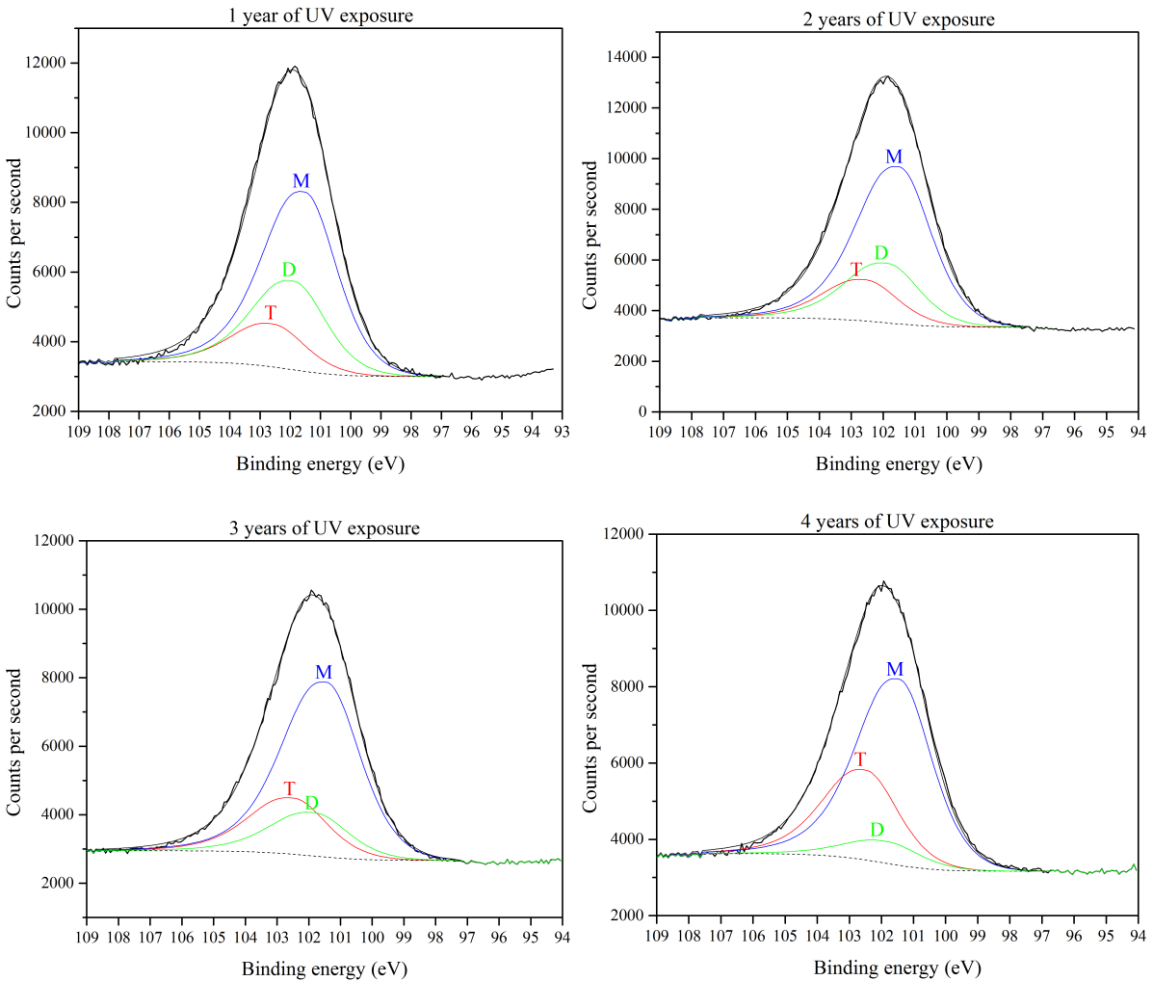

Figure 6-21. High resolution spectra of Si 2p core peak for PT5x3 after various durations of UV exposure.

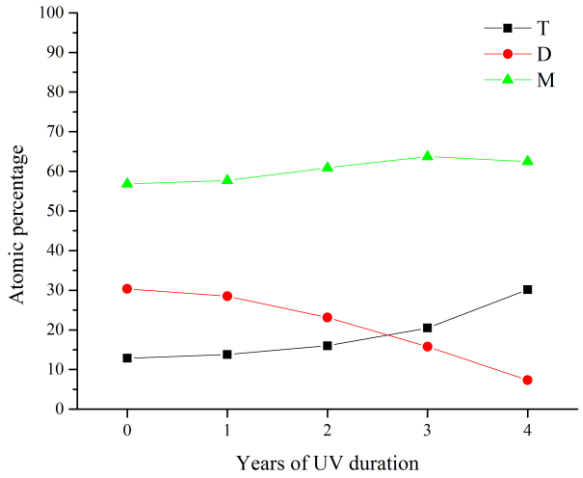

Figure 6-22. The effect of various UV exposure durations on the silicon chemical states

Figure 6-23 shows the measured ice adhesion strength on PT5x3 after various durations of UV exposure. For the first three cycles, ice adhesion strength is slightly increased. However, for the third and fourth cycle, ice adhesion strength is reduced by a factor of 2. Since it's been shown that UV exposure has no significant effect on surface morphology, and is only capable of reorganizing the organic functions in the surface structure at best, the ice adhesion strength measurement results presented here are highly unusual. This decrease in ice adhesion strength may be explained by the changes in the chemical state of silicon, but this can not be reliably confirmed unless more information on the role of silicon chemical states on surface characteristics is available.

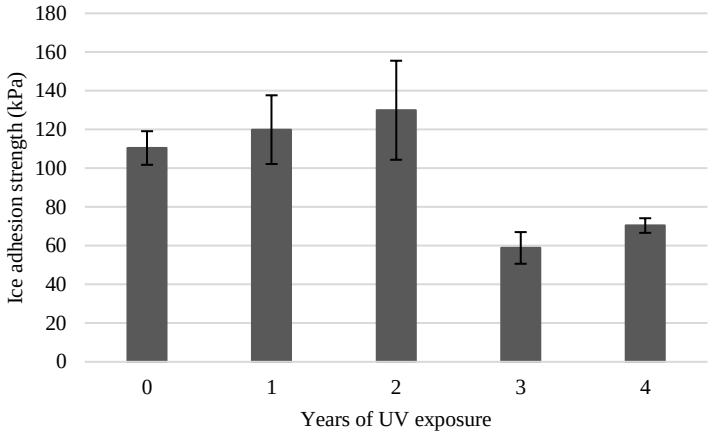

Figure 6-23. Ice adhesion strength vs. years of UV exposure for PT5x3

6.4 EFFECTS OF WATER IMMERSION ON SURFACE PROPERTIES

Samples of PT5, PT5x3 and PT5x6 were immersed in deionized water for up to 25 days and were periodically subjected to contact angle measurement and chemical analysis. Most surface properties stabilized after 25 days of water immersion, and thus immersion duration was chosen to be 25 days. Figure 6-24 shows the static contact angle and contact angle hysteresis measured on the coatings after various durations of water immersion. The general trend of static contact angle in all cases presented here is an initial decrease in water

contact angle followed by what looks like an increase. However, it is highly probable that this increase is in fact due to measurement error or sample heterogeneity. The increased contact angle observed after 6 days of water immersion may be indicative of a relatively constant contact angle after the initial loss of the coating material in water. It can be deduced that water immersion has a very similar effect on the static wetting behavior of the coating for PT5, PT5x3 and PT5x6.

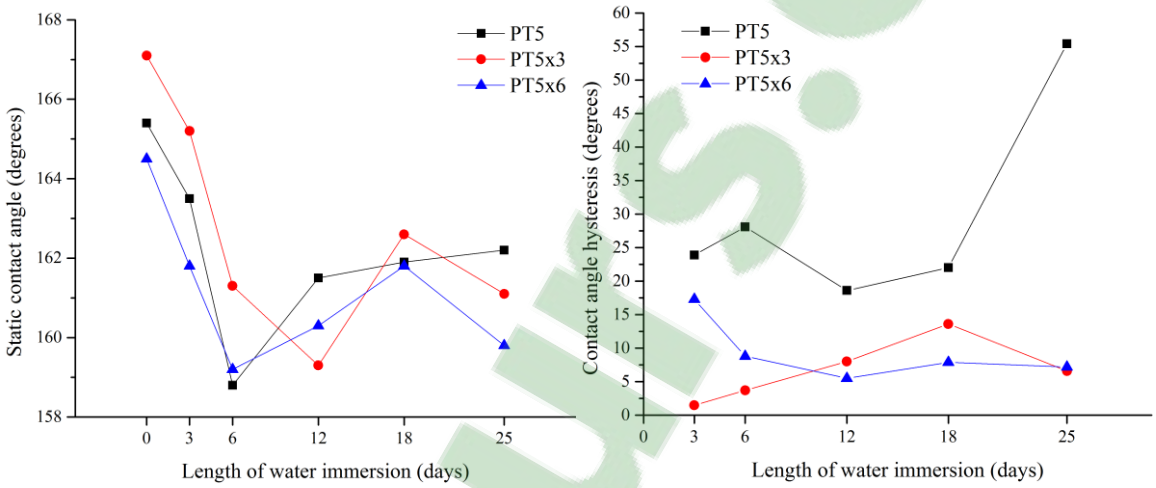

Figure 6-24. Variation of static contact angle and contact angle hysteresis after up to 25 days of water immersion for PT5, PT5x3 and PT5x6.

Unlike static contact angle, water immersion affects the contact angle hysteresis to various degrees for different coatings. In the case of PT5, contact angle hysteresis increases rapidly with water immersion duration. Since the chemical composition of PT5 is similar to that of PT5x3, this rapid increase in contact angle hysteresis should be attributed to surface morphology or coating thickness. In fact, lower thickness and smaller deposited particles in the case of PT5 may be responsible for faster loss of the coating, thus exposing the porous structure underneath and increasing the contact angle hysteresis. Compared to PT5, the rate of contact angle hysteresis increase in the case of PT5x3 is much slower which may be explained by the higher thickness of PT5x3. However, PT5x6 behaves very differently in water immersion. In this case, contact angle hysteresis decreases with water immersion

time, which cannot be explained easily based on the information provided so far. Therefore, in order to fully understand the effect of water immersion on surface properties, chemical analysis of the samples seemed necessary.

Figure 6-25 shows the atomic percentages of silicon, oxygen, and carbon on the coatings after various durations of water immersion. Loss of silicon after water immersion in the case of PT5 and PT5x3 is suggestive of the coating removal in water which was discussed previously. However, in the case of PT5x6, silicon atomic percentage increases with water immersion time and since no silicon source is provided in the water, this increase can only be due to a decrease in the atomic percentage of carbon or oxygen. In fact, PT5x6 is the only case in which a decrease in carbon percentage was observed with water immersion. Normally, an unaccounted addition of carbon can be attributed to surface contamination, but a decrease in carbon percentage can only be due to the loss of some chemical functions from the surface.

The most significant difference between the chemical compositions of PT5x3 and PT5x6 is the absence of D chemical state and an abundance of M chemical state in the case of PT5x6 (Figure 5-26). In other words, PT5x6 is consisted of shorter siloxane chains with lower cross-linking. This can reduce the stability of the siloxane structure in aqueous environment, resulting in a loss of organic functions.

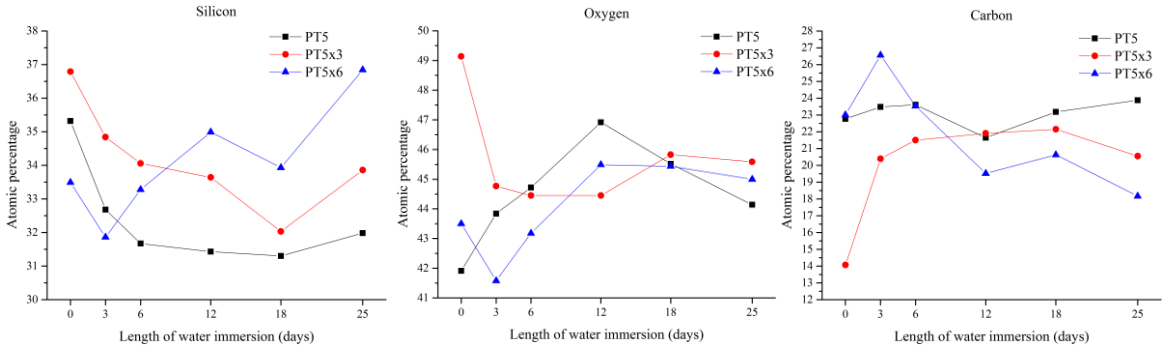

Figure 6-25. Atomic percentages of silicon, oxygen and carbon after various durations of water immersion for PT5, PT5x3 and PT5x6.

6.5 CONCLUSION

In this chapter, surface stability against some of the most well-known environmental factors was studied. It was shown that in all cases, exposing the sample to multiple icing/deicing cycles can remove coating material from the surface, which leads to a gradual increase in ice adhesion strength with the number of icing/deicing cycles. Based on SEM, XPS, and wetting analyses, it may be concluded that PT5x3 is the most stable coating against icing/deicing cycles. Due to its sufficient thickness, chemical composition, and hierarchical structure, PT5x3 is capable of retaining its icephobic characteristics for up to 10 cycles of icing/deicing. Furthermore, the effects of prolonged UV exposure on surface properties was studied for PT5x3. It was shown that UV exposure has no noticeable effect on surface morphology, but it may be capable of reorganizing organic functions in the surface structure, thus changing the silicon chemical state. This may be used to explain the unusual results acquired from ice adhesion strength measurement after the equivalent of 3 and 4 years of UV exposure, where it was shown that ice adhesion strength can decrease drastically after the 3rd year of UV exposure. Finally, the effects of water immersion on surface properties was studied for PT5, PT5x3 and PT5x6. It was shown that in all cases, static contact angle initially decreases with water immersion duration, but after around 6 days, static contact angle becomes relatively constant and does not change with the duration of water immersion. It was also shown that for PT5, contact angle hysteresis is greatly affected by water immersion duration.

It should be noted that although every effort has been made in this study to mimic the natural conditions during icing events, it is impossible to reliably estimate a coating's practical life-time based solely on the results presented in this chapter: the results presented here are valid for a single set of icing conditions (such as wind speed, temperature, droplet size, etc.). Natural icing events may occur under different, and usually fluctuating,

conditions. This can radically change the ice type and subsequently, ice adhesion strength on the coating. Besides, although the deicing method used in this study can accurately determine the adhesion strength between the ice and the substrate, it is significantly more aggressive compared to natural shedding or thawing of ice. Thus, compared to natural shedding, our deicing procedure has a much more radical effect on the coating. The best coating presented here (PT5x3) was shown to be able to maintain its icephobic properties after 10 icing/deicing cycles. However, its life time is expected to be much longer than 10 natural icing/thawing cycles.

CHAPTER 7

CONCLUSIONS AND FUTURE RECOMMENDATIONS

7.1 CONCLUSIONS AND CONTRIBUTIONS OF THIS THESIS

The development of a superhydrophobic/icephobic coating on Al-6061 substrates based on a two-step plasma-treatment procedure was reported. In the first step, aluminum samples are treated in a non-depositing environment with a relatively short jet-to-substrate distance and N_2 or N_2-O_2 plasmas. In the second step, hydrophobic materials are deposited on the surface using N_2 plasma and hexamethyldisiloxane (HMDSO) as the precursor.

The first step is introduced as a path to increase surface roughness and facilitate the creation of superhydrophobic surface structures. A microporous structure is observed on the surface of aluminum after 3 passes of N_2-O_2 plasma treatment. SEM studies reveal the presence of various surface features after the first pass, some of which are very similar to the structures observed in laser ablation. Furthermore, XPS studies reveal that the surface is heavily oxidized after N_2-O_2 plasma treatment. High speed imaging of the N_2 or N_2-O_2 plasma interacting with the surface shows that multiple streamers are created as an expansion of the rotating arc source inside the jet body. In the case of N_2-O_2 plasma, the formation of this streamer is facilitated by the near-infinite electric conductivity of the plasma column, in contrast with the case of N_2 plasma, where it was shown that the

streamers are significantly weaker, suggesting that the N_2 plasma is not as conductive as N_2-O_2 plasma. It is argued that these streamers are responsible for delivering electric charges from the plasma source to a close proximity of the surface. Subsequently, multiple electric arcs can be transferred onto the surface which are believed to be the driving force behind the transformation mechanism. It is shown that the upper energy flux limit of the plasma jet is comparable to a typical case of laser ablation. This allows us to draw some similarities between surface features observed after laser ablation and surface features observed after one pass of N_2-O_2 plasma treatment. In fact, different laser pulse durations and different beam fluences can give rise to different surface features, some of which are observed in our case. For instance, ultrashort laser pulses (in the range of femtoseconds) can lead to circular features with 'clean' edges, which are the result of a direct solid-to-gas phase transformation, since the energy delivery timeframe does not allow for substrate melting. In longer pulse durations (in the range of pico/nanoseconds) with low beam fluence enough time is provided for melting and re-solidification, which leads to the re-deposition of molten aluminum on the edges of surface features. In nanoseconds durations with higher beam fluence, the homogeneous nucleation of vapor from molten aluminum results in a micro-roughened and micro-porous surface structure. In the case of APPJ treatment, since the occurrence of electric arcs due to the streamers seems to be randomly distributed in time and space, it may be suggested that multiple arcs with various durations are capable of delivering significant amounts of energy to the surface. This will lead to different surface features based on arc duration and energy. It is argued that these arcs favor irregularities with different electrical properties on the surface of aluminum. Since each treatment pass is introducing more irregularities to the surface, a feature created in the first pass may be a preferable spot for further electric arcs in the second pass. Therefore, by exposing the sample to multiple passes of N_2-O_2 plasma, a uniform micro-roughened and micro-porous surface structure is achieved which may be used as a substrate for coating deposition.

The main objective of the next step is to develop a superhydrophobic/icephobic coating on Al-6061 through APPJ treatment in a depositing environment. In order to do so, some of the major plasma parameters should be closely investigated and a simple modification to the jet should be carried out. At first, the effect of HMDSO flow rate and plasma gas on surface properties was studied. It was shown that static contact angle initially increases with precursor flow rate, but a critical flow rate exists beyond which contact angle remains fairly constant. This critical value was attributed to the full coverage of the aluminum surface with hydrophobic materials. However, a white powder was observed on the surfaces developed using precursor flow rates above a certain threshold, which can decrease the mechanical properties of the coating. This white powder was shown to be due to the agglomeration of silica-based spherical nano-particles observed in the lower precursor flow rates. Therefore, in order to avoid the generation of white powder particles, flow rate should be kept low. Furthermore, FTIR studies revealed that by increasing the precursor flow rate, the amount of organic deposition increases. However, surfaces developed using N_2 plasma are more organic and are consisted of smaller surface features compared to the ones developed using N_2-O_2 plasma. Therefore, it was concluded that N_2 plasma with low precursor flow rates (lower than 10 g/h) is the more preferred choice for hydrophobic applications.

In development of hydrophobic coatings, it is essential to avoid the presence of hydrophilic oxide groups in the coating structure as much as possible. In order to prevent the diffusion of O_2 from the ambient air into the plasma region, the plasma jet is slightly modified with a quartz tube. It is shown that the addition of this quartz tube to the jet-head can drastically change the surface morphology, leading to a hierarchical structure which is ideal for hydrophobic applications. Furthermore, the quartz tube added to the jet allows for ignition and maintenance of weak plasmas while reducing the diffusion of oxygen species

from ambient air into the plasma, ultimately decreasing the amount of powder particles deposited on the aluminum surface and improving the mechanical properties of the coating.

In the next step, after the jet modification, superhydrophobic/icephobic coatings are developed in the presence of HMDSO in N_2 plasma. Multiple samples are created using different precursor flow rates, generation powers and number of deposition passes in order to specifically study the effects of these parameters on surface properties.

In the case of the lowest precursor flow rate studied (3 g/h, PT3), it is shown that the presence of precursor molecules in the plasma is not enough for a complete and uniform coverage of the surface. On the other hand, by increasing the precursor flow rate to 7 g/h (PT7), coating materials may completely cover some surface features originated from the N_2-O_2 plasma treatment step, leading to a '*morphological saturation*' of the surface. The most preferred surface structure is observed in the case of PT5, where despite the complete coverage of the surface with organosilicons, surface features created during the N_2-O_2 plasma treatment are maintained, leading to a hierarchical structure with surface features ranging from tens of micrometers to only a few nanometers. Such structures are shown to be preferable for superhydrophobic and icephobic applications.

Further samples are developed using precursor flow rates of 3 g/h and 5 g/h with multiple passes of plasma deposition. It is shown that increasing the number of deposition passes leads to a thicker coating with larger deposited particles on the surface. Multiple passes of plasma deposition can also affect coating's chemical composition. Every plasma deposition pass after the first one is performed in the presence of a pre-deposited dielectric layer, the thickness of which depends on the deposition parameters. This layer may affect the electrical properties of the plasma. It is shown that plasma becomes denser in the presence of this dielectric layer, leading to a lower monomer fragmentation degree. This is in agreement with FTIR results, where it is shown that monomer over-fragmentation in a

few cases can lead to the deposition of some chemical groups on the surface, particularly Si-O-C, C-H or Si-H. The presence of these functions is only significant in cases where over-fragmentation is expected, such as PT3x3 or PT5P75, and are believed to be formed due to the chemical reactions between ambient air species and monomer over-fragmentation products. XPS studies show that by increasing the number of passes to 6 in the case of PT5, siloxane chains on the surface become shorter with a higher density of methyl groups, which can decrease coating's mechanical stability against icing deicing cycles. Besides, unlike PT5x3, PT5x6 exhibits morphological saturation to some degree, which may contribute to the lower contact angle and higher ice adhesion strength observed in the case of PT5x6.

Finally, it is shown that increasing the plasma power from 2.7 kW to 3.6 kW leads to monomer over-fragmentation and higher oxide deposition on the surface which can contribute to the higher ice adhesion strength for PT5P75.

It is concluded that the sample prepared using a precursor flow rate of 5 g/h with 3 passes of plasma deposition shows the best superhydrophobic/icephobic properties among the conditions studied here. Ice adhesion strength is measured on PT5x3 for up to 10 cycles of icing/deicing, and it is shown that PT5x3 can reduce the ice adhesion strength by a factor of at least 2 for the first 7 cycles. After 10 cycles, ice adhesion strength on PT5x3 is still lower than untreated sample by a factor of 1.5.

In chapter 6, coating's stability against natural factors is investigated. Various coatings are exposed to multiple cycles of icing/deicing and their surface properties are studied during these cycles. SEM studies show that multiple icing/deicing cycles lead to different degrees of coating removal in all cases. This is further confirmed by XPS results, where a reduction in silicon and oxygen atomic percentages was observed on all samples after icing/deicing cycles. However, PT5x3 is shown to be able to retain some degree of its multi-leveled roughness even after 10 cycles of icing/deicing. This is in agreement with ice

adhesion strength measurements, where PT5x3 is shown to be the least affected by the icing/deicing cycles.

The integrity of PT5x3 during prolonged UV exposure durations is also studied. It is shown that UV exposure has no noticeable effect on surface morphology, however it is capable of reorganizing the organic functions in the surface structure, thus changing the silicon chemical state, increasing the density of organic function on the surface while decreasing siloxane chains length. Ice adhesion strength is shown to decrease significantly after the equivalent of 2 years of UV exposure. This is explained by a denser presence of methyl groups on the surface (higher percentage of M functions).

Finally, the effects of water immersion on the surface properties of PT5, PT5x3 and PT5x6 is studied. It is shown that in all cases, static contact angle initially decreases before it becomes stable after around 6 days of water immersion. However, a rapid increase in contact angle hysteresis is observed on PT5x3 after around 12 days of water immersion, which is attributed to the loss of finer surface features in aqueous environment. Furthermore, XPS studies reveal that in the case of PT5x6, some organic functions are lost after water immersion. This is in agreement with the initial XPS studies on PT5x6, where it is suggested that the absence of D groups in the siloxane structure may be responsible for the lower mechanical integrity of the surface.

7.2 RECOMMENDATIONS FOR FUTURE WORK

Further studies as a continuation of this research can be focused on the following aspects:

- The effects of all plasma parameters on surface wetting and icing properties should be fully studied. In this study, we've chosen some of the plasma parameters that are believed to have the most pronounced effect on surface properties. However, some plasma parameters are left to be investigated. For instance, the length of the silicon

tube used to confine the plasma jet and hinder the diffusion of oxygen into the plasma plays a role in coating's composition and morphology, but this correlation is not studied here. Plasma frequency, plasma duty cycle, ionization gas flow rate and carrier gas flow rate are some of the other plasma parameters that may affect the coating's properties.

- Another potential study may be focused on precise and direct measurement of the energy and duration of the electric arcs on the surface during the N_2-O_2 treatment process. During this study, several efforts were made to measure arc duration and energy. However, due to the very short duration of the arcs and their hectic nature, none of these efforts were successful. Therefore, an experiment should be designed to accurately measure the energy and the duration of the arcs, so that the similarities between N_2-O_2 plasma treatment introduced here and some of the known processes can be clarified. For instance, an arc generator with controlled arc energy/duration can be used on the surface to confirm the distribution of various surface features based on arc energy and arc duration.
- A hypothesis was presented to explain the variations in surface chemical composition with the number of deposition passes based on organic functions ejection from the surface during deposition. The results presented in this thesis are consistent with this hypothesis, but in order to reliably evaluate the validity of such explanation, it is recommended to study the chemical composition of the plasma more accurately. For instance, mass spectroscopy of the plasma interacting with a previously deposited organo-silicon based coating can prove or disprove the presence of methyl groups ejected from the surface.
- As mentioned before, a set of icing conditions (wind speed, temperature, droplet size, etc) is chosen in this study for ice accumulation which is relatively close to what one would expect in natural icing events. However, different climates can drastically

change the ice type, which in turn affects the ice adhesion strength measurements. Therefore, to reliably evaluate the icephobic properties of a coating, the effects of icing conditions on ice adhesion strength and ice shedding capabilities should be understood.

- The coatings presented in this thesis are designed with high voltage over-head cables in mind, and therefore, in practical applications, they will be subjected to high voltage currents. Thus, it is recommended to study the inter-relation between electrical parameters, such as electric fields or the intensity and the polarity of the voltage, and coating characteristics. For instance, the formation of corona discharges on the needle-like structures on the surface can be problematic in many applications, and therefore the significance of corona discharges in the presence of surface micro/nano-structure should be studied prior to any implementation in practical applications.
- As mentioned before, in siloxane coatings, four different silicon chemical states are defined based on the number of oxygen atoms in contact with silicon. Using Si 2p core peak curve-fitting, the atomic percentages of each one of these states can be determined. However, no study has ever been done on the contributions of these states to coating's macro-properties, such as wetting and icing behavior or mechanical integrity. This may be done by studying standard samples with known contents of Q, T, D, and M. For instance, polydimethylsiloxane is fully consisted of D unit. Therefore, PDMS may be used as a D standard sample. Establishing a correlation between the presence of these functions and some practical properties of the coating can be used to fully understand and explain the surface behavior in various cases.
- While the effects of UV exposure on ice adhesion strength was briefly discussed, more work can be done to fully understand the role of UV on ice adhesion strength and

coating stability. Firstly, the effects of aging parameters, such as UV wavelength or humidity, on UV degradation process can be studied. Besides, if the explanation given here for the reduced adhesion strength after 3 years of UV exposure is true, then it is expected to observe a lower stability against icing/deicing cycles in samples after 3 and 4 years of UV exposure, since it was suggested that UV radiation can reorganize the organic functions in the coating leading to shorter siloxane chain lengths. Therefore, another path to further improve our understanding of these coatings is to measure the ice adhesion strength on samples exposed to UV radiation during multiple cycles of icing/deicing.

REFERENCES

[1] Canada's Top Ten Weather Stories of 1998, Environment Canada. (2011). https://www.ec.gc.ca/meteo-weather/default.asp?lang=En&n=FA49AB5D-1 (accessed January 30, 2017).

[2] The 1998 ice storm: 10-year retrospective - RMS Special Report, New Ark, CA, 2008. http://forms2.rms.com/rs/729-DJX-565/images/wtr_1998_ice_storm_10_retrospective.pdf.

[3] E.L. Lecomte, A.W. Pang, J.W. Russell, Ice Storm '98, Institute for Catastrophic Loss Reduction, Ottawa, ON, Canada and Institute for Business and Home Safety, Boston, MA, USA. 1 (1998) 47.

[4] C.C. Ryerson, Assessment of Superstructure Ice Protection as Applied to Offshore Oil Operations Safety: Problems, Hazards, Needs, and Potential Transfer Technologies, 2008.

[5] M. Farzaneh, Atmospheric icing of power networks, in: Atmospheric Icing of Power Networks, Springer, Berlin, 2008: pp. 1–381. doi:10.1007/978-1-4020-8531-4.

[6] H. Sojoudi, M. Wang, N.D. Boscher, G.H. McKinley, K.K. Gleason, Durable and scalable icephobic surfaces: similarities and distinctions from superhydrophobic surfaces., Soft Matter. 12 (2016) 1938–63. doi:10.1039/c5sm02295a.

[7] A.J. Eliasson, M. Farzaneh, S.M. Fikke, A. Haldar, M. Isozaki, F. Jakl, R. Lake, A. Leblond, M. Minchin, M. Mito, C.C. Ryerson, V. Shkaptsov, J.B. Wareing, B. Anderson, M. Kermani, L. Kollar, R. Menini, Z. Peter, C. Volat, CIGRE Working Group B2.29: Systems for prediction and monitoring of ice shedding, anti-icing and de-icing for power line conductors and ground wires, 2010.

[8] W. Barthlott, C. Neinhuis, Purity of the sacred lotus, or escape from contamination in biological surfaces, Planta. 202 (1997) 1–8. doi:10.1007/s004250050096.

[9] Z. Guo, W. Liu, B.L. Su, Why so strong for the lotus leaf?, Applied Physics Letters. 93 (2008) 201909. doi:10.1063/1.3036535.

[10] T. Young, An Essay on the Cohesion of Fluids, Philosophical Transactions of the Royal Society of London. 95 (1805) 65–87. doi:10.1098/rstl.1805.0005.

[11] R.N. Wenzel, Resistance of Solid Surfaces To Wetting By Water, Industrial & Engineering Chemistry. 28 (1936) 988–994. doi:10.1021/ie50320a024.

[12] A.B.D. Cassie, S. Baxter, Wettability of porous surfaces, Transactions of the Faraday Society. 40 (1944) 546–551. doi:10.1039/TF9444000546.

[13] C. Ishino, K. Okumura, Wetting transitions on textured hydrophilic surfaces, European Physical Journal E. 25 (2008) 415–424. doi:10.1140/epje/i2007-10308-y.

[14] C. Ishino, K. Okumura, D. Quere, No TitWetting transitions on rough surfaces le, Europhysics Letters. 68 (2004) 419–425.

[15] E. Bormashenko, R. Grynyov, Plasma treatment induced wetting transitions on biological tissue (pigeon feathers), Colloids and Surfaces B: Biointerfaces. 92 (2012) 367–371. doi:10.1016/j.colsurfb.2011.11.053.

[16] G. Wolansky, A. Marmur, Apparent contact angles on rough surfaces: The Wenzel equation revisited, Colloids and Surfaces A: Physicochemical and Engineering Aspects. 156 (1999) 381–388. doi:10.1016/S0927-7757(99)00098-9.

[17] A. Marmur, Wetting on hydrophobic rough surfaces: To be heterogeneous or not to be?, Langmuir. 19 (2003) 8343–8348. doi:10.1021/la0344682.

[18] S. Brandon, N. Haimovich, E. Yeger, A. Marmur, Partial wetting of chemically patterned surfaces: The effect of drop size, Journal of Colloid and Interface Science. 263 (2003) 237–243. doi:10.1016/S0021-9797(03)00285-6.

[19] M. Ma, R.M. Hill, {S}uperhydrophobic surfaces, Koninklije Brill NV, Leiden, 2006. doi:10.1016/j.cocis.2006.06.002.

[20] M. Strobel, C.S. Lyons, An essay on contact angle measurements, Plasma Processes and Polymers. 8 (2011) 8–13. doi:10.1002/ppap.201000041.

[21] A.M. Kietzig, Comments on “an essay on contact angle measurements” - An illustration of the respective influence of droplet deposition and measurement parameters, Plasma Processes and Polymers. 8 (2011) 1003–1009. doi:10.1002/ppap.201100114.

[22] M. Müller, C. Oehr, Comments on “an essay on contact angle measurements” by Strobel and Lyons, Plasma Processes and Polymers. 8 (2011) 19–24. doi:10.1002/ppap.201000115.

[23] C.G. Ngan, E.B. Dussan V., On the nature of the dynamic contact angle: an experimental study, Journal of Fluid Mechanics. 118 (1982) 27–40. doi:10.1017/S0022112082000949.

[24] R. Tadmor, Line energy and the relation between advancing, receding, and Young contact angles, Langmuir. 20 (2004) 7659–7664. doi:10.1021/la049410h.

[25] F.J. Montes Ruiz-Cabello, M.A. Rodríguez-Valverde, M.A. Cabrerizo-Vílchez, Additional comments on “an essay on contact angle measurements” by M. Strobel and C. S. Lyons, Plasma Processes and Polymers. 8 (2011) 363–366. doi:10.1002/ppap.201100043.

[26] N. Shirtcliffe, P. Thiemann, M. Stratmann, G. Grundmeier, Chemical structure and morphology of thin, organo-silicon plasma-polymer films as a function of process parameters, Surface and Coatings Technology. 142–144 (2001) 1121–1128. doi:10.1016/S0257-8972(01)01226-9.

[27] Z. Guo, W. Liu, B.L. Su, Superhydrophobic surfaces: From natural to biomimetic to functional, Journal of Colloid and Interface Science. 353 (2011) 335–355. doi:10.1016/j.jcis.2010.08.047.

[28] R. Di Mundo, F. Palumbo, R. D’Agostino, Nanotexturing of polystyrene surface in fluorocarbon plasmas: from sticky to slippery superhydrophobicity, Langmuir. 24

(2008) 5044–5051. doi:10.1021/la800059a.

[29] W. Chen, A.Y. Fadeev, M.C. Hsieh, D. Öner, J. Youngblood, T.J. McCarthy, Ultrahydrophobic and ultralyophobic surfaces: some comments and examples, Langmuir. 15 (1999) 3395–3399. doi:10.1021/la990074s.

[30] R. Jafari, M. Farzaneh, Fabrication of superhydrophobic nanostructured surface on aluminum alloy, Applied Physics A: Materials Science and Processing. 102 (2011) 195–199. doi:10.1007/s00339-010-6131-0.

[31] B. Balu, V. Breedveld, D.W. Hess, Fabrication of "roll-off" and "sticky" superhydrophobic cellulose surfaces-via plasma processing, Langmuir. 24 (2008) 4785–4790. doi:10.1021/la703766c.

[32] P. Favia, G. Cicala, A. Milella, F. Palumbo, P. Rossini, R. d'Agostino, Deposition of super-hydrophobic fluorocarbon coatings in modulated RF glow discharges, Surface and Coatings Technology. 169–170 (2003) 609–612. doi:10.1016/S0257-8972(03)00123-3.

[33] R. Saraf, H.J. Lee, S. Michielsen, J. Owens, C. Willis, C. Stone, E. Wilusz, Comparison of three methods for generating superhydrophobic, superoleophobic nylon nonwoven surfaces, Journal of Materials Science. 46 (2011) 5751–5760. doi:10.1007/s10853-011-5530-8.

[34] X.-M. Li, D. Reinhoudt, M. Crego-Calama, What do we need for a superhydrophobic surface? A review on the recent progress in the preparation of superhydrophobic surfaces., Chemical Society Reviews. 36 (2007) 1350–1368. doi:10.1039/b602486f.

[35] M. Ma, R.M. Hill, Superhydrophobic surfaces, Current Opinion in Colloid and Interface Science. 11 (2006) 193–202. doi:10.1016/j.cocis.2006.06.002.

[36] M. Farzaneh, D.K. Sarkar, Nanostructured Superhydrophobic Coatings, Journal of CPRI. 4 (2008) 135–147.

[37] Z. Guo, W. Liu, Biomimic from the superhydrophobic plant leaves in nature: Binary structure and unitary structure, Plant Science. 172 (2007) 1103–1112. doi:10.1016/j.plantsci.2007.03.005.

[38] R.E. Johnson, R.H. Dettre, Contact Angle Hysteresis. III. Study of an Idealized Heterogeneous Surface, The Journal of Physical Chemistry. 68 (1964) 1744–1750. doi:10.1021/j100789a012.

[39] J. Ma, Y. Sun, K. Gleichauf, J. Lou, Q. Li, Nanostructure on taro leaves resists fouling by colloids and bacteria under submerged conditions, Langmuir. 27 (2011) 10035–10040. doi:10.1021/la2010024.

[40] Y.Y. Yan, N. Gao, W. Barthlott, Mimicking natural superhydrophobic surfaces and grasping the wetting process: A review on recent progress in preparing superhydrophobic surfaces, Advances in Colloid and Interface Science. 169 (2011) 80–105. doi:10.1016/j.cis.2011.08.005.

[41] K.H. Kale, S. Palaskar, Atmospheric pressure plasma polymerization of hexamethyldisiloxane for imparting water repellency to cotton fabric, Textile Research Journal. 81 (2010) 608–620. doi:10.1177/0040517510385176.

[42] S.H. Kim, J.H. Kim, B.K. Kang, H.S. Uhm, Superhydrophobic CF x coating via in-line atmospheric RF plasma of He-CF 4-H 2, Langmuir. 21 (2005) 12213–12217. doi:10.1021/la0521948.

[43] J. Zhang, P. France, A. Radomyselskiy, S. Datta, J. Zhao, W. Van Ooij, Hydrophobic cotton fabric coated by a thin nanoparticle plasma film, Journal of Applied Polymer Science. 88 (2003) 1473–1481. doi:10.1002/app.11831.

[44] X. Yao, Y. Song, L. Jiang, Applications of bio-inspired special wettable surfaces, Advanced Materials. 23 (2011) 719–734. doi:10.1002/adma.201002689.

[45] N.J. Shirtcliffe, G. McHale, M.I. Newton, The superhydrophobicity of polymer surfaces: Recent developments, Journal of Polymer Science, Part B: Polymer Physics. 49 (2011) 1203–1217. doi:10.1002/polb.22286.

[46] A. Alizadeh, M. Yamada, R. Li, W. Shang, S. Otta, S. Zhong, L. Ge, A. Dhinojwala, K.R. Conway, V. Bahadur, A.J. Vinciquerra, B. Stephens, M.L. Blohm, Dynamics of ice nucleation on water repellent surfaces, Langmuir. 28 (2012) 3180–3186. doi:10.1021/la2045256.

[47] M. Farzaneh, Ice accretions on high–voltage conductors and insulators and related phenomena, Philosophical Transactions of the Royal Society of London A: Mathematical, Physical and Engineering Sciences. 358 (2000) 2971–3005. doi:10.1098/rsta.2000.0692.

[48] L. Foroughi Mobarakeh, R. Jafari, M. Farzaneh, Superhydrophobic Surface Elaboration Using Plasma Polymerization of Hexamethyldisiloxane (HMDSO), Advanced Materials Research. 409 (2011) 783–787. doi:10.4028/www.scientific.net/AMR.409.783.

[49] R. Jafari, R. Menini, M. Farzaneh, Superhydrophobic and icephobic surfaces prepared by RF-sputtered polytetrafluoroethylene coatings, Applied Surface Science. 257 (2010) 1540–1543. doi:10.1016/j.apsusc.2010.08.092.

[50] H. Lim, D.H. Jung, J.H. Noh, G.R. Choi, W.D. Kim, Simple nanofabrication of a superhydrophobic and transparent biomimetic surface, Chinese Science Bulletin. 54 (2009) 3613–3616. doi:10.1007/s11434-009-0274-4.

[51] A. Milella, R. Di Mundo, F. Palumbo, P. Favia, F. Fracassi, R. d'Agostino, Plasma nanostructuring of polymers: Different routes to superhydrophobicity, Plasma Processes and Polymers. 6 (2009) 460–466. doi:10.1002/ppap.200930011.

[52] J. Genzer, K. Efimenko, Recent developments in superhydrophobic surfaces and their relevance to marine fouling: a review., Biofouling. 22 (2006) 339–360. doi:10.1080/08927010600980223.

[53] S. Wang, L. Feng, L. Jiang, One-step solution-immersion process for the fabrication of stable bionic superhydrophobic surfaces, Advanced Materials. 18 (2006) 767–770. doi:10.1002/adma.200501794.

[54] E. Hermelin, J. Petitjean, J.C. Lacroix, K.I. Chane-Ching, J. Tanguy, P.C. Lacaze, Ultrafast electrosynthesis of high hydrophobic polypyrrole coatings on a zinc electrode: Applications to the protection against corrosion, Chemistry of Materials. 20 (2008) 4447–4456. doi:10.1021/cm703658t.

[55] F. Zhang, L. Zhao, H. Chen, S. Xu, D.G. Evans, X. Duan, Corrosion resistance of superhydrophobic layered double hydroxide films on aluminum, Angewandte Chemie - International Edition. 47 (2008) 2466–2469. doi:10.1002/anie.200704694.

[56] H.F. Hoefnagels, D. Wu, G. De With, W. Ming, Biomimetic superhydrophobic and highly oleophobic cotton textiles, Langmuir. 23 (2007) 13158–13163.

doi:10.1021/la702174x.

[57] F.L. Huang, Q.F. Wei, W.Z. Xu, Q. Li, Preparation and characterization of PTFE gradient nanostructure on silk fabric, Surf. Rev. Lett. 14 (2007) 547–551. doi:Doi 10.1142/S0218625x07009827.

[58] X. Zhang, M. Jin, Z. Liu, D.A. Tryk, S. Nishimoto, T. Murakami, A. Fujishima, Superhydrophobic TiO2 surfaces: Preparation, photocatalytic wettability conversion, and superhydrophobic-superhydrophilic patterning, Journal of Physical Chemistry C. 111 (2007) 14521–14529. doi:10.1021/jp0744432.

[59] N.D. Boscher, P. Choquet, D. Duday, S. Verdier, Chemical compositions of organosilicon thin films deposited on aluminium foil by atmospheric pressure dielectric barrier discharge and their electrochemical behaviour, Surface and Coatings Technology. 205 (2010) 2438–2448. doi:10.1016/j.surfcoat.2010.09.037.

[60] E. Hosono, S. Fujihara, I. Honma, H. Zhou, Superhydrophobic perpendicular nanopin film by the bottom-up process, Journal of the American Chemical Society. 127 (2005) 13458–13459. doi:10.1021/ja053745j.

[61] X. Zhang, F. Shi, X. Yu, H. Liu, Y. Fu, Z. Wang, L. Jiang, X. Li, Polyelectrolyte Multilayer as Matrix for Electrochemical Deposition of Gold Clusters: Toward Super-Hydrophobic Surface, Journal of the American Chemical Society. 126 (2004) 3064–3065. doi:10.1021/ja0398722.

[62] M.E. Buck, S.C. Schwartz, D.M. Lynn, Superhydrophobic thin films fabricated by reactive layer-by-layer assembly of azlactone-functionalized polymers, Chemistry of Materials. 22 (2010) 6319–6327. doi:10.1021/cm102115e.

[63] Y. Ofir, B. Samanta, P. Arumugam, V.M. Rotello, Controlled fluorination of FePt nanoparticles: Hydrophobic to superhydrophobic surfaces, Advanced Materials. 19 (2007) 4075–4079. doi:10.1002/adma.200700169.

[64] K. Ramaratnam, V. Tsyalkovsky, V. Klep, I. Luzinov, Ultrahydrophobic textile surface via decorating fibers with monolayer of reactive nanoparticles and non-fluorinated polymer., Chemical Communications (Cambridge, England). 2007 (2007) 4510–4512. doi:10.1039/b709429a.

[65] L. Zhai, F.C. Cebeci, R.E. Cohen, M.F. Rubner, Stable superhydrophobic coatings from polyelectrolyte multilayers, Nano Letters. 4 (2004) 1349–1353. doi:10.1021/nl049463j.

[66] Y. Zhang, X. Yu, H. Wu, J. Wu, Facile fabrication of superhydrophobic nanostructures on aluminum foils with controlled-condensation and delayed-icing effects, Applied Surface Science. 258 (2012) 8253–8257. doi:10.1016/j.apsusc.2012.05.032.

[67] S.A. Kulinich, M. Farzaneh, How wetting hysteresis influences ice adhesion strength on superhydrophobic surfaces, Langmuir. 25 (2009) 8854–8856. doi:10.1021/la901439c.

[68] S. Farhadi, M. Farzaneh, S.A. Kulinich, Anti-icing performance of superhydrophobic surfaces, Applied Surface Science. 257 (2011) 6264–6269. doi:10.1016/j.apsusc.2011.02.057.

[69] A.J. Meuler, J.D. Smith, K.K. Varanasi, J.M. Mabry, G.H. McKinley, R.E. Cohen, Relationships between water wettability and ice adhesion, ACS Applied Materials and Interfaces. 2 (2010) 3100–3110. doi:10.1021/am1006035.

[70] S.B. Subramanyam, K. Rykaczewski, K.K. Varanasi, Ice adhesion on lubricant-

impregnated textured surfaces, Langmuir. 29 (2013) 13414–13418. doi:10.1021/la402456c.

[71] K.K. Varanasi, T. Deng, J.D. Smith, M. Hsu, N. Bhate, Frost formation and ice adhesion on superhydrophobic surfaces, Applied Physics Letters. 97 (2010) 234102. doi:10.1063/1.3524513.

[72] L. Makkonen, Ice Adhesion —Theory, Measurements and Countermeasures, Journal of Adhesion Science and Technology. 26 (2012) 413–445. doi:10.1163/016942411X574583.

[73] N. Srikanth, E. Liu, P. Wilson, Z. Chen, Development of Sol – Gel Icephobic Coatings: Effect of Surface Roughness and Surface Energy, Applied Materials & Interfaces. (2014).

[74] D.K. Sarkar, M. Farzaneh, Superhydrophobic Coatings with Reduced Ice Adhesion, Journal of Adhesion Science and Technology. 23 (2009) 1215–1237. doi:10.1163/156856109X433964.

[75] Y. Wang, J. Xue, Q. Wang, Q. Chen, J. Ding, Verification of icephobic/anti-icing properties of a superhydrophobic surface, ACS Applied Materials and Interfaces. 5 (2013) 3370–3381. doi:10.1021/am400429q.

[76] P. Tourkine, M. Le Merrer, D. Quéré, Delayed freezing on water repellent materials, Langmuir. 25 (2009) 7214–7216. doi:10.1021/la900929u.

[77] L. Cao, A.K. Jones, V.K. Sikka, J. Wu, D. Gao, Anti-Icing superhydrophobic coatings, Langmuir. 25 (2009) 12444–12448. doi:10.1021/la902882b.

[78] P. Kim, T.S. Wong, J. Alvarenga, M.J. Kreder, W.E. Adorno-Martinez, J. Aizenberg, Liquid-infused nanostructured surfaces with extreme anti-ice and anti-frost performance, ACS Nano. 6 (2012) 6569–6577. doi:10.1021/nn302310q.

[79] P.W. Wilson, W. Lu, H. Xu, P. Kim, M.J. Kreder, J. Alvarenga, J. Aizenberg, Inhibition of ice nucleation by slippery liquid-infused porous surfaces (SLIPS)., Physical Chemistry Chemical Physics : PCCP. 15 (2013) 581–5. doi:10.1039/c2cp43586a.

[80] H.A. Stone, Ice-phobic surfaces that are wet, ACS Nano. 6 (2012) 6536–6540. doi:10.1021/nn303372q.

[81] H. Dodiuk, S. Kenig, a. Dotan, Do Self-cleaning Surfaces Repel Ice?, Journal of Adhesion Science and Technology. 26 (2012) 701–714. doi:10.1163/016942411X575933.

[82] H. Wang, G. He, Q. Tian, Effects of nano-fluorocarbon coating on icing, Applied Surface Science. 258 (2012) 7219–7224. doi:10.1016/j.apsusc.2012.04.043.

[83] H. Mei, D. Luo, P. Guo, C. Song, C. Liu, Y. Zheng, L. Jiang, Multi-level micro-/nanostructures of butterfly wings adapt at low temperature to water repellency, Soft Matter. 7 (2011) 10569. doi:10.1039/c1sm06347b.

[84] K.L. Mittal, Adhesion Measurement of Thin Films, ElectroComponent Science and Technology. 3 (1976) 21–42. doi:10.1155/APEC.3.21.

[85] L. Gao, T.J. McCarthy, Wetting 101??, Langmuir. 25 (2009) 14105–14115. doi:10.1021/la902206c.

[86] A. Dotan, H. Dodiuk, C. Laforte, S. Kenig, The Relationship between Water Wetting and Ice Adhesion, Journal of Adhesion Science and Technology. 23 (2009) 1907–1915. doi:10.1163/016942409X12510925843078.

[87] A.J. Meuler, G.H. McKinley, R.E. Cohen, Exploiting topographical texture to impart icephobicity, ACS Nano. 4 (2010) 7048–7052. doi:10.1021/nn103214q.

[88] V. Bahadur, L. Mishchenko, B. Hatton, J.A. Taylor, J. Aizenberg, T. Krupenkin, Predictive model for ice formation on superhydrophobic surfaces, Langmuir. 27 (2011) 14143–14150. doi:10.1021/la200816f.

[89] P. Guo, Y. Zheng, M. Wen, C. Song, Y. Lin, L. Jiang, Icephobic/anti-icing properties of micro/nanostructured surfaces, Advanced Materials. 24 (2012) 2642–2648. doi:10.1002/adma.201104412.

[90] F. Wang, C. Li, Y. Lv, F. Lv, Y. Du, Ice accretion on superhydrophobic aluminum surfaces under low-temperature conditions, Cold Regions Science and Technology. 62 (2010) 29–33. doi:10.1016/j.coldregions.2010.02.005.

[91] C. Antonini, M. Innocenti, T. Horn, M. Marengo, A. Amirfazli, Understanding the effect of superhydrophobic coatings on energy reduction in anti-icing systems, Cold Regions Science and Technology. 67 (2011) 58–67. doi:10.1016/j.coldregions.2011.02.006.

[92] S.A. Kulinich, M. Farzaneh, Ice adhesion on super-hydrophobic surfaces, Applied Surface Science. 255 (2009) 8153–8157. doi:10.1016/j.apsusc.2009.05.033.

[93] M.A. Sarshar, C. Swarctz, S. Hunter, J. Simpson, C.H. Choi, Effects of contact angle hysteresis on ice adhesion and growth on superhydrophobic surfaces under dynamic flow conditions, Colloid and Polymer Science. 291 (2013) 427–435. doi:10.1007/s00396-012-2753-4.

[94] L. Mishchenko, B. Hatton, V. Bahadur, J.A. Taylor, T. Krupenkin, J. Aizenberg, Design of ice-free nanostructured surfaces based on repulsion of impacting water droplets, ACS Nano. 4 (2010) 7699–7707. doi:10.1021/nn102557p.

[95] D.A. Del Cerro, G.R.B.E. Römer, A.J. Huis In't Veld, Erosion resistant anti-ice surfaces generated by ultra short laser pulses, Physics Procedia. 5 (2010) 231–235. doi:10.1016/j.phpro.2010.08.141.

[96] C. Laforte, J.L. Laforte, Deicing strains and stresses of iced substrates, Journal of Adhesion Science and Technology. 26 (2012) 603–620. doi:10.1163/016942411X574790.

[97] S. Yang, Q. Xia, L. Zhu, J. Xue, Q. Wang, Q.M. Chen, Research on the icephobic properties of fluoropolymer-based materials, Applied Surface Science. 257 (2011) 4956–4962. doi:10.1016/j.apsusc.2011.01.003.

[98] H.L. West, A.R. Ogston, Compositions for the prevention of the formation or accretion of ice on exposed surfaces, 2373727, 1945.

[99] J.M. Fain, N.L. Hewitt, R. Bank, De-icing and freeze depressant composition, 2716068, 1955.

[100] C. Tendero, C. Tixier, P. Tristant, J. Desmaison, P. Leprince, Atmospheric pressure plasmas: A review, Spectrochimica Acta - Part B Atomic Spectroscopy. 61 (2006) 2–30. doi:10.1016/j.sab.2005.10.003.

[101] A. Grill, Cold plasma materials fabrication: from fundamentals to applications, IEEE Press, New York, 1993.

[102] A.M. Hirst, F.M. Frame, M. Arya, N.J. Maitland, D. O'Connell, Low temperature plasmas as emerging cancer therapeutics: the state of play and thoughts for the future,

Tumor Biology. 37 (2016) 7021–7031. doi:10.1007/s13277-016-4911-7.

[103] K.D. Weltmann, E. Kindel, R. Brandenburg, C. Meyer, R. Bussiahn, C. Wilke, T. von Woedtke, Atmospheric pressure plasma jet for medical therapy: Plasma parameters and risk estimation, Contributions to Plasma Physics. 49 (2009) 631–640. doi:10.1002/ctpp.200910067.

[104] K.D. Weltmann, E. Kindel, T. von Woedtke, M. Hähnel, M. Stieber, R. Brandenburg, Atmospheric-pressure plasma sources: Prospective tools for plasma medicine, Pure and Applied Chemistry. 82 (2010) 1223–1237. doi:10.1351/PAC-CON-09-10-35.

[105] K. Heuer, M. a Hoffmanns, E. Demir, S. Baldus, C.M. Volkmar, M. Röhle, P.C. Fuchs, P. Awakowicz, C. V Suschek, C. Opländer, The topical use of non-thermal dielectric barrier discharge (DBD): Nitric oxide related effects on human skin., Nitric Oxide : Biology and Chemistry / Official Journal of the Nitric Oxide Society. 44C (2014) 52–60. doi:10.1016/j.niox.2014.11.015.

[106] C. Hertwig, K. Reineke, J. Ehlbeck, D. Knorr, O. Schlüter, Decontamination of whole black pepper using different cold atmospheric pressure plasma applications, Food Control. 55 (2015) 221–229. doi:10.1016/j.foodcont.2015.03.003.

[107] F. Pasquali, A.C. Stratakos, A. Koidis, A. Berardinelli, C. Cevoli, L. Ragni, R. Mancusi, G. Manfreda, M. Trevisani, Atmospheric cold plasma process for vegetable leaf decontamination: A feasibility study on radicchio (red chicory, Cichorium intybus L.), Food Control. 60 (2016) 552–559. doi:10.1016/j.foodcont.2015.08.043.

[108] D. Butscher, D. Zimmermann, M. Schuppler, P. Rudolf von Rohr, Plasma inactivation of bacterial endospores on wheat grains and polymeric model substrates in a dielectric barrier discharge, Food Control. 60 (2016) 636–645. doi:10.1016/j.foodcont.2015.09.003.

[109] E. Amanatides, D. Mataras, Modeling and Diagnostics of He Discharges for Treatment of Polymers, in: R. D'Agostino, P. Favia, Y. Kawai, H. Ikegami, N. Sato, F. Arefi-khonsari (Eds.), Advanced Plasma Technology, WILEY-VCH Verlag GmbH & Co. KGaA, Weinheim, 2008: pp. 55–74. doi:10.1002/9783527622184.ch4.

[110] P.K. Chu, S. Qin, C. Chan, N.W. Cheung, L.A. Larson, Plasma immersion ion implantation - A fledgling technique for semiconductor processing, Materials Science and Engineering R: Reports. 17 (1996) 207–280. doi:10.1016/S0927-796X(96)00194-5.

[111] P.N. Dave, A.K. Joshi, Plasma Pyrolysis and Gasification of plastic waste - a review, Journal of Scientific & Industrial Research. 69 (2010) 177–179.

[112] R. Chattopadhyay, Advanced Thermally Assisted Surface Engineering Processes, Kluwer Academic Publishers, 2004. doi:10.1017/CBO9781107415324.004.

[113] H. Chang, Y.J. Yang, H.C. Li, C.C. Hsu, I.C. Cheng, J.Z. Chen, Preparation of nanoporous TiO2 films for DSSC application by a rapid atmospheric pressure plasma jet sintering process, Journal of Power Sources. 234 (2013) 16–22. doi:10.1016/j.jpowsour.2013.01.113.

[114] H. Chien, K. Ma, Y. Yeh, C. Chao, Preparation of Superhydrophobic Surface for PTFE / ePTFE Materials by Oxygen Plasma Treatment, in: Ieee, 2011: pp. 1215–1218.

[115] W. Tong, P.A. Tran, A.M. Turnley, M. Aramesh, S. Prawer, M. Brandt, K. Fox, The influence of sterilization on nitrogen-included ultrananocrystalline diamond for biomedical applications, Materials Science and Engineering C. 61 (2016) 324–332.

doi:10.1016/j.msec.2015.12.041.

[116] A. Vesel, I. Junkar, U. Cvelbar, J. Kovac, M. Mozetic, Surface modification of polyester by oxygen- And nitrogen-plasma treatment, Surface and Interface Analysis. 40 (2008) 1444–1453. doi:10.1002/sia.2923.

[117] M.R. Wertheimer, B. Saoudi, M. Ahlawat, R. Kashyap, In situ thermometry in noble gas dielectric barrier discharges at atmospheric pressure, Plasma Processes and Polymers. 9 (2012) 955–967. doi:10.1002/ppap.201200028.

[118] J. Prégent, L. Vandsburger, V. Blanchard, P. Blanchet, B. Riedl, A. Sarkissian, L. Stafford, Modification of hardwood samples in the flowing afterglow of N2/O2 dielectric barrier discharges open to ambient air, Cellulose. 22 (2015) 3397–3408. doi:10.1007/s10570-015-0736-6.

[119] O. Levasseur, a Bouarouri, N. Naudé, R. Clergereaux, N. Gherardi, L. Stafford, Organization of dielectric barrier discharges in the presence of structurally-inhomogeneous wood substrates, Escampig 2012. 1 (2012) 14–15. doi:10.1109/TPS.2014.2321518.

[120] K. Fricke, I. Koban, H. Tresp, L. Jablonowski, K. Schröder, A. Kramer, K.D. Weltmann, T. von Woedtke, T. Kocher, Atmospheric pressure plasma: A high-performance tool for the efficient removal of biofilms, PLoS ONE. 7 (2012) 1–8. doi:10.1371/journal.pone.0042539.

[121] A. El-Shafei, H. Helmy, A. Ramamoorthy, P. Hauser, Nanolayer atmospheric pressure plasma graft polymerization of durable repellent finishes on cotton, Journal of Coatings Technology Research. 12 (2015) 681–691. doi:10.1007/s11998-015-9665-4.

[122] B. Cortese, H. Morgan, Controlling the wettability of hierarchically structured thermoplastics, Langmuir. 28 (2012) 896–904. doi:10.1021/la203741b.

[123] J. Vetter, G. Barbezat, J. Crummenauer, J. Avissar, Surface treatment selections for automotive applications, Surface and Coatings Technology. 200 (2005) 1962–1968. doi:10.1016/j.surfcoat.2005.08.011.

[124] M.Y. Alkawareek, S.P. Gorman, W.G. Graham, B.F. Gilmore, Eradication of marine biofilms by atmospheric pressure non-thermal plasma: A potential approach to control biofouling?, International Biodeterioration and Biodegradation. 86 (2014) 14–18. doi:10.1016/j.ibiod.2013.05.030.

[125] F. Massines, J. Silva, J.F. Leli??vre, R. Bazinette, J. Vallade, P. Lecouvreur, S. Pouliquen, Hydrogenated Silicon Nitride SiNx:H Deposited by Dielectric Barrier Discharge for Photovoltaics, Plasma Processes and Polymers. 13 (2016) 170–183. doi:10.1002/ppap.201500182.

[126] B. Chapman, Glow Discharge Processes, New York, 1980. doi:QC702.7.P6C48.

[127] K. Ellinas, A. Tserepi, E. Gogolides, From superamphiphobic to amphiphilic polymeric surfaces with ordered hierarchical roughness fabricated with colloidal lithography and plasma nanotexturing, Langmuir. 27 (2011) 3960–3969. doi:10.1021/la104481p.

[128] J. Park, H. Lim, W. Kim, J.S. Ko, Design and fabrication of a superhydrophobic glass surface with micro-network of nanopillars, Journal of Colloid and Interface Science. 360 (2011) 272–279. doi:10.1016/j.jcis.2011.04.047.

[129] F. Palumbo, R. Di Mundo, D. Cappelluti, R. Dagostino, SuperHydrophobic and SuperHydrophilic polycarbonate by tailoring chemistry and nano-texture with

plasma processing, Plasma Processes and Polymers. 8 (2011) 118–126. doi:10.1002/ppap.201000098.

[130] L.M. Lacroix, M. Lejeune, L. Ceriotti, M. Kormunda, T. Meziani, P. Colpo, F. Rossi, Tuneable rough surfaces: A new approach for elaboration of superhydrophobic films, Surface Science. 592 (2005) 182–188. doi:10.1016/j.susc.2005.07.006.

[131] E. Wohlfart, J.P. Fernández-Blázquez, E. Arzt, A. Del Campo, Nanofibrillar patterns on PET: The influence of plasma parameters in surface morphology, Plasma Processes and Polymers. 8 (2011) 876–884. doi:10.1002/ppap.201000164.

[132] J.P. Fernández-Blázquez, D. Fell, E. Bonaccurso, A. del Campo, Superhydrophilic and superhydrophobic nanostructured surfaces via plasma treatment, Journal of Colloid and Interface Science. 357 (2011) 234–238. doi:10.1016/j.jcis.2011.01.082.

[133] T. Takahashi, Y. Hirano, Y. Takasawa, T. Gowa, N. Fukutake, A. Oshima, S. Tagawa, M. Washio, Change in surface morphology of polytetrafluoroethylene by reactive ion etching, Radiation Physics and Chemistry. 80 (2011) 253–256. doi:10.1016/j.radphyschem.2010.07.042.

[134] Y. Han, S.O. Manolach, F. Denes, R.M. Rowell, Cold plasma treatment on starch foam reinforced with wood fiber for its surface hydrophobicity, Carbohydrate Polymers. 86 (2011) 1031–1037. doi:10.1016/j.carbpol.2011.05.056.

[135] N. Vandencasteele, H. Fairbrother, F. Reniers, Selected effect of the ions and the neutrals in the plasma treatment of PTFE surfaces: An OES-AFM-contact angle and XPS study, Plasma Processes and Polymers. 2 (2005) 493–500. doi:10.1002/ppap.200500010.

[136] N. Vandencasteele, B. Nisol, P. Viville, R. Lazzaroni, D.G. Castner, F. Reniers, Plasma-modified PTFE for biological applications: Correlation between protein-resistant properties and surface characteristics, Plasma Processes and Polymers. 5 (2008) 661–671. doi:10.1002/ppap.200700143.

[137] E.A.D. Carbone, N. Boucher, M. Sferrazza, F. Reniers, How to increase the hydrophobicity of PTFE surfaces using an r.f. atmospheric-pressure plasma torch, Surface and Interface Analysis. 42 (2010) 1014–1018. doi:10.1002/sia.3384.

[138] R. Morent, N. De Geyter, T. Desmet, P. Dubruel, C. Leys, Plasma surface modification of biodegradable polymers: A review, Plasma Processes and Polymers. 8 (2011) 171–190. doi:10.1002/ppap.201000153.

[139] J. Fresnais, J.P. Chapel, F. Poncin-Epaillard, Synthesis of transparent superhydrophobic polyethylene surfaces, Surface and Coatings Technology. 200 (2006) 5296–5305. doi:10.1016/j.surfcoat.2005.06.022.

[140] I. Woodward, W.C.E. Schofield, V. Roucoules, J.P.S. Badyal, Super-hydrophobic surfaces produced by plasma fluorination of polybutadiene films, Langmuir. 19 (2003) 3432–3438. doi:10.1021/la020427e.

[141] R.W. Jaszewski, H. Schift, B. Schnyder, A. Schneuwly, P. Gröning, Deposition of anti-adhesive ultra-thin teflon-like films and their interaction with polymers during hot embossing, Applied Surface Science. 143 (1999) 301–308. doi:10.1016/S0169-4332(99)00014-8.

[142] M.A. Golub, T. Wydeven, A.L. Johnson, Similarity of plasma-polymerized tetrafluoroethylene and fluoropolymer films deposited by rf sputtering of poly(tetrafluoroethylene), Langmuir. 14 (1998) 2217–2220. doi:10.1021/la971102e.

[143] H. Biederman, M. Zeuner, J. Zalman, P. Bílková, D. Slavínská, V. Stelmasuk, A. Boldyreva, Rf magnetron sputtering of polytetrafluoroethylene under various conditions, Thin Solid Films. 392 (2001) 208–213. doi:10.1016/S0040-6090(01)01029-X.

[144] M.E. Ryan, L.C. Fonseca, S. Tasker, J.P.S. Badyal, Plasma Polymerization of Sputtered Poly(tetrafluoroethylene), Journal of Physical Chemistry. 99 (1995) 7060–7064.

[145] M. Drábik, O. Polonskyi, O. Kylián, J. Čechvala, A. Artemenko, I. Gordeev, A. Choukourov, D. Slavínská, I. Matolínová, H. Biederman, Super-hydrophobic coatings prepared by RF magnetron sputtering of PTFE, Plasma Processes and Polymers. 7 (2010) 544–551. doi:10.1002/ppap.200900164.

[146] O. Kylián, M. Drábik, O. Polonskyi, J. Čechvala, A. Artemenko, I. Gordeev, A. Choukourov, I. Matolínová, D. Slavínská, H. Biederman, Deposition of nanostructured fluorocarbon plasma polymer films by RF magnetron sputtering of polytetrafluoroethylene, Thin Solid Films. 519 (2011) 6426–6431. doi:10.1016/j.tsf.2011.04.213.

[147] V. Stelmashuk, H. Biederman, D. Slavínská, J. Zemek, M. Trchová, Plasma polymer films rf sputtered from PTFE under various argon pressures, Vacuum. 77 (2005) 131–137. doi:10.1016/j.vacuum.2004.08.011.

[148] H.K. Yasuda, Plasma Polymerization, Academic Press, London, 2012. https://books.google.com/books?id=5Fi1lIMCdtsC&pgis=1 (accessed October 31, 2011).

[149] M.T. Van Os, Surface modification by plasma polymerization: film deposition, tailoring of surface properties and biocompatibility, Print Partners Ipskamp, Enschede, 2000. doi:90 36515130.

[150] S. Gaur, G. Vergason, V. Technology, V. Etten, Plasma Polymerization: Theory and Practice, in: Society of Vacuum Coaters: 43rd Annual Technical Conference Proceedings, Society of Vacuum Coaters, Denver, 2000: pp. 267–271.

[151] D. Hegemann, M.M. Hossain, E. Körner, D.J. Balazs, Macroscopic description of plasma polymerization, Plasma Processes and Polymers. 4 (2007) 229–238. doi:10.1002/ppap.200600169.

[152] H. Yasuda, Y. Matsuzawa, Economical advantages of low-pressure plasma polymerization coating, Plasma Processes and Polymers. 2 (2005) 507–512. doi:10.1002/ppap.200500002.

[153] J. Pulpytel, V. Kumar, P. Peng, V. Micheli, N. Laidani, F. Arefi-Khonsari, Deposition of organosilicon coatings by a non-equilibrium atmospheric pressure plasma jet: Design, analysis and macroscopic scaling law of the process, Plasma Processes and Polymers. 8 (2011) 664–675. doi:10.1002/ppap.201000121.

[154] U. Lommatzsch, J. Ihde, Plasma polymerization of HMDSO with an atmospheric pressure plasma jet for corrosion protection of aluminum and low-adhesion surfaces, Plasma Processes and Polymers. 6 (2009) 642–648. doi:10.1002/ppap.200900032.

[155] L.J. Ward, W.C.E. Schofield, J.P.S. Badyal, A.J. Goodwin, P.J. Merlin, Atmospheric Pressure Glow Discharge Deposition of Polysiloxane and SiO x Films, Langmuir. 19 (2003) 2110–2114. doi:10.1021/la0204287.

[156] E. Hare, E. Shafrin, W. Zisman, Properties of films of adsorbed fluorinated acids, The

Journal of Physical .... 513 (1954) 236–239. doi:10.1021/j150513a011.

[157] N. Vandencasteele, F. Reniers, Plasma-modified polymer surfaces: Characterization using XPS, Journal of Electron Spectroscopy and Related Phenomena. 178–179 (2010) 394–408. doi:10.1016/j.elspec.2009.12.003.

[158] F.J. du Toit, R.D. Sanderson, W.J. Engelbrecht, J.B. Wagener, The effect of surface fluorination on the wettability of high density polyethylene, Journal of Fluorine Chemistry. 74 (1995) 43–48. doi:10.1016/0022-1139(94)03218-O.

[159] P.P. Bera, J.S. Francisco, T.J. Lee, Design strategies to minimize the radiative efficiency of global warming molecules., Proceedings of the National Academy of Sciences of the United States of America. 107 (2010) 9049–9054. doi:10.1073/pnas.0913590107.

[160] K. Steenland, T. Fletcher, D.A. Savitz, Epidemiologic evidence on the health effects of perfluorooctanoic acid (PFOA), Environmental Health Perspectives. 118 (2010) 1100–1108. doi:10.1289/ehp.0901827.

[161] A. Satyaprasad, V. Jain, S.K. Nema, Deposition of superhydrophobic nanostructured Teflon-like coating using expanding plasma arc, Applied Surface Science. 253 (2007) 5462–5466. doi:10.1016/j.apsusc.2006.12.085.

[162] G.H. Yang, Y. Zhang, E.T. Kang, K.G. Neoh, A.C.H. Huan, D.M.Y. Lai, Plasma polymerization of allylpentafluorobenzene on copper surfaces, Journal of Materials Chemistry. 12 (2002) 426–431. doi:10.1039/b108895p.

[163] Y. Zhang, E.T. Kang, K.G. Neoh, W. Huang, A.C.H. Huan, H. Zhang, R.N. Lamb, Surface modification of polyimide films via plasma polymerization and deposition of allylpentafluorobenzene, Polymer. 43 (2002) 7279–7288. doi:10.1016/S0032-3861(02)00711-5.

[164] R. Menini, M. Farzaneh, Elaboration of Al2O3/PTFE icephobic coatings for protecting aluminum surfaces, Surface and Coatings Technology. 203 (2009) 1941–1946. doi:10.1016/j.surfcoat.2009.01.030.

[165] Y.Y. Ji, Y.C. Hong, S.H. Lee, S.D. Kim, S.S. Kim, Formation of super-hydrophobic and water-repellency surface with hexamethyldisiloxane (HMDSO) coating on polyethyleneteraphtalate fiber by atmosperic pressure plasma polymerization, Surface and Coatings Technology. 202 (2008) 5663–5667. doi:10.1016/j.surfcoat.2008.06.151.

[166] P. Favia, R. Agostino, F. Fracassi, D. Chimica, Plasma and surface diagnostics in PECVD from silicon containing organic monomers, Pure and Applied Chemistry. 66 (2009) 1373–1380. doi:10.1351/pac199466061373.

[167] S. Nogueira, I.H. Tan, R. Furlan, S.P. Brazil, P. Rico, Production of Highly Hydrophobic Films Using Low Frequency and High Density Plasma, Revista Brasileira de Aplicações de Vácuo. 25 (2006) 45–53.

[168] R.A. Siliprandi, S. Zanini, E. Grimoldi, F.S. Fumagalli, R. Barni, C. Riccardi, Atmospheric pressure plasma discharge for polysiloxane thin films deposition and comparison with low pressure process, Plasma Chemistry and Plasma Processing. 31 (2011) 353–372. doi:10.1007/s11090-011-9286-3.

[169] V. Rouessac, A. Ungureanu, S. Bangarda, A. Deratani, C.H. Lo, T.C. Wei, K.R. Lee, J.Y. Lai, Fluorine-free superhydrophobic microstructured films grown by PECVD, Chemical Vapor Deposition. 17 (2011) 198–203. doi:10.1002/cvde.201106903.

[170] Y.Y. Ji, S.S. Kim, O.P. Kwon, S.H. Lee, Easy fabrication of large-size superhydrophobic surfaces by atmospheric pressure plasma polymerization with non-polar aromatic hydrocarbon in an in-line process, Applied Surface Science. 255 (2009) 4575–4578. doi:10.1016/j.apsusc.2008.12.002.

[171] S.C. Cho, Y.C. Hong, S.G. Cho, Y.Y. Ji, C.S. Han, H.S. Uhm, Surface modification of polyimide films, filter papers, and cotton clothes by HMDSO/toluene plasma at low pressure and its wettability, Current Applied Physics. 9 (2009) 1223–1226. doi:10.1016/j.cap.2009.01.020.

[172] D.K. Sarkar, M. Farzaneh, R.W. Paynter, Wetting and superhydrophobic properties of PECVD grown hydrocarbon and fluorinated-hydrocarbon coatings, Applied Surface Science. 256 (2010) 3698–3701. doi:10.1016/j.apsusc.2009.12.049.

[173] a. D. Aliev, L.B. Boinovich, V.L. Bukhovets, a. M. Emelyanenko, a. M. Gorbunov, a. E. Gorodetskii, a. S. Pashinin, Superhydrophobic coatings based on boron nitride nanotubes: The mechanism of superhydrophobicity and self-regeneration of highly hydrophobic properties, Nanotechnologies in Russia. 6 (2011) 723–732. doi:10.1134/S1995078011060024.

[174] J.-H. Kim, G. Liu, S.H. Kim, Deposition of stable hydrophobic coatings with in-line CH4 atmospheric rf plasma, Journal of Materials Chemistry. 16 (2006) 977. doi:10.1039/b516329c.

[175] M. Nisoa, P. Wanichapichart, Surface hydrophobic modification of cellulose membranes by plasma-assisted deposition of hydrocarbon films, Songklanakarin Journal of Science and Technology. 32 (2010) 97–101.

[176] H. Ji, A. Côté, D. Koshel, B. Terreault, G. Abel, P. Ducharme, G. Ross, S. Savoie, M. Gagné, Hydrophobic fluorinated carbon coatings on silicate glaze and aluminum, Thin Solid Films. 405 (2002) 104–108. doi:10.1016/S0040-6090(01)01707-2.

[177] A.S.C.M. D'Oliveira, R. Vilar, C.G. Feder, High temperature behaviour of plasma transferred arc and laser Co-based alloy coatings, Applied Surface Science. 201 (2002) 154–160. doi:10.1016/S0169-4332(02)00621-9.

[178] A. Gatto, E. Bassoli, M. Fornari, Plasma Transferred Arc deposition of powdered high performances alloys: Process parameters optimisation as a function of alloy and geometrical configuration, Surface and Coatings Technology. 187 (2004) 265–271. doi:10.1016/j.surfcoat.2004.02.013.

[179] H.J. Kim, B.H. Yoon, C.H. Lee, Wear performance of the Fe-based alloy coatings produced by plasma transferred arc weld-surfacing process, Wear. 249 (2001) 846–852. doi:10.1016/S0043-1648(01)00683-4.

[180] M. Yan, W.Z. Zhu, Surface treatment of 45 steel by plasma-arc melting, Surface and Coatings Technology. 91 (1997) 183–191. http://www.sciencedirect.com/science/article/pii/S0257897296031817.

[181] L. Bourithis, S. Papaefthymiou, G.D. Papadimitriou, Plasma transferred arc boriding of a low carbon steel: Microstructure and wear properties, Applied Surface Science. 200 (2002) 203–218. doi:10.1016/S0169-4332(02)00901-7.

[182] R.L. Deuis, J.M. Yellup, C. Subramanian, Metal-matrix composite coatings by PTA surfacing, Composites Science and Technology. 58 (1998) 299–309. doi:10.1016/S0266-3538(97)00131-0.

[183] F. Matsuda, K. Nakata, S. Shimizu, K. Nagai, Carbide Addition on Aluminum Alloy

Surface by Plasma Transferred Arc Welding Process, Transactions of JWIR. 19 (1990) 81–87.

[184] A. Moshkovith, V. Perfiliev, D. Gindin, N. Parkansky, R. Boxman, L. Rapoport, Surface texturing using pulsed air arc treatment, Wear. 263 (2007) 1467–1469. doi:10.1016/j.wear.2006.11.043.

[185] D. Bouilly, D. Perez, L.J. Lewis, Damage in materials following ablation by ultrashort laser pulses: A molecular-dynamics study, Physical Review B - Condensed Matter and Materials Physics. 76 (2007) 1–9. doi:10.1103/PhysRevB.76.184119.

[186] B.N. Chichkov, C. Momma, S. Nolte, F. von Alvensleben, A. Tünnermann, Femtosecond, picosecond and nanosecond laser ablation of solids, Applied Physics A: Materials Science & Processing. 63 (1996) 109–115. doi:10.1007/s003390050359.

[187] S. Nolte, C. Momma, H. Jacobs, A. Tu, B.N. Chichkov, B. Wellegehausen, H. Welling, Ablation of metals by ultrashort laser pulses, Journal of the Optical Society of America B. 14 (1997) 2716–2722. doi:10.1364/JOSAB.14.002716.

[188] R. Le Harzic, N. Huot, E. Audouard, C. Jonin, P. Laporte, S. Valette, A. Fraczkiewicz, R. Fortunier, Comparison of heat-affected zones due to nanosecond and femtosecond laser pulses using transmission electronic microscopy, Applied Physics Letters. 80 (2002) 3886–3888. doi:10.1063/1.1481195.

[189] A. Gragossian, S.H. Tavassoli, B. Shokri, Laser ablation of aluminum from normal evaporation to phase explosion, Journal of Applied Physics. 105 (2009) 1–8. doi:10.1063/1.3131689.

[190] C. Porneala, D.A. Willis, Time-resolved dynamics of nanosecond laser-induced explosion, Applied Physics Letters. 42 (2009). doi:10.1088/0022-3727/42/15/155503.

[191] A. Miotello, R. Kelly, Laser-induced phase explosion: New physical problems when a condensed phase approaches the thermodynamic critical temperature, Applied Physics A: Materials Science and Processing. 69 (1999) 67–73. doi:10.1007/s003399900296.

[192] L. V. Zhigilei, B.J. Garrison, Microscopic mechanisms of laser ablation of organic solids in the thermal and stress confinement irradiation regimes, Journal of Applied Physics. 88 (2000) 1281–1298. doi:10.1063/1.373816.

[193] N.M. Bulgakova, A. V. Bulgakov, Pulsed laser ablation of solids: transition from normal vaporization to phase explosion, Applied Physics A Materials Science & Processing. 73 (2001) 199–208. doi:10.1007/s003390000686.

[194] C. Porneala, D.A. Willis, Observation of nanosecond laser-induced phase explosion in aluminum, Applied Physics Letters. 89 (2006) 1–4. doi:10.1063/1.2393158.

[195] H. Kakiuchi, K. Higashida, T. Shibata, H. Ohmi, T. Yamada, K. Yasutake, High-rate HMDSO-based coatings in open air using atmospheric-pressure plasma jet, Journal of Non-Crystalline Solids. 358 (2012) 2462–2465. doi:10.1016/j.jnoncrysol.2011.12.081.

[196] J. Park, H.-S. Han, Y.-C. Kim, J.-P. Ahn, M.-R. Ok, K.E. Lee, J.-W. Lee, P.-R. Cha, H.-K. Seok, H. Jeon, Direct and accurate measurement of size dependent wetting behaviors for sessile water droplets, Scientific Reports. 5 (2015) 18150. doi:10.1038/srep18150.

[197] L.A. O'Hare, B. Parbhoo, S.R. Leadley, Development of a methodology for XPS curve-

fitting of the Si 2p core level of siloxane materials, Surface and Interface Analysis. 36 (2004) 1427–1434. doi:10.1002/sia.1917.

[198] L.A. O'Hare, A. Hynes, M.R. Alexander, A methodology for curve-fitting of the XPS Si 2p core level from thin siloxane coatings, Surface and Interface Analysis. 39 (2007) 926–936. doi:10.1002/sia.2634 A.

[199] N.D. Boscher, D. Duday, S. Verdier, P. Choquet, Single-step process for the deposition of high water contact angle and high water sliding angle surfaces by atmospheric pressure dielectric barrier discharge, ACS Applied Materials and Interfaces. 5 (2013) 1053–1060. doi:10.1021/am302795v.

[200] PV Maps, Natural Resources Canada. (2016).

[201] Fridman, Kinetic modelling for an atmospheric pressure argon plasma jet in humid air, Journal of Physics D: Applied Physics. 46 (2013) 275201. doi:10.1088/0022-3727/46/27/275201.

[202] V.A. Bityurin, A. V. Grigorenko, A. V. Efimov, A.I. Klimov, O. V. Korshunov, D.S. Kutuzov, V.F. Chinnov, Spectral and kinetic analysis of heterogeneous gas discharge plasma in the flow of an Al, H2O, and Ar mixture, High Temperature. 52 (2014) 1–11. doi:10.1134/S0018151X14010052.

[203] M. Castro, R. Cuerno, M. Nicoli, L. V??zquez, J.G. Buijnsters, Universality of cauliflower-like fronts: From nanoscale thin films to macroscopic plants, New Journal of Physics. 14 (2012). doi:10.1088/1367-2630/14/10/103039.

[204] R. Messier, J.E. Yehoda, Geometry of thin-film morphology, Journal of Applied Physics. 58 (1985).

[205] M. Ricci, J.L. Dorier, C. Hollenstein, P. Fayet, Influence of argon and nitrogen admixture in HMDSO/O2 plasmas onto powder formation, Plasma Processes and Polymers. 8 (2011) 108–117. doi:10.1002/ppap.201000052.

[206] O. Levasseur, L. Stafford, N. Gherardi, N. Naudé, E. Beche, J. Esvan, P. Blanchet, B. Riedl, A. Sarkissian, Role of substrate outgassing on the formation dynamics of either hydrophilic or hydrophobic wood surfaces in atmospheric-pressure, organosilicon plasmas, Surface and Coatings Technology. 234 (2013) 42–47. doi:10.1016/j.surfcoat.2013.05.045.

[207] A. Kilicaslan, O. Levasseur, V. Roy-Garofano, J. Profili, M. Moisan, C. C??t??, A. Sarkissian, L. Stafford, Optical emission spectroscopy of microwave-plasmas at atmospheric pressure applied to the growth of organosilicon and organotitanium nanopowders, Journal of Applied Physics. 115 (2014). doi:10.1063/1.4868899.

[208] M.K. Gunde, Vibrational modes in amorphous silicon dioxide, Physica B: Condensed Matter. 292 (2000) 286–295. doi:10.1016/S0921-4526(00)00475-0.

[209] J. Petersen, J. Bardon, A. Dinia, D. Ruch, N. Gherardi, Organosilicon Coatings Deposited in Atmospheric Pressure Townsend Discharge for Gas Barrier Purpose: Effect of Substrate Temperature on Structure and Properties, ACS Applied Materials & Interfaces. 4 (2012) 5872–5882. doi:10.1021/am3015229.

[210] A. Granier, M. Vervloet, K. Aumaille, C. Vall e, Optical emission spectra of TEOS and HMDSO derived plasmas used for thin film deposition, Plasma Sources Science and Technology. 12 (2003) 89–96. doi:10.1088/0963-0252/12/1/312.

[211] P.J. Launer, Infrared Analysis of organosilicon compounds: spectra-structure correlations, 1987.

[212] L.G. Britcher, D.C. Kehoe, J.G. Matisons, A.G. Swincer, Siloxane Coupling Agents, Macromolecules. 28 (1995) 3110–3118. doi:10.1021/ma00113a013.

[213] R. Dorai, M.J. Kushner, A model for plasma modification of polypropylene using atmospheric pressure discharges, Journal of Physics D: Applied Physics. 36 (2003) 666–685. doi:10.1088/0022-3727/36/6/309.

[214] L. Zhu, G. Gamez, T.A. Schmitz, F. Krumeich, R. Zenobi, Material ejection and redeposition following atmospheric pressure near-field laser ablation on molecular solids, Analytical and Bioanalytical Chemistry. 396 (2010) 163–172. doi:10.1007/s00216-009-2919-1.

[215] S.H. Tan, N.T. Nguyen, Y.C. Chua, T.G. Kang, Oxygen plasma treatment for reducing hydrophobicity of a sealed polydimethylsiloxane microchannel, Biomicrofluidics. 4 (2010) 1–8. doi:10.1063/1.3466882.

[216] D.T. Eddington, J.P. Puccinelli, D.J. Beebe, Thermal aging and reduced hydrophobic recovery of polydimethylsiloxane, Sensors and Actuators, B: Chemical. 114 (2006) 170–172. doi:10.1016/j.snb.2005.04.037.

[217] P. Koulik, S. Begounov, S. Goloviatinskii, Atmospheric Plasma Sterilization and Deodorization of Dielectric Surfaces, Plasma Chemistry and Plasma Processing. 19 (1999) 311–326. doi:10.1023/A:1021604027855.

[218] S. Moradi, P. Englezos, S.G. Hatzikiriakos, Contact angle hysteresis: Surface morphology effects, Colloid and Polymer Science. 291 (2013) 317–328. doi:10.1007/s00396-012-2746-3.

[219] A.L. Andrady, S.H. Hamid, X. Hu, A. Torikai, Effects of increased solar ultraviolet radiation on materials, Journal of Photochemistry and Photobiology B: Biology. 46 (1998) 96–103. doi:10.1016/S1011-1344(98)00188-2.

[220] A. Fozza, J. Roch, J.E. Klemberg-Sapieha, A. Kruse, A. Holländer, M.R. Wertheimer, Oxidation and ablation of polymers by vacuum-UV radiation from low pressure plasmas, American Chemical Society, Polymer Preprints, Division of Polymer Chemistry. 38 (1997) 1097–1098. doi:10.1016/S0168-583X(97)00154-7.